

**Microstructure, mechanical properties, corrosion, and wear behavior of high-entropy alloy AlCoCrFeNi<sub>x</sub> ( $x > 0$ ) and medium-entropy alloy ( $x = 0$ )**

by

Rui Ken Sim

A thesis submitted in partial fulfilment of the requirement for the degree of

Master of Science

in

Chemical Engineering

Department of Chemical and Materials Engineering

University of Alberta

© Rui Ken Sim, 2022

# Abstract

As one of the early studied high-entropy alloys, AlCoCrFeNi drew considerable attention due to its attractive mechanical properties. Efforts were made to improve this material by alloying with additional elements or modifying the ratio of its elements for improved properties. On the other hand, medium-entropy alloys with fewer elements can also have superior performance with less complication. In this study, we investigated the microstructures and properties of as-cast AlCoCrFeNi<sub>x</sub> alloys ( $x = 0-2$ ), focusing on the microstructural evolution and the corresponding mechanical properties and resistance to wear, corrosion, and corrosive wear. In particular, the Ni-free four-element medium-entropy alloy, AlCoCrFe, was examined and compared with its five-element high-entropy companion, AlCoCrFeNi. It was observed that the medium-entropy alloy was harder and had a higher resistance to wear and corrosion than the five-element alloy. Detailed microstructural analyses demonstrated that the medium-entropy alloy AlCoCrFe had a spinodal-decomposed nanostructure, which grew into a two-phase microstructure with phase transformation in the five-element high-entropy alloy. With increasing Ni content, one of the phases changed from a disordered BCC structure to a softer and more ductile FCC structure, further lowering the strength of the high-entropy alloy and its resistance to wear. The medium-entropy alloy showed certain advantages with superior properties while having less complicated microstructure features.

# Preface

This thesis is an original work by Rui Ken Sim supervised by Dr. Dongyang Li. The structural analysis in Chapter 3.2.1 is made with help from Dr. Anqiang Department of Chemical and Materials Engineering, University of Alberta, who provides the TEM images. Result of nanoindentation with images and compression test were obtained with the help from Mr. Zhen Xu, Department of Chemical and Materials Engineering, University of Alberta. The electrochemical tests and analysis were assisted by Dr. Mingyu Wu, Department of Chemical and Materials Engineering, University of Alberta.

# Acknowledgment

Here I wanted to acknowledge that Dr. Dongyang Li as my supervisor, gave me a lot of help in my graduate study life and I am forever grateful for it. His patience and attitudes to the research, his precise suggestions, and control of all kinds of situations are the role model for not only me and to the worldwide researchers as well.

I am thankful for Dr. Dongyang Li's group members, especially Dr. Mingyu Wu who not only taught me of the lab's apparatus, and guidance of my research which point out the right direction of my research as I am her little brother, Dr. Anqiang He for the assistance of TEM images and analysis, Mr. Zhen Xu for helping me in mechanical test and suggestions of materials.

I am also appreciating the faculty staff of Chemical and Materials Engineering at the University of Alberta, who provided myriad of help from my daily basis to the research. I also wanted to thank the committee members who gave suggestions that making process of my research.

Last but not least, I wanted to thank my parents for the support of my study in Canada, not only in elements but also emotionally. Thanks to all the friends I met at the University of Alberta through badminton. The happiness we shared, and I will not forget about it. Wish everyone have a bright and glorious future.

# Table of Contents

Chapter 1 Introduction .....	1
Chapter 2 Literature review .....	5
2.1 The correlation of the change of microstructure with the content of elements of the alloys .....	5
2.1.1 The relationship between the change of microstructure with the alteration of elements and the mechanical properties of HEAs .....	5
2.1.2 The wear behavior of the alloys with the alteration of elements .....	10
2.1.3 The mechanical properties of medium-entropy alloys .....	15
2.2 The ability of anti-corrosion of high-entropy alloys in a chemical and mechanical way .....	19
2.2.1 Electrochemical response with the change of elements of high-entropy alloys .....	19
2.2.2 The anti-corrosion ability resulted in the corrosive wear of high-entropy alloys .....	24
2.2.3 Electrochemical response and tribo-corrosion of medium-entropy alloys .....	28
Chapter 3 Effect of Ni in Mechanical Properties and Microstructure of medium-entropy alloys AlCoCrFe and high-entropy alloys AlCoCrFeNi <sub>x</sub> (x > 0) .....	32
3.1 Experiment Procedure .....	34
3.1.1 Samples preparation .....	34
3.1.2 Microstructure characterization .....	34
3.1.3 Evaluation of physical properties .....	35
3.2 Result and discussion .....	36
3.2.1 Microstructure of AlCoCrFeNi <sub>x</sub> (x = 0 and x > 0) by SEM and TEM .....	36
3.2.2 Mechanical properties of AlCoCrFeNi <sub>x</sub> (x = 0 and x > 0) .....	47
3.2.3 The relationship between the result of wear and the physical properties of AlCoCrFeNi <sub>x</sub> (x = 0 and x > 0) .....	52

3.3 Conclusions	55
Chapter 4 Corrosion behavior of AlCoCrFeNi <sub>x</sub> (x = 0 and x > 0) by altering Ni content	57
4.1 Experiment Procedure	58
4.1.1 Sample preparation	58
4.1.2 Experimental details	59
4.2 Result and Discussion	60
4.2.1 The relation of electrical resistance of alloys to corrosion with the change of Ni content	60
4.2.2 Relationship between the change of Ni content of AlCoCrFeNi <sub>x</sub> and corrosive wear result	67
4.3 Conclusions	71
Chapter 5 General conclusions and future studies	72
5.1 Conclusions	72
5.2 Future Studies	73
References	75

# List of Tables

**Table 2.1.** Corrosion dynamics parameters of high-entropy alloys, 304 SS and Q235 steel in HCl solutions. [37]

**Table 2.2.** Mechanical properties of the materials measured with nano-indentation under the maximum load of 100 mN. [69]

**Table 2.3.** Specific wear rates of AlCoCrFeNi, AlCrFeCoNiTi0.5 and 316SS alloys in 3.5 wt. % NaCl and HCl (pH = 3) solutions. Counterpart: 6 mm diameter Si<sub>3</sub>N<sub>4</sub> ball. [69]

**Table 3.1.** – Overall and local chemical compositions (at%) of AlCoCrFeNi<sub>1.5</sub> and AlCoCrFeNi<sub>2.0</sub> determined by EDX.

**Table 3.2.** Local EDX analysis (with TEM) for different phases in AlCoCrFe, AlCoCrFeNi<sub>1.0</sub>, and AlCoCrFeNi<sub>2.0</sub>.

**Table 3.3.** Micro-hardness values of AlCoCrFe, AlCoCrFeNi<sub>1.0</sub>, AlCoCrFeNi<sub>1.5</sub>, and AlCoCrFeNi<sub>2.0</sub>; indentation loads: 80 mN and 300 mN.

**Table 3.4.** – EDX analysis of the local composition of wear tracks on the samples shown in Fig. 3.11.

**Table 4.1.** The fitting results of the impedance measurements.

**Table 4.2.** EDX compositional analysis for selected spots.

# List of Figures

**Figure 1.** Alloys between the spinodai points are unstable and can decompose into two coherent phases  $\alpha_1$  and  $\alpha_2$  without overcoming an activation energy barrier. Alloys between the coherent miscibility gaps and the spinodai are metastable and can decompose only after nucleation of the other phase. [101]

**Figure 2.1.** TEM images of  $\text{Al}_x\text{CoCrCuFeNi}$  HEAs: TEM images of  $\text{Al}_x\text{CoCrCuFeNi}$  HEAs: (a) High-magnification brightfield image of  $\text{Al}_0\text{CoCrCuFeNi}$ , the corresponding electron diffractions presented in insets (Fig. 2.1b and c); (d) High-magnification bright-field image of  $\text{Al}_2\text{CoCrCuFeNi}$ , magnification insets (e–g), the corresponding electron diffractions presented in insets (Fig. 2.1h–j). [15]

**Figure 2.2.** SEM microstructures of (a) and (b)  $\text{AlCoCrCuFeNi}$ , (c) and (d)  $\text{Al}_{0.5}\text{CoCrCuFeNi}$ , (e) and (f)  $\text{AlCo}_{0.5}\text{CrCuFeNi}$ , (g) and (h)  $\text{AlCoCr}_{0.5}\text{CuFeNi}$ , (i) and (j)  $\text{AlCoCrCu}_{0.5}\text{FeNi}$ , (k) and (l)  $\text{AlCoCrCuFe}_{0.5}\text{Ni}$ , and (m) and (n)  $\text{AlCoCrCuFeNi}_{0.5}$  (DR: dendrite, ID: interdendrite, SD: spinodal decomposition). [16]

**Figure 2.3.** Mechanical properties of  $\text{Fe}_x\text{CoNiCu}$  alloys: (a) relationship between hardness and Fe content of  $\text{Fe}_x\text{CoNiCu}$  alloys; (b) engineering stress-strain curves of  $\text{Fe}_x\text{CoNiCu}$  alloys; (c) statistics of the tensile strength and the elongation of  $\text{Fe}_x\text{CoNiCu}$  alloys. [19]

**Figure 2.4.** Engineering tensile stress-strain curves of the as-cast  $\text{CoCrFeNiNb}_x$  ( $x = 0, 0.103, 0.155, 0.206, 0.309$  and  $0.412$ ) alloys at room temperature. [20]

**Figure 2.5.** (a) Vickers hardness and total crack length of  $\text{AlCoCrFeMo}_{0.5}\text{Ni}_x$  alloys as functions of Ni content; and (b) those of  $\text{Al}_x\text{CoCrCuFeNi}$  alloys for comparison with (a). [26]

**Figure 2.6.** Vickers hardness and wear resistance of  $\text{Al}_{0.5}\text{CoCrCuFeNiV}_x$  alloys with different vanadium contents. [27]

**Figure 2.7.** The comparison of the wear resistance and hardness of  $\text{Al}_{0.5}\text{CoCrCuFeNiV}_x$  ( $x = 0.2 - 2.0$  with  $0.2$  difference in atomic ratio) and  $\text{Al}_y\text{CoCrCuFeNi}$  ( $y = 0.2, 0.4, 0.6$ ) HEA alloys. [27]

**Figure 2.8.** Wear surface profilometry after pin-on-disc wear testing of  $\text{CoCrFeMnNi}$  at: (a) room temperature, (b)  $300\text{ }^\circ\text{C}$ , (c)  $600\text{ }^\circ\text{C}$ , and (d)  $900\text{ }^\circ\text{C}$ . The corresponding profilometry of  $\text{Al}_{0.3}\text{CoCrFeNi}$ ,  $\text{Al}_{0.6}\text{CoCrFeNi}$  and  $\text{AlCoCrFeNi}$  are shown in (e–h), (i–l) and (m–p), respectively. [28]

**Figure 2.9.** SEM-EDS map of the cross-section of the oxide scale formed on: (a)  $\text{CoCrFeMnNi}$ , (b)  $\text{Al}_{0.3}\text{CoCrFeNi}$ , (c)  $\text{Al}_{0.6}\text{CoCrFeNi}$ , (d)  $\text{AlCoCrFeNi}$ , and (e) Inconel 718 during dry sliding wear testing at  $900\text{ }^\circ\text{C}$  (away from the wear track). [28]

**Figure 2.10.** Wear loss of (a)  $\text{AlCoCrFeNi}$  and (b), caused by wear tests with and without the airflow (standard deviation). [29]

**Figure 2.11.** Temperature dependencies of the 0.2% offset yield strengths of the CrMnFeCoNi (HE-1) and CrFeCoNi (HE-4) alloys tensile tested at engineering strain rates of  $10^{-3} \text{ s}^{-1}$  (a), and  $10^{-1} \text{ s}^{-1}$  (b). Variations in ultimate tensile strength and yield strength for the two alloys are shown in (c) and strain rates investigated in this study. To first order, the small variations between the two alloys and strain rates are ignored, so only one dashed curve is drawn (as a guide to the eye) through each data set [45]

**Figure 2.12.** (a) Temperature dependence of the tensile ductilities of CrMnFeCoNi (HE-1) and CrFeCoNi (HE-4) tested at an engineering strain rate of  $10^3 \text{ s}^{-1}$ . Also shown are fractography of specimens tested at  $-196 \text{ }^\circ\text{C}$  (b, c) and  $400 \text{ }^\circ\text{C}$  (d, e). The dashed outlines of the fracture surfaces show that there is less thickness reduction (necking) at  $-196 \text{ }^\circ\text{C}$  (b) than at  $400 \text{ }^\circ\text{C}$  (e). [45]

**Figure 2.13.** True stress-strain curves of tensile tests at 77 K and 293 K of (a) CrCoNi medium-entropy alloy and (c) CrMnFeCoNi high-entropy alloy. Curves with arrows at the end are from specimens tested to fracture while the other curves in (a) are from interrupted tests. Work hardening rate ( $ds/d\varepsilon$ ) versus true stress of (b) CrCoNi and (d) CrMnFeCoNi. [46]

**Figure 2.14.** (a) Engineering stress-strain curves of the  $(\text{CoCrNi})_{100-x}\text{Mo}_x$  alloys after annealing at  $900^\circ\text{C}$  and (b) comparison of mechanical properties of Mo-3 alloy with reported single-phase FCC-HEAs and TRIP-DP-HEAs. [47]

**Figure 2.15.** Corrosion performance in HCl solutions (a) potentiodynamic polarization curves of high-entropy alloy, 304 SS and Q235 steel (b) cyclic polarization curve of  $\text{Al}_2\text{CrFeCo}_{0.5}\text{CuNiTi}$  high-entropy alloy coating. [37]

**Figure 2.16.** Corrosion performance of GTA cladded AlCoCrFeNi HEA coatings. (a) Open circuit potential; (b) Potentiodynamic polarization; (c) Nyquist plot; (d) Equivalent circuit. [38]

**Figure 2.17.** XRD result of each of different Fe content AlCoCrFeNi. [38]

**Figure 2.18.** Potentiodynamic polarization curves of AlCoCrFeNi, AlCrFeCoNiTi<sub>0.5</sub> and 316SS in (a) 3.5 wt.% NaCl and (b) HCl (pH = 3) solutions. [69]

**Figure 2.19.** SEM images of worn surface at the sliding distance of 36 m in (left) 3.5 wt.% NaCl solution and (right) HCl (pH = 3) solution: (a) and (b) AlCoCrFeNi; (c) and (d) AlCrFeCoNiTi<sub>0.5</sub>; (e) and (f) 316SS; BSD images of worn surfaces of (g) AlCoCrFeNi and (h) AlCrFeCoNiTi<sub>0.5</sub> worn in 3.5 wt.% NaCl solution. [69]

**Figure 2.20.** OM images of (a) CoCrNi, (b) CoCrFeMnNi, and (c) SS 304 from cross-sectional areas after oxidation at  $1100 \text{ }^\circ\text{C}$  for 24 h. [70]

**Figure 2.21.** Potentiodynamic polarization curves of CoCrNi MEA and 316 L SS. [71]

**Figure 2.22.** Corrosion rates of CoCrNi MEA and 316 L after immersion test in 3.5 wt% NaCl solution. [71]

**Figure 2.23.** True tensile stress-strain of Ti–Zr–Nb MEAs at room temperature, and the inset at bottom left is the schematic diagram and size of the tensile specimen, the inset at bottom right is the EBSD of Ti33-33 near the fracture. [80]

**Figure 2.24.** Potentiodynamic curves of Ti–Zr–Nb MEAs and Ti6Al4V alloy in the PBS solution at  $37 \pm 0.5$  °C. The inset is the enlarged part of the curves from -0.65 V to -0.3 V. [80]

**Figure 3.1.** SEM images of (a) AlCoCrFe, (b) AlCoCrFeNi<sub>0.5</sub>, (c) AlCoCrFeNi<sub>1.0</sub>, (d) AlCoCrFeNi<sub>1.5</sub>, (e) AlCoCrFeNi<sub>2.0</sub>. A closer image of AlCoCrFeNi<sub>1.0</sub> with larger magnification is inserted in (c).

**Figure 3.2.** (a) TEM bright field images showing morphologies of AlCoCrFe sample; electron diffraction patterns of (b) an ordered BCC phase and (c) a disordered BCC phase; (d) a high-resolution atomic image showing the two phases.

**Figure 3.3.** EDX elemental maps showing the distribution of Al, Cr, Fe, and Co in AlCoCrFe medium-entropy alloy. As shown, there are two domains, one is Cr-Fe-rich (bright domain) and the other is Al-Co-rich (dark domain)

**Figure 3.4. A** - a TEM image of AlCoCrFeNi<sub>1.0</sub>, and diffraction patterns of two phases in the alloy. **B** -EDX elemental maps showing the distribution of Al, Cr, Fe, Co, and Ni.

**Figure 3.5. A** - a TEM image of AlCoCrFeNi<sub>2.0</sub>, which contains two distinctive type domains, one of which is an ordered BCC phase and the other is a FCC phase; inside the ordered BCC phase, there are nanoparticles; **B** – EDX maps of element distributions in the ordered BCC and FCC phases.

**Figure 3.6.** (a) a TEM image of the ordered BCC phase (B2) in AlCoCrFeNi<sub>2.0</sub>, within which nanoparticles are present; (b) a HRTEM image showing nanoparticles and the B2 matrix: the dashed squares A and B were used for fast Fourier transform (FFT) processing. The corresponding diffractograms, displayed just below image (a), indicate that the nanoparticle has a disorder BCC structure while the matrix is B2. (c) a STEM dark-filed image and EDX maps of element distributions in the nanoparticles and the ordered BCC matrix.

**Figure 3.7.** Vickers hardness test of AlCoCrFeNi<sub>x</sub> (x= 0, 0.5, 1.0, 1.5, 2.0) compared with commercial stainless steel 316 in HRA (load is 60kgf).

**Figure 3.8.** Nano/micro-indentation tests on (a) AlCoCrFe, (b) AlCoCrFeNi<sub>1.0</sub>, (c) AlCoCrFeNi<sub>1.5</sub>, and (c) AlCoCrFeNi<sub>2.0</sub>.

**Figure 3.9.** Compression stress ~ strain curves of AlCoCrFeNi<sub>x</sub> with x =0, 0.5, 1.0, 1.5, 2.0.

**Figure 3.10.** Wear loss of the alloys caused by (a) dry wear test without airflow and (b) dry wear test with airflow. The airflow was used to minimize the effect of frictional heat on wear.

**Figure 3.11.** The SEM images of wear tracks on (a) AlCoCrFe, (b) AlCoCrFeNi<sub>1.0</sub> and (c) AlCoCrFeNi<sub>2.0</sub>., caused by wear tests with and without the airflow cooling.

**Figure 4.1.** (a) Corrosion currents of AlCoCrFeNi<sub>x</sub> in acidic solution of pH=3 (x = 0, 0.5, 1.0, 1.5, 2.0); (b) Polarization curves of the alloys in the acidic solution.

**Figure 4.2.** (a) Results of impedance measurements for AlCoCrFeNi<sub>x</sub> (x = 0, 0.5, 1.0, 1.5, 2.0) in the acidic solution; (b) Equivalent circuits used to model the impedance data.

**Figure 4.3.** Volume losses of AlCoCrFeNi<sub>x</sub> (x = 0, 0.5, 1.0, 1.5, 2.0) caused by wear under a load of 5N in acidic solution of pH=3.

**Figure 4.4.** Wear tracks of (a) AlCoCrFe, (c) AlCoCrFeNi<sub>0.5</sub>, (d) AlCoCrFeNi<sub>1.0</sub>; Cracks and pits are visible on the worn surface of AlCoCrFe. (b) a cross-sectional profile of wear track on AlCoCrFe, which shows the depth of two relatively large pits.

# List of Symbols

Symbols are arranged in the order of appearing in this thesis.

$\Delta S_{\text{mix}}$	Entropy of mixing
R	Gas content
N	Quantity of elements components
$c_i$	atomic fraction of each component
$\Delta G$	Gibbs free energy
$\Delta H$	Enthalpy
T	Temperature
K	Kelvin
$\sigma$	solution-type intermediate phase
GPa	Gigapascals
V	Electrical potential
Hv	Vickers hardness
pH	Potential of hydrogen
$\Delta E$	Potential differences

mV	microvolt
Hz	Hertz
N	Newton
rpm	rotation per minute
$i_{\text{corr}}$	corrosion current
$i_p$	Passive current density
$\eta_p$	Width of passive region
$E_p$	Pitting potential
$R_s$	the resistance of the solution
$R_f$	resistance of the corrosion product film
$C_f$	capacitance of the corrosion product film
$R_{ct}$	resistance to charge transfer
$C_{dl}$	capacitance of the double layer
eV	electronvolt

# List of Abbreviations

BCC	Body-Centered Cubic
BSD	Backscattered Electron Detector
CPE	Constant-Phase Elements
EDX	Energy Dispersive X-Ray Analysis
EIS	Electrochemical impedance spectroscopy
EFW	Electron Work Function
FCC	Face-Centered Cubic
HCP	Hexagonal-Close Packed
HEA	High-Entropy Alloys
HRTEM	high-resolution transmission electron microscopy
MEA	Medium-Entropy Alloys
OCP	Open Circuit Potential
SCE	Saturated Calomel Electrode
SEM	Scanning Electron Microscope
SS	Stainless Steel

TEM	Transmission Electron Microscopy
WEDM	Wire Electrical Discharge Machine
XRD	X-Ray Powder Diffraction

# Chapter 1: Introduction

The development of materials technology today is focused on how to minimize the weight and maximize material ability for various applications, such as strength, corrosion resistance, wear resistance, etc. The high-entropy alloys (HEA) are promising for meeting the requirements. Compared to the conventional materials such as stainless steel or carbon steel, HEAs show improved mechanical behavior with superior anti-corrosion ability over many conventional alloys including stainless steel.

High-entropy alloys are defined as an alloy consisting of five or more elements with the concentration of each element in the range of 5% and 35%. [1, 2]. The word “high-entropy” is based on the mixing entropy of the alloys which can be calculated with the following equation [1]:

$$\Delta S_{mix} = -R \sum_{i=1}^N c_i \ln c_i$$

which R is the gas constant, N is the quantity of elements and  $c_i$  is the atomic fraction of each element. An alloy having its entropy larger than  $1.5R$  is considered as a high-entropy alloy, and alloys' entropy between  $1.5R$  and  $R$  is regarded as a medium-entropy alloy [3]. An equimolar five-element HEA has its entropy equal to  $1.61R$ . According to the Gibbs free energy equation,  $\Delta G = \Delta S - T\Delta S$ , a higher entropy will make the overall free energy lower at high temperatures, thus reducing phases inside the alloys and making it more thermodynamically stable. Higher thermodynamic stability benefits the performance of HEA with desired physical properties.

Theoretically, HEAs are in a solid solution state with multi-elements, which can be hardened through solid-solution hardening mechanism. The crystal structure (BCC, FCC, and HCP) influences on the mechanical properties such as hardness [4], since it affects the availability of slip systems. Some brittle phases or intermetallic compounds could occur inside HEAs, which can lower the resistance to fracture [5]. Selecting specified elements with bigger atomic size could reduce the phases inside the HEA and the solid-solution state could be achieved to have promising properties like high ductility with desired hardness partially due to increased lattice distortion, high corrosion resistance, and high wear resistance [3, 5, 6, 80]. The high corrosion resistance of HEAs is benefited by the passive elements inside HEAs such as Ti, Al, and Cr, which help form passive films [7-10]. The selection of materials in HEA is important as it manipulates the properties of the HEA. Although selection of elements for HEAs is often based on trial-and-error tests, some promising parameters or factors could be used. One of such factors for element selection is the electron work function (EWF), which has been shown [11-13] effective in selecting elements to strengthen materials by strengthening their metallic bonds. As an example, high-EWF element, Ni, can be used to reach a higher level of solid-solution hardening, which also benefits the anti-corrosion ability of alloys [14] due to the increased stability of the atomic bonds.

In HEAs, spinodal decomposition is often observed, which has strong influence on mechanical properties of HEAs. The spinodal decomposition also occurs in the HEA under this present study. Spinodal decomposition is the spontaneous splitting of a single phase into two phases without barrier to nucleation [101], accompanied with decrease of the total free energy. Considering an bi-element alloy (A-B) in single phase at high temperatures with a composition  $X_0$  as an example, this single phase becomes unstable as temperature decreases and split into A-

rich and B-rich domains with lowered free energy. Such a transformation may involve “up-hill” diffusion and “down-hill” diffusion without nucleation until the compositions of  $X_1$  and  $X_2$  are reached, as shown in Fig. 1.

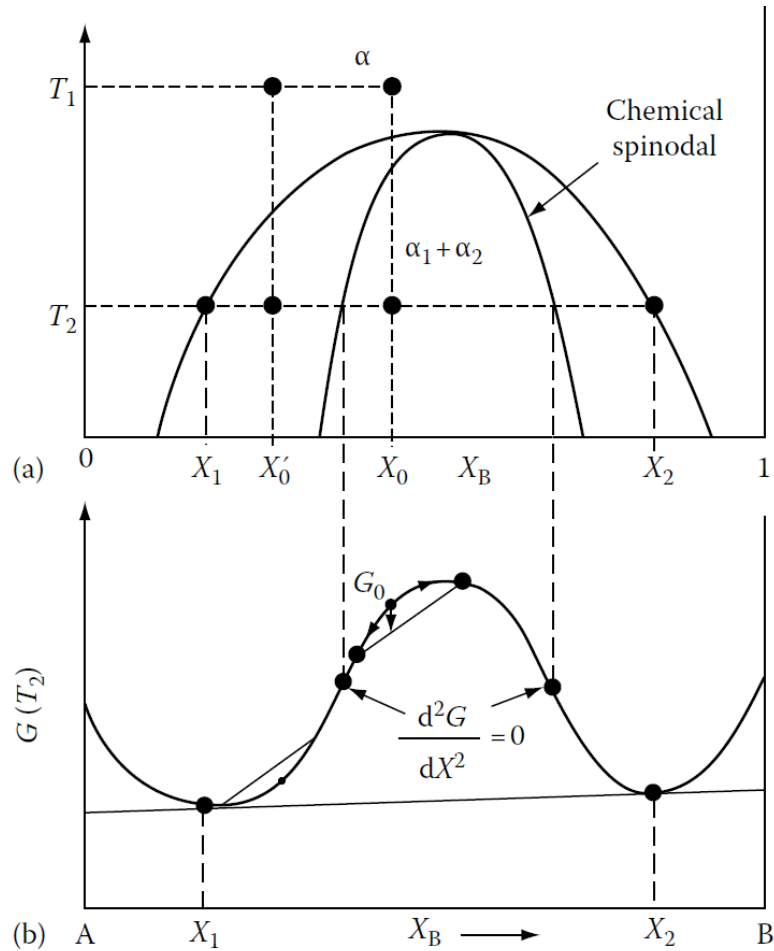


*Fig. 1. Illustration of spinodal decomposition; a single-phase alloy becomes unstable as temperature decreases and decompose into two coherent phases  $\alpha_1$  and  $\alpha_2$  without overcoming an activation energy barrier [101]*

The studies of medium-entropy alloys with less elements show that the medium-entropy alloys are also promising [39 - 45, 71 - 78] for industrial applications with lower costs and less complicated microstructure. In this study, mechanical properties, tribological performances, and

tribo-corrosion of a medium-entropy alloy, AlCoCrFe and corresponding high-entropy alloys, AlCoCrFeNi<sub>x</sub> (x: 0~2), are investigated and compared with the aim of providing useful information for potential industrial applications. This thesis has the following structure: Chapter 1&2 present the background of HEAs and MEAs and their mechanical and anti-corrosion properties. The studies conducted in this thesis research on the mechanical properties including hardness, compression behavior, and wear resistances of both HEAs and MEA are reported in Chapter 3. The electrochemical behaviors, including potentiodynamic polarization test, impedance test and tribo-corrosion of the HEAs and MEA, are presented and discussed in Chapter 4. Chapter 5 gives general conclusions from this research and potential future studies.

# Chapter 2: Literature Review

This chapter introduces relevant experimental observations on how the content of nickel and those of other elements affect the microstructure of the medium-entropy alloy AlCoCrFe and corresponding changes in mechanical properties such as hardness, wear, and tensile strength. Besides, effects of the Ni content on the anti-corrosion ability or corrosive wear resistance are also introduced.

## 2.1 Microstructure and the content of elements of the alloys

### 2.1.1 Change in microstructure with the composition and corresponding mechanical properties of HEAs

Properties of HEA alloys are strongly affected by their microstructures, which are dependent on the composition and can also be altered by heat treatment. This chapter presents some case studies to microstructural variation in high-entropy alloys with the content of elements through detailed observations with transmission electron microscopy. For example, Liu et al. studied the effect of aluminum content in  $Al_xCoCrCuFeNi$  high-entropy alloys on their microstructure and properties. Fig. 2.1 shows TEM images of  $Al_0CoCrCuFeNi$ , compared with those of  $Al_2CoCrCuFeNi$ , with electron diffraction patterns depicting the difference in phase [15] showing that the fraction of BCC phase increase with the increasing content of Al.

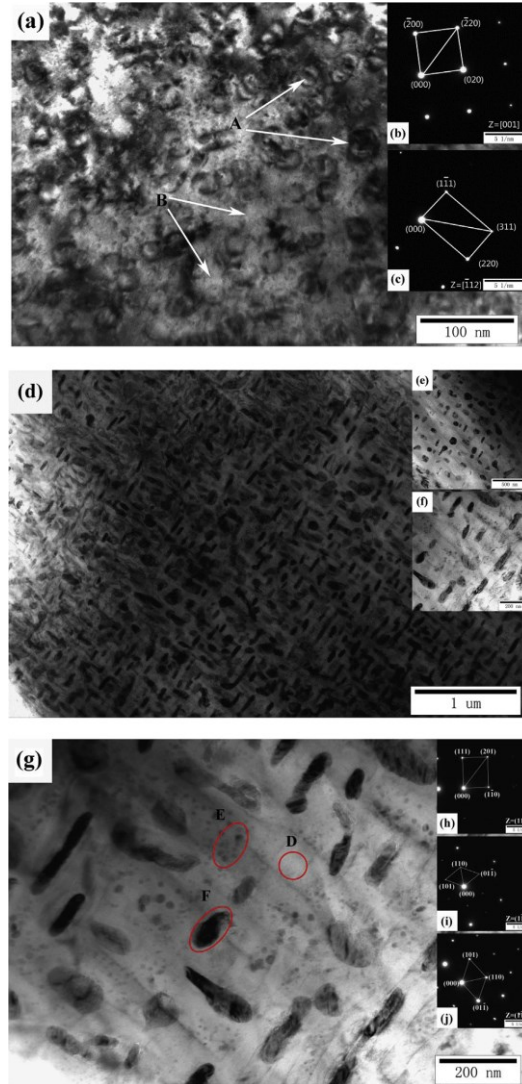


**Fig. 2.1.** TEM images of  $Al_xCoCrCuFeNi$  HEAs: TEM images of  $Al_xCoCrCuFeNi$  HEAs: (a) High-magnification brightfield image of  $Al_0CoCrCuFeNi$ , the corresponding electron diffractions presented in insets (Fig. 2.1b and c); (d) High-magnification bright-field image of  $Al_2CoCrCuFeNi$ , magnification insets (e–g), the corresponding electron diffractions presented in insets (Fig. 2.1h–j) [15].

Tung et al. [16] discovered that the elements of Co, Cu, and Ni promoted the formation of a FCC phase while Al and Cr promoted the formation of a BCC phase in the AlCoCrCuFeNi HEA system when each of the elements changed to a half of its original content. Fig. 2.2 shows corresponding SEM images of the AlCoCrCuFeNi HEA with the change of its composition. The

BCC phase helps increasing hardness of the HEA based on properties of the BCC structured phase.

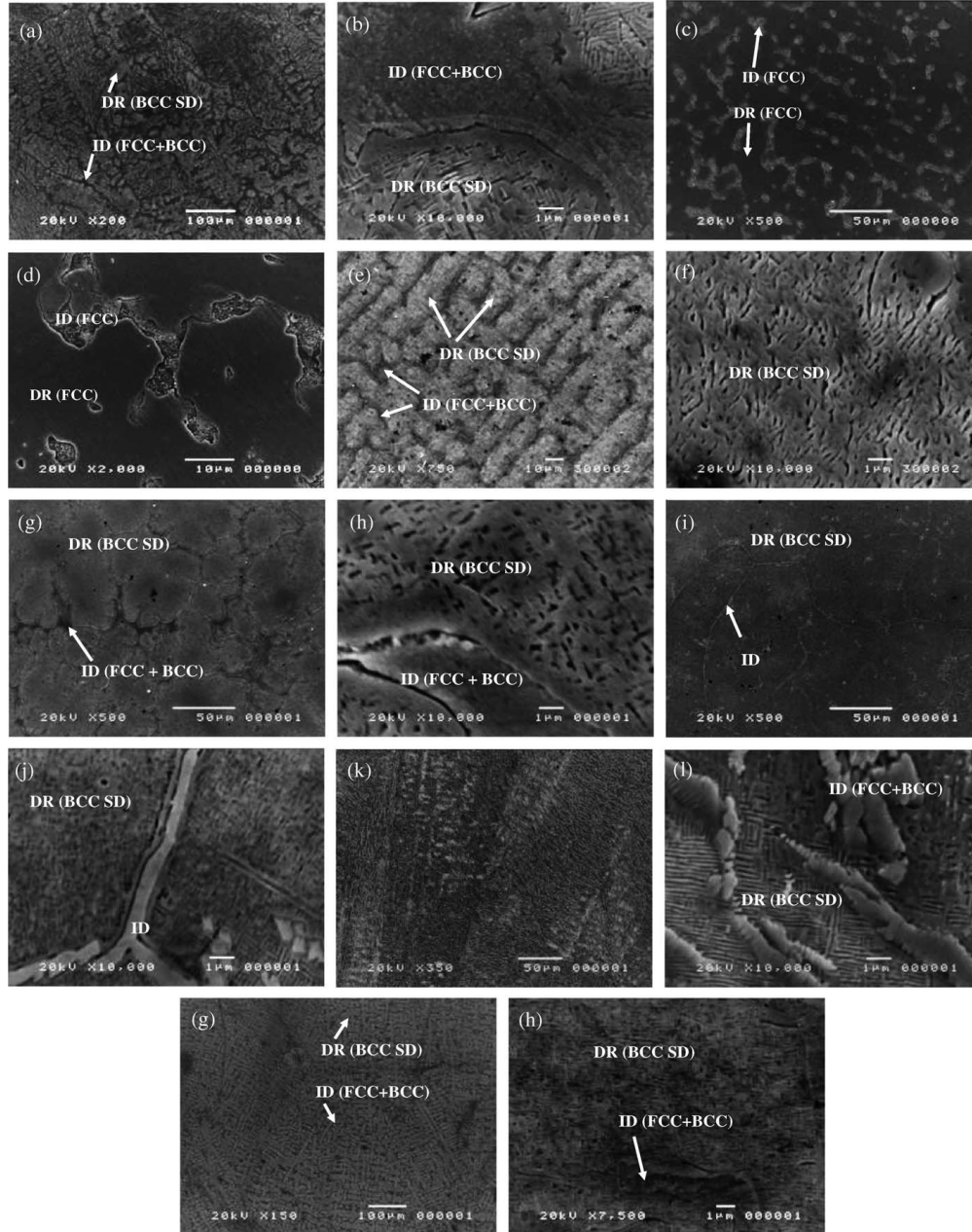


**Fig. 2.2.** SEM microstructures of (a) and (b)  $AlCoCrCuFeNi$ , (c) and (d)  $Al_{0.5}CoCrCuFeNi$ , (e) and (f)  $AlCo_{0.5}CrCuFeNi$ , (g) and (h)  $AlCoCr_{0.5}CuFeNi$ , (i) and (j)  $AlCoCrCu_{0.5}FeNi$ , (k) and (l)  $AlCoCrCuFe_{0.5}Ni$ , and (m) and (n)  $AlCoCrCuFeNi_{0.5}$  (DR: dendrite, ID: interdendrite, SD: spinodal decomposition) [16].

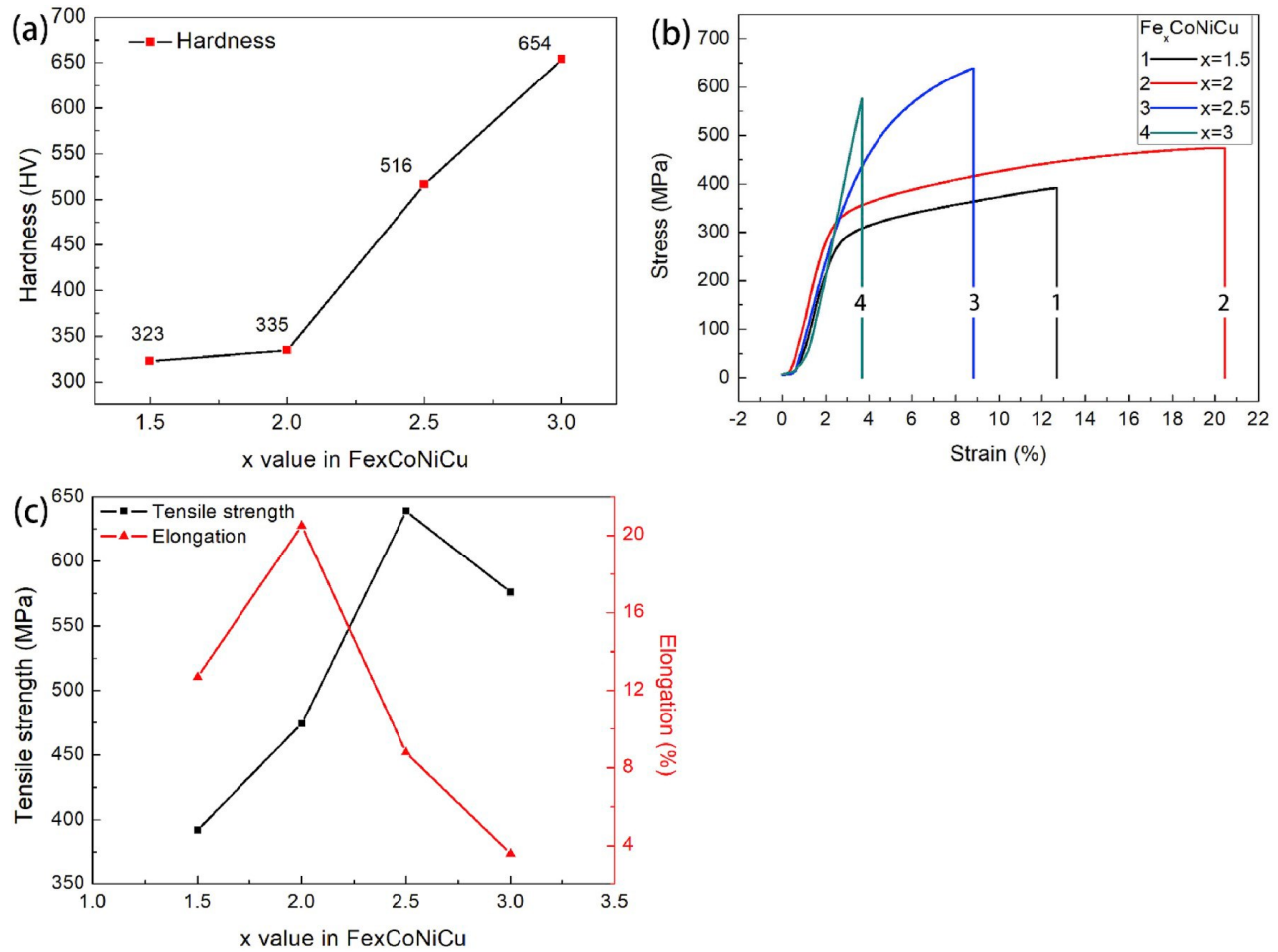


**Fig. 2.3.** Mechanical properties of  $Fe_xCoNiCu$  alloys: (a) relationship between hardness and Fe content of  $Fe_xCoNiCu$  alloys; (b) engineering stress-strain curves of  $Fe_xCoNiCu$  alloys; (c) statistics of the tensile strength and the elongation of  $Fe_xCoNiCu$  alloys [19]

The change of microstructure certainly resulted in changes in mechanical properties of the HEAs, such as hardness and yield strength. As an example, the hardness of high-entropy  $Fe_{36}Ni_{18}Mn_{33}Al_{13})_{100-x}Ti_x$  alloys increases with increasing the Ti content [17]. Increasing the Ni content [18] in  $Al_2CrFeCoCuTiNi_x$  increases the fraction of its BCC phase which is harder than its FCC phase, and the Al content [15, 22-25] also shows such an effect. Medium-entropy alloy [19], e.g.,  $Fe_xCoNiCu$ , increases its hardness with the Fe content, as Fe induces a change from a

single FCC phase to FCC+BCC phase when the Fe content increases from  $x=1.5$  to  $3.0$ , as Fig. 2.3 illustrates. The increase in tensile strength can be related to the addition of specific elements such as Nb [20] added to CoCrFeNi alloys as shown in Fig. 2.4. The addition of elements may also make the alloys weaker than the original ones, depending on the added element. For example, Hsu et al. [25] showed that the addition of Co, which was a FCC phase stabilizer, led to a phase change from BCC+  $\sigma$  to BCC+FCC+  $\sigma$ , resulting in a decrease in the mechanical strength. Juan et al. [26] showed a similar case, in which increasing the Ni content in AlCoCrFeMo<sub>0.5</sub>Ni<sub>x</sub> ( $x = 0-2$ ) led to a phase change from B2 +  $\sigma$  to B2 + FCC +  $\sigma$ , accompanied with a decrease in hardness as Fig. 2.5 illustrates. Usually, the BCC structure is theoretically harder than the FCC structure.

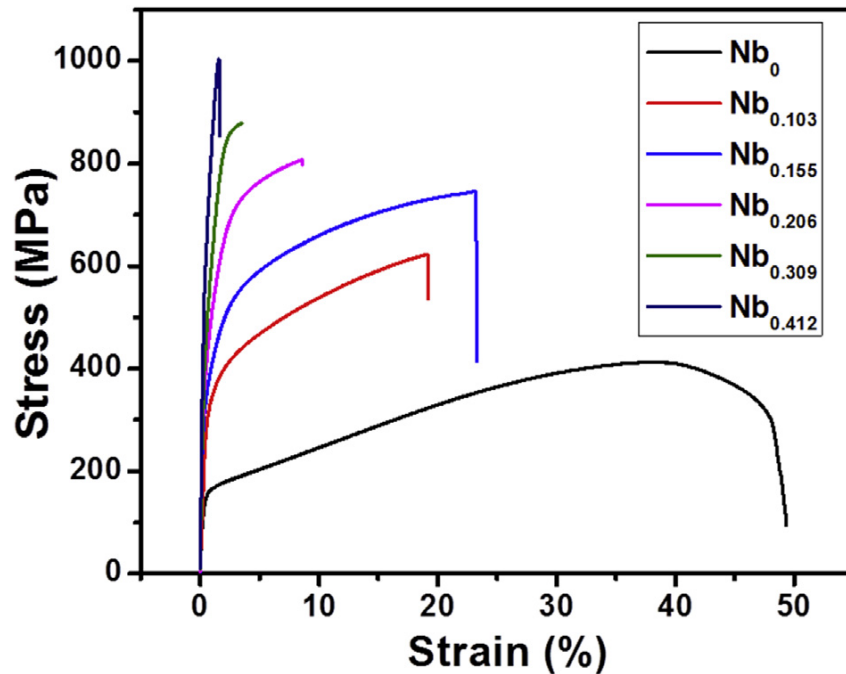


**Fig. 2.4.** Engineering tensile stress-strain curves of the as-cast CoCrFeNiNb<sub>x</sub> ( $x = 0, 0.103, 0.155, 0.206, 0.309$  and  $0.412$ ) alloys at room temperature [20]

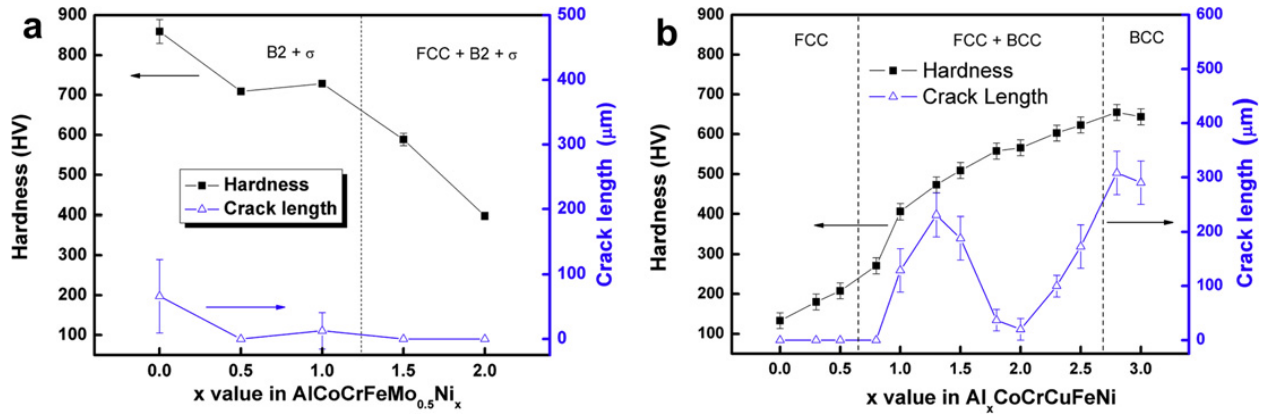


**Fig. 2.5.** (a) Vickers hardness and total crack length of  $\text{AlCoCrFeMo}_{0.5}\text{Ni}_x$  alloys as functions of Ni content; and (b) those of  $\text{Al}_x\text{CoCrCuFeNi}$  alloys for comparison with (a). [26]

## 2.1.2 The wear behavior of HEAs with the alteration of elements

Hardness strongly affects the wear resistance of an alloy. HEAs with a larger fraction of BCC phases are usually harder with higher wear resistance [4, 19, 30-36]. Although HEAs may present some exceptional properties, the hardness plays a predominant role in determining the wear resistance of HEAs.

Chen et al. [27] investigated HEA alloys,  $\text{Al}_{0.5}\text{CoCrCuFeNi}$  and  $\text{Al}_{0.5}\text{CoCrCuFeNiV}_x$ , in terms of their hardness and wear resistance (see Figs. 2.6 and Fig. 2.7). When the alloys mainly contain BCC phases, their hardness is high. With increasing the V content,  $\text{Al}_{0.5}\text{CoCrCuFeNiV}_x$  changes its structure from a simple FCC solid solution to a complex structure dominated by BCC dendrites through spinodal decomposition. As a result of the structural change, hardness and wear resistance of this alloy increase.

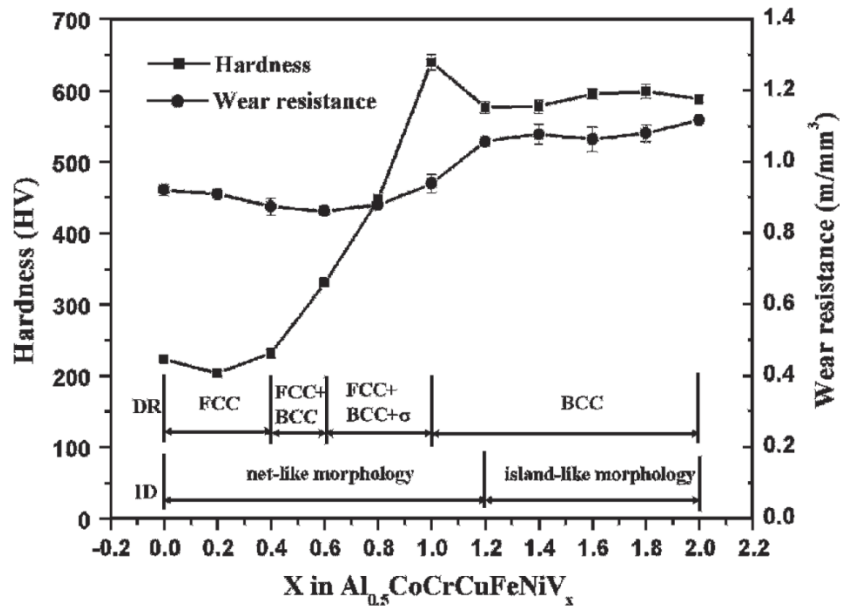


Fig. 2.6 Vickers hardness and wear resistance of  $Al_{0.5}CoCrCuFeNiV_x$  alloys with different vanadium contents. [27]

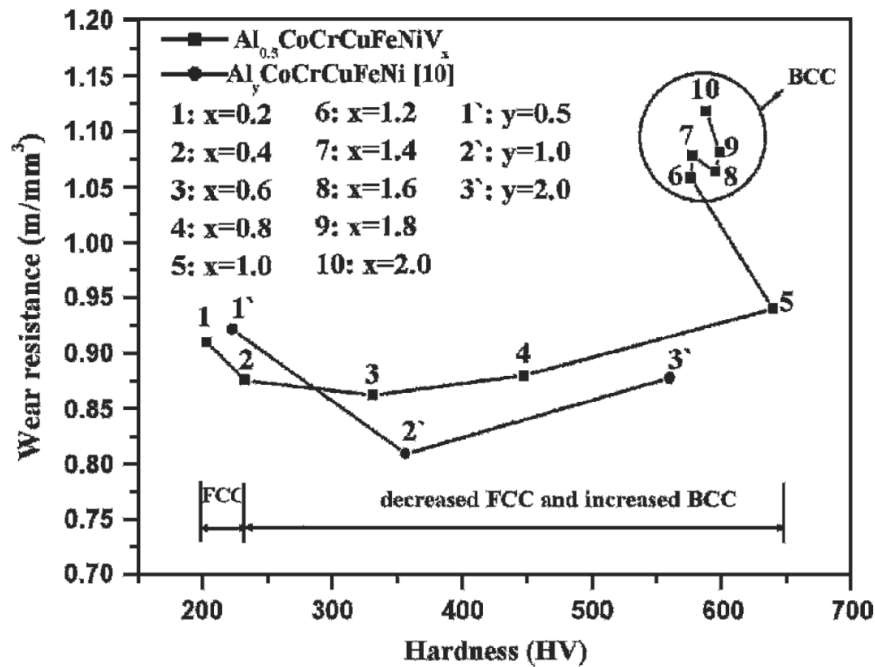
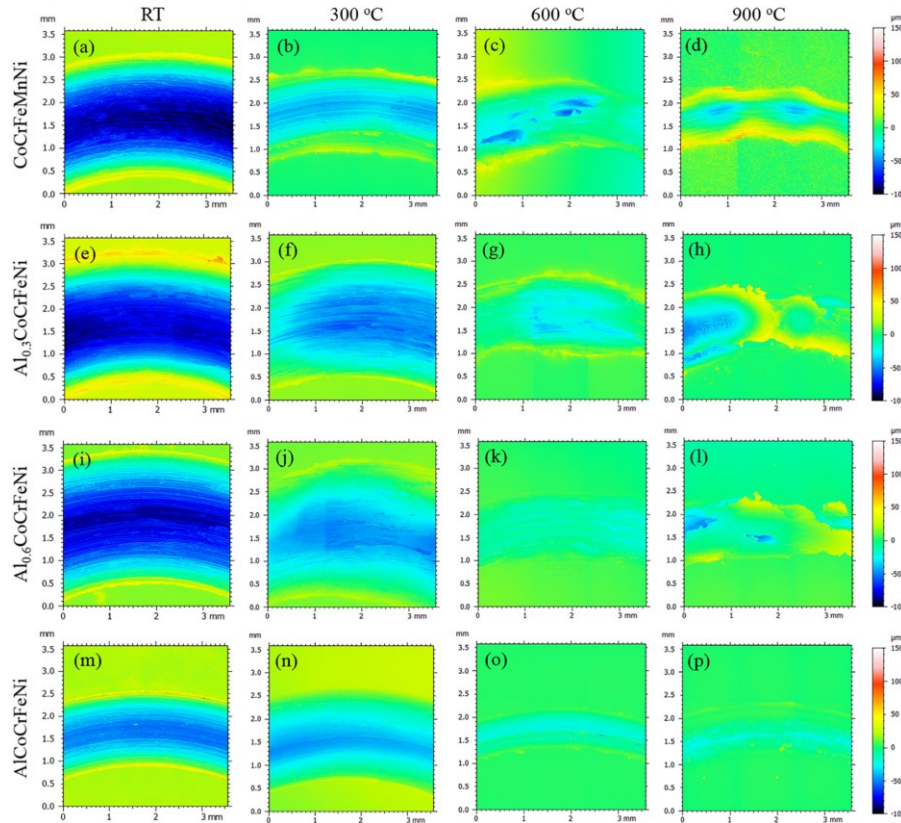
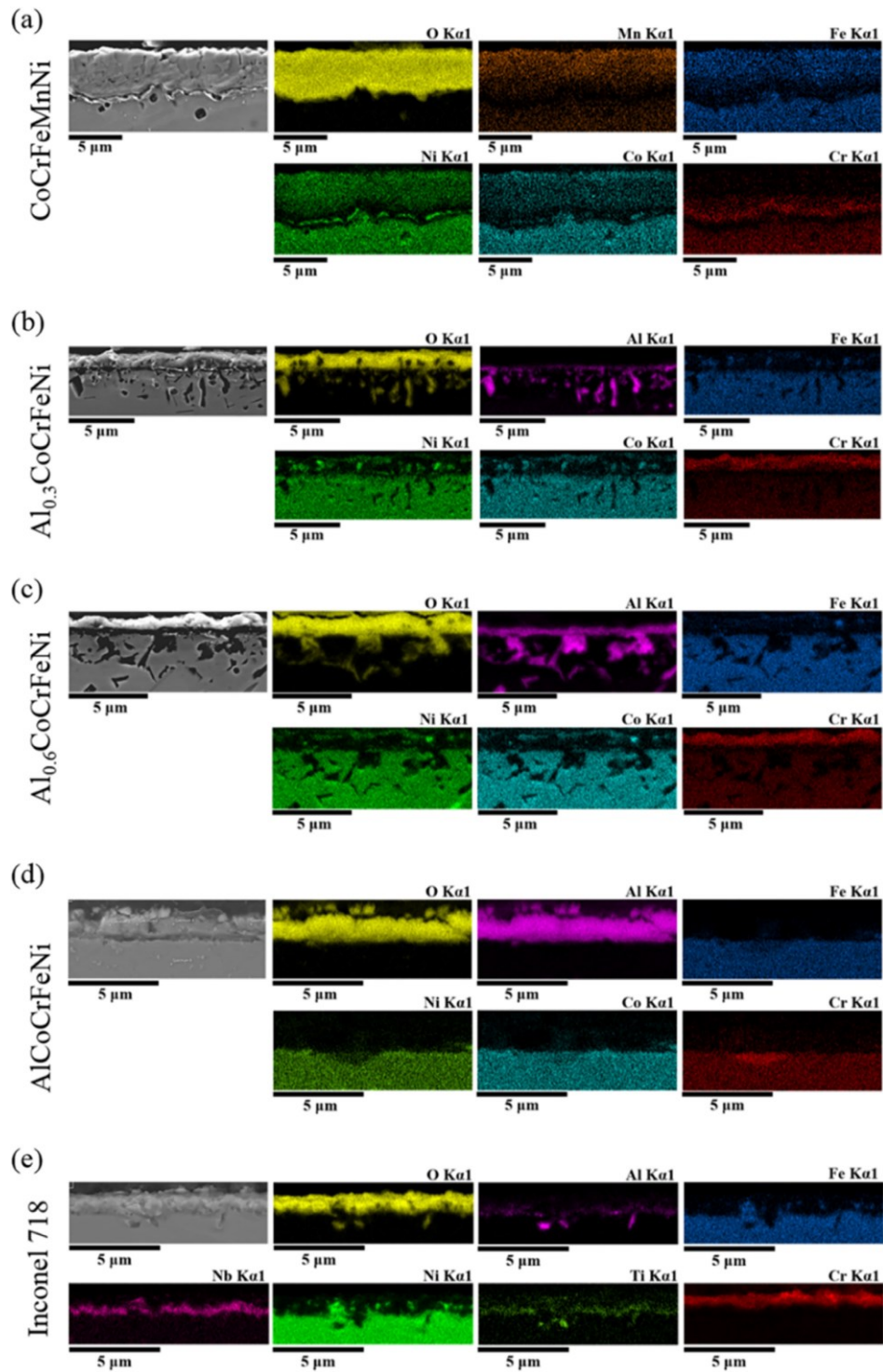


Fig. 2.7 The comparison of the wear resistance and hardness of  $Al_{0.5}CoCrCuFeNiV_x$  ( $x = 0.2 - 2.0$  with 0.2 difference in atomic ratio) and  $Al_yCoCrCuFeNi$  ( $y = 0.2, 0.4, 0.6$ ) HEA alloys [27]

Jithin et al. [28] investigated tribological properties of CoCrFeMnNi and  $Al_x$ CoCrFeNi HEAs under sliding wear condition at temperatures within a range of from 25 °C to 900 °C, and showed that the relationships among the phase structure, hardness and wear resistance of the high-entropy alloys. Besides, the oxide films formed on the high-entropy alloys affects their wear resistance by providing surface protection to a certain degree. Fig. 2.8 shows the worn surface profilometry of the alloys and Fig. 2.9 presents cross-sectional SEM-EDX images and composition maps of the alloys at 900 °C, demonstrating that the oxide layer can act as a protective layer for the alloys.

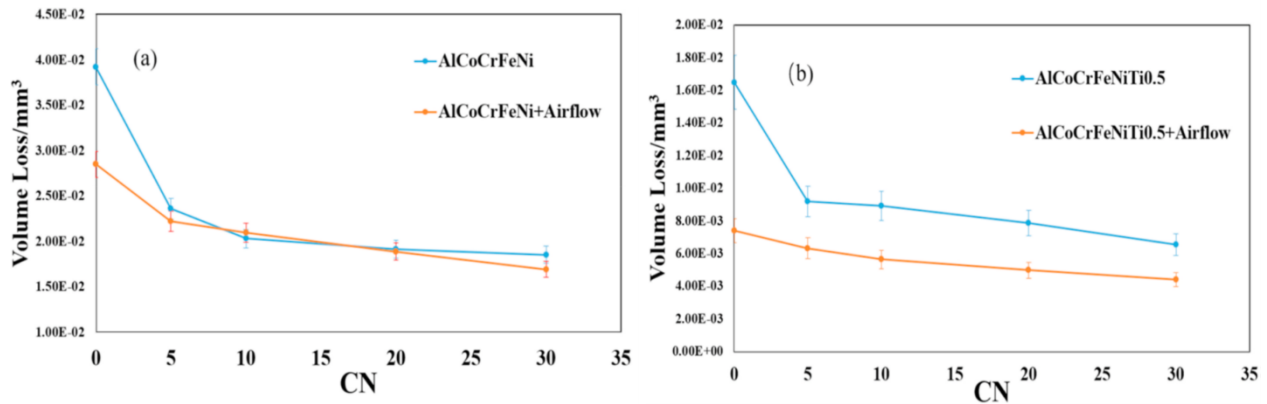


**Fig. 2.8** Wear surface profilometry after pin-on-disc wear testing of CoCrFeMnNi at: (a) room temperature, (b) 300 °C, (c) 600 °C, and (d) 900 °C. The corresponding profilometry of  $Al_{0.3}CoCrFeNi$ ,  $Al_{0.6}CoCrFeNi$  and  $AlCoCrFeNi$  are shown in (e–h), (i–l) and (m–p), respectively [28]



**Fig. 2.9.** SEM-EDS map of the cross-section of the oxide scale formed on: (a) CoCrFeMnNi, (b)  $Al_{0.3}CoCrFeNi$ , (c)  $Al_{0.6}CoCrFeNi$ , (d) AlCoCrFeNi, and (e) Inconel 718 during dry sliding wear testing at 900 °C (away from the wear track) [28].

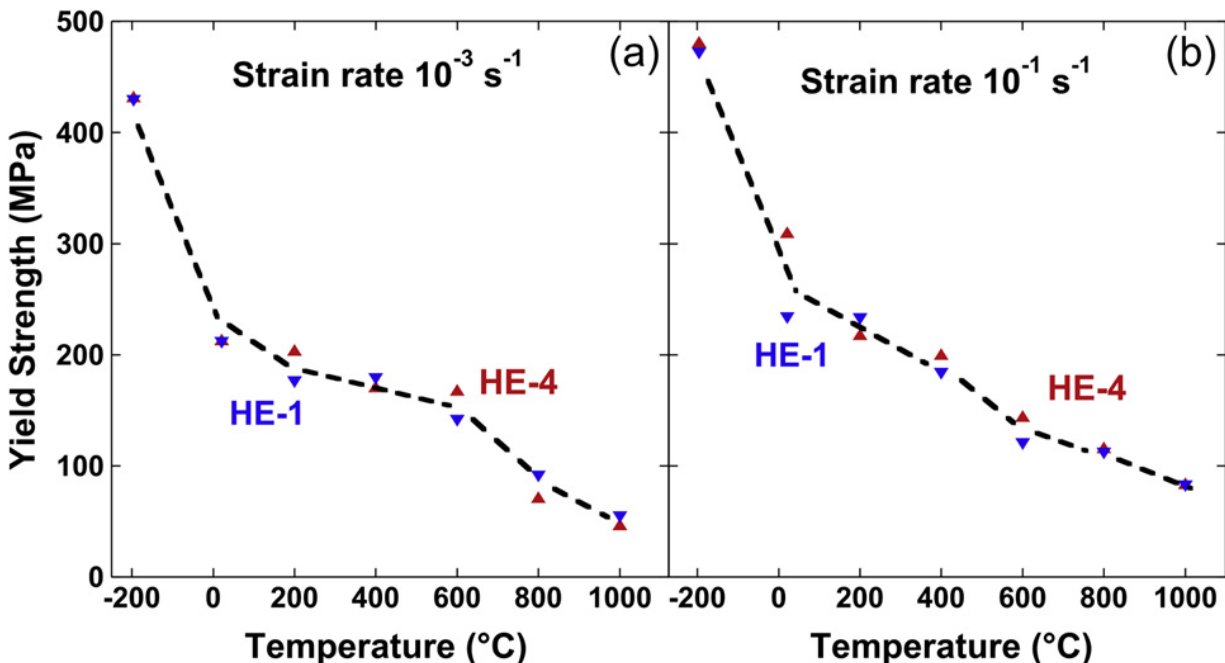
The oxide scale formed on HEAs caused by frictional heating may not always protective, which is dependent on the type and properties of the oxide. Xu et al. [29] studied the effect of Ti in the tribological properties of AlCoCrFeNi HEA with the airflow during wear testing to reduce frictional heating in order to evaluate the effect of oxidation on the wear resistance. The airflow reduced the frictional heat on the surface, helping reduce the formation of oxide scale and also reduce the surface softening due to the rise of surface temperature. Fig. 2.10 shows the wear losses of AlCoCrFeNi and AlCoCrFeNiTi<sub>0.5</sub> with and without airflow. The CN is a number that related to the frequency of reversing the sliding direction during the wear tests. As shown, the airflow reduced the wear volume loss, implying that the oxide scale formed on the alloys did not benefit the wear resistance of the alloys.



**Fig. 2.10.** Wear loss of (a) AlCoCrFeNi and (b), caused by wear tests with and without the airflow (standard deviation) [29]

### 2.1.3 The mechanical properties of medium-entropy alloys

The medium-entropy alloys also present interesting mechanical and anti-corrosion ability, compared to the high-entropy alloys, with fewer elements and less complexity, which may facilitate microstructure control and reduce costs. There are studies [39-45] conducted to compare the mechanical properties, anti-corrosion properties, or other properties like magnetic properties of high-entropy alloys with those of medium-entropy alloys. Gali et al. [45] investigated and compared the yield strength and fracture strain of a high-entropy alloy CrMnFeCoNi (HE-1) and corresponding medium entropy alloy CoCrFeNi (HE-4) at different temperatures from -196 °C to 1000 °C. Fig. 2.11 depicts changes in tensile strength and yield strength of these two alloys with increasing temperature, showing the strong dependence of the temperature to both the yield and ultimate strength. Fig. 2.12 shows the effect of temperature on the elongation to fracture of both the alloys, showing that the MEA has its properties similar to those of the HEA.



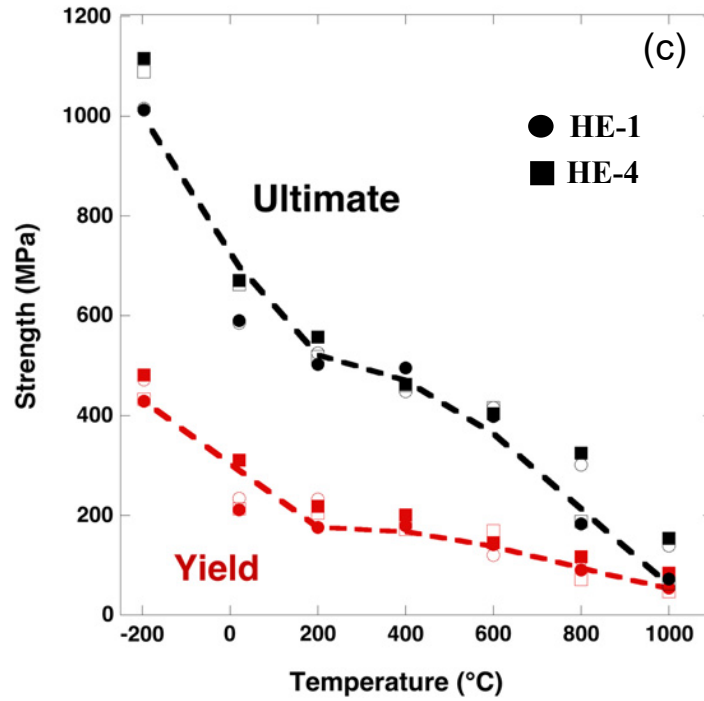


**Fig. 2.11.** Temperature dependencies of the 0.2% offset yield strengths of the CrMnFeCoNi (HE-1) and CrFeCoNi (HE-4) alloys tensile tested at engineering strain rates of  $10^{-3} s^{-1}$  (a), and  $10^{-1} s^{-1}$  (b). Variations in ultimate tensile strength and yield strength for the two alloys are shown in (c) and strain rates investigated in this study. To first order, the small variations between the two alloys and strain rates are ignored, so only one dashed curve is drawn (as a guide to the eye) through each data set [45]

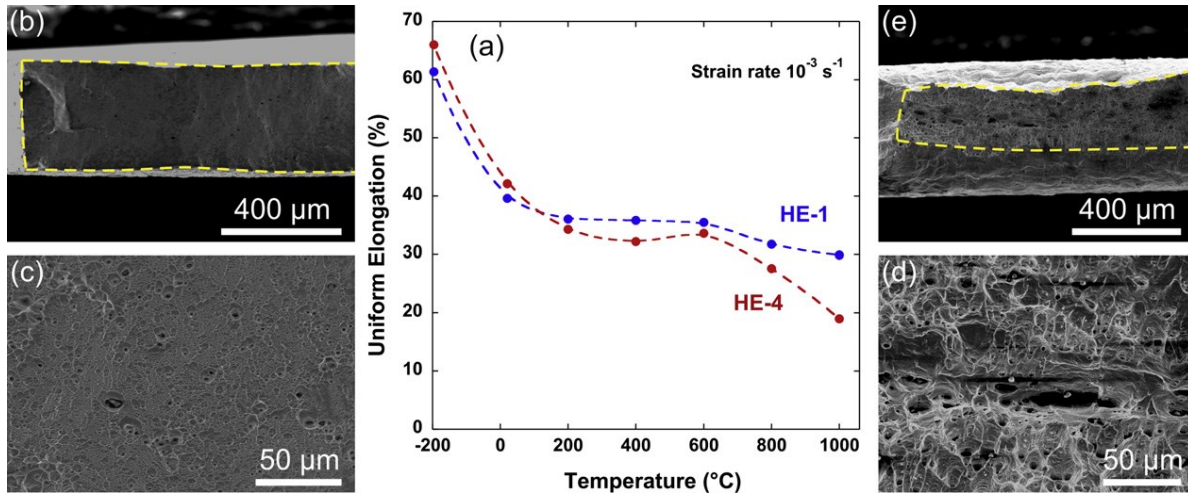


**Fig. 2.12.** (a) Temperature dependence of the tensile ductilities of CrMnFeCoNi (HE-1) and CrFeCoNi (HE-4) tested at an engineering strain rate of  $10^{-3} \text{ s}^{-1}$ . Also shown are fractography of specimens tested at  $-196 \text{ }^\circ\text{C}$  (b, c) and  $400 \text{ }^\circ\text{C}$  (d, e). The dashed outlines of the fracture surfaces show that there is less thickness reduction (necking) at  $-196 \text{ }^\circ\text{C}$  (b) than at  $400 \text{ }^\circ\text{C}$  (e) [45]

Laplanche et al. [46] investigated the tensile properties of a medium-entropy alloy CrCoNi and corresponding high-entropy alloy CrCoFeMnNi at various temperatures in the range of 77K and 293 K, which were rolled with the same process to have similar textures. The study shows that the mechanical properties of this MEA are superior to those of the HEA, as illustrated in Fig. 2.13.

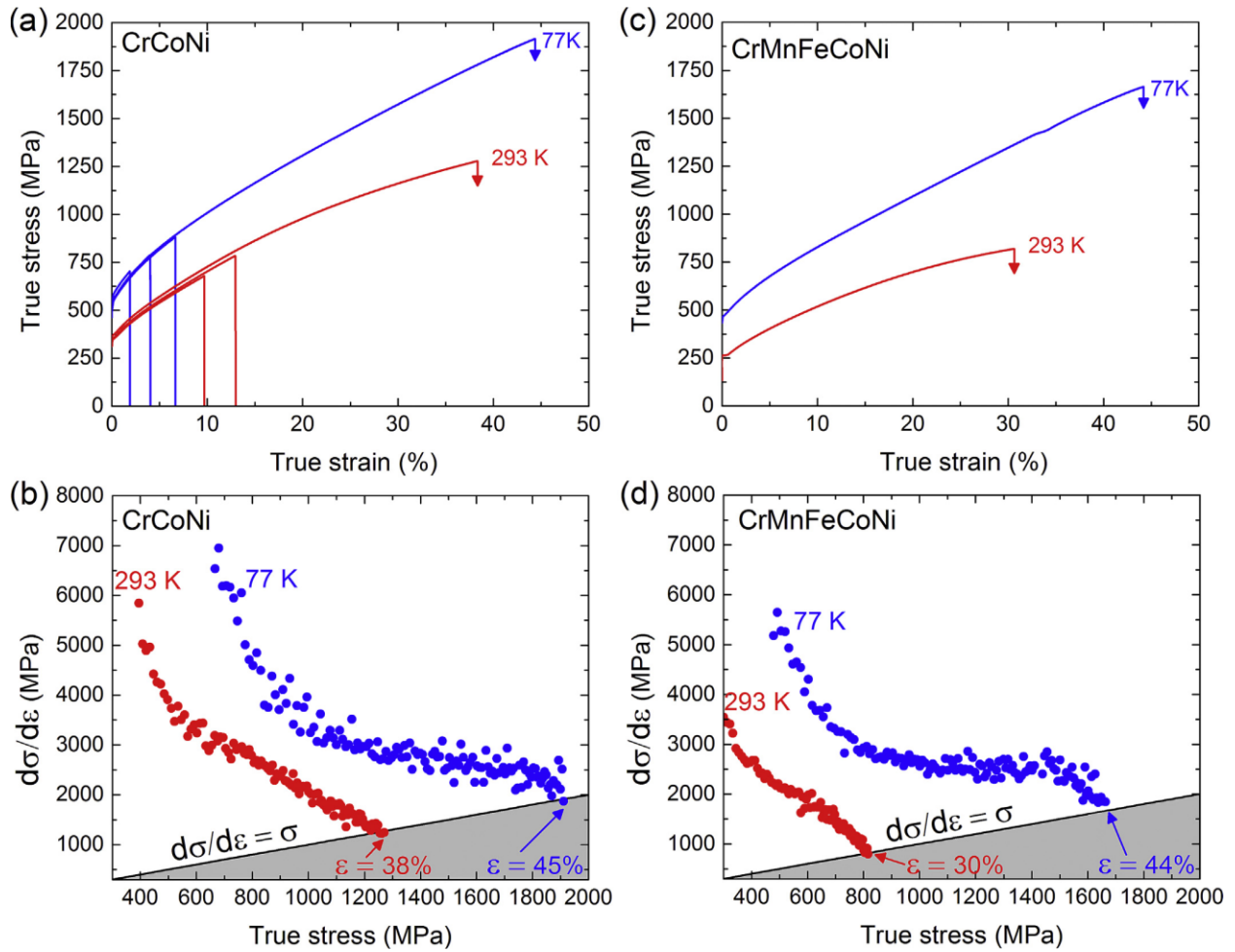


**Fig. 2.13.** True stress-strain curves of tensile tests at 77 K and 293 K of (a) CrCoNi medium-entropy alloy and (c) CrMnFeCoNi high-entropy alloy. Curves with arrows at the end are from specimens tested to fracture while the other curves in (a) are from interrupted tests. Work hardening rate ( $d\sigma/d\varepsilon$ ) versus true stress of (b) CrCoNi and (d) CrMnFeCoNi [46]

With addition of proper elements, the medium-entropy alloys could have an improvement in mechanical properties. Chang et al. [47] observed that an addition of Mo to CoCrNi alloy, the modified alloy of  $(\text{CoCrNi})_{97}\text{Mo}_3$  had an increase in yield strength by 30 % while the original high ductility was. Fig. 2.14 presents the engineering stress-strain curve and fracture elongation

of Mo-0, Mo-1, Mo-3, Mo-5, which had different values of x in the alloy's denotation of  $(\text{CoCrNi})_{100-x}\text{Mo}_x$ .

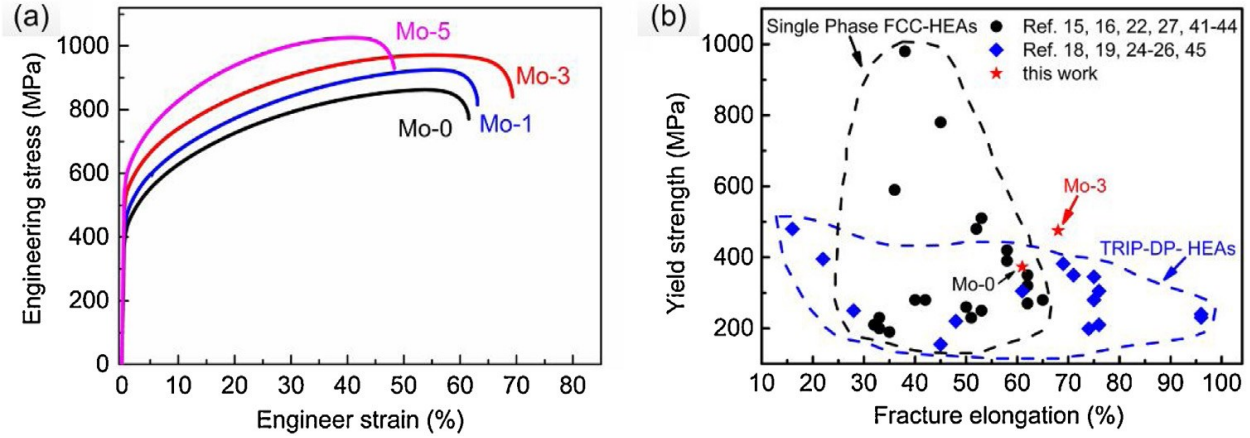


**Fig. 2.14.** (a) Engineering stress-strain curves of the  $(\text{CoCrNi})_{100-x}\text{Mo}_x$  alloys after annealing at  $900^\circ\text{C}$ , and (b) comparison of mechanical properties of Mo-3 alloy with reported single-phase FCC-HEAs and TRIP-DP-HEAs [47]

## 2.2 The corrosion behavior of high-entropy alloys

### 2.2.1 Effect of composition on corrosion resistance of high entropy alloys

Many high-entropy alloys possess the anti-corrosion ability, which makes them a promising candidate for anti-corrosion applications. Passive elements such as Cr, Ti and Al in high-entropy alloys render them corrosion resistant, compared to other HEAs without passive elements. A number of studies on the electrochemical response of high-entropy alloys to corrosive solution environments can be found in the literature [38, 48-54]. Qiu et al. [54]

discovered that the addition of Co can also improve the anti-corrosion ability by forming a passive film the surface. Fig. 2.15 presents potentiodynamic polarization curves of alloys,  $\text{Al}_2\text{CrFeCo}_{0.5}\text{CuNiTi}$  and  $\text{Al}_2\text{CrFeCo}_{1.0}\text{CuNiTi}$ , with different amounts of Co, and corresponding corrosion parameters are given in Table 2.1, including corrosion current ( $I_{\text{corr}}$ ) and corrosion potential ( $E_{\text{corr}}$ ), in comparison with other alloys [37]. The passive films that play an important role in corrosion resistance formed on the HEA surface with the presence of Co, and their resistances to corrosion increase with increasing the Co Content. The corrosion current density of the HEA in this study is lower as shown in Fig 2.15(a).

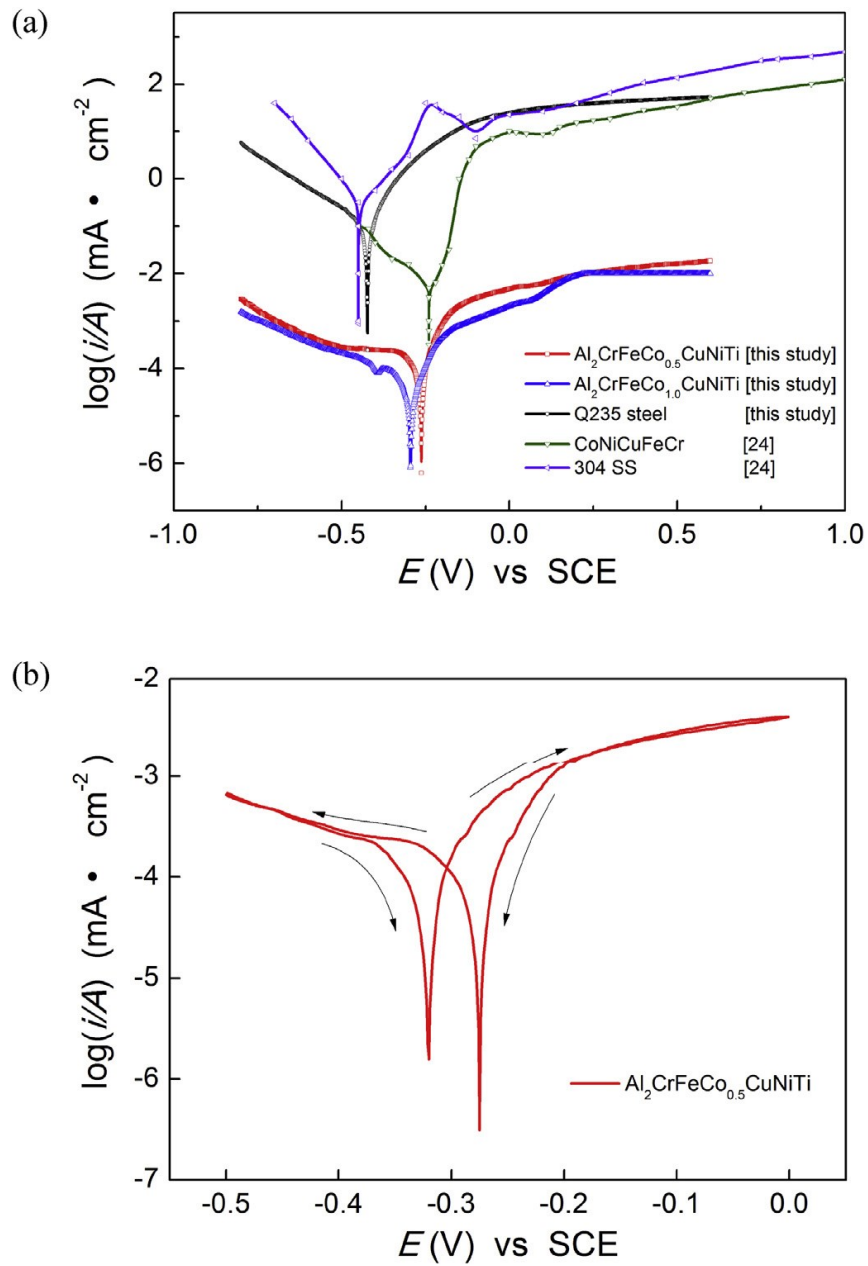


**Fig. 2.15.** Corrosion performance in HCl solutions (a) potentiodynamic polarization curves of high-entropy alloy, 304 SS and Q235 steel (b) cyclic polarization curve of  $\text{Al}_2\text{CrFeCo}_{0.5}\text{CuNiTi}$  high-entropy alloy coating [37]

**Table 2.1** Corrosion parameters of HEAs, 304 SS and Q235 steel in HCl solutions [37]

Samples	Concentration	$I_{\text{corr}}/\text{mA}\cdot\text{cm}^2$	$E_{\text{corr}}/\text{V}$
$\text{Al}_2\text{CrFeCo}_{0.5}\text{CuNiTi}$	0.5 mol/L	$3.9\times 10^{-4}$	-0.25
$\text{Al}_2\text{CrFeCo}_{1.0}\text{CuNiTi}$	0.5 mol/L	$3.3\times 10^{-4}$	-0.30
Q235 Steel	0.5 mol/L	$2.1\times 10^{-1}$	-0.41
304 SS	1.0 mol/L	$7.3\times 10^{-1}$	-0.45
CoCrCuFeNi	1.0 mol/L	$9.0\times 10^{-3}$	-0.24
$(\text{CoCrCuFeNi})_{95}\text{B}_5$	1.0 mol/L	$1.4\times 10^{-2}$	-0.22
CoCrCuFeNiNb	1.0 mol/L	$1.0\times 10^{-2}$	-0.31

Not only the passive elements, changes in content of other elements also affect the anti-corrosion ability of the HEAs, Fan et al. [38] investigated the effect of Fe content on corrosion behavior of AlCoCrFeNi, including iron concentrations of 42.5 at.%, 44.9 at.%, 47.5 at.%, 50.4 at.%. The increase in the Fe content changes the structure from BCC to BCC+FCC. The dual phase structure deteriorates the corrosion properties of the alloy. Fig. 2.16 depicts the corrosion performances of the HEA with altered Fe contents in comparison with that of commercial 304 stainless steel, including open circuit diagram, potentiodynamic polarization, and Nyquist plot. The increase of the content of Fe in AlCoCrFeNi stabilizes the FCC phase by increasing the VEC, thus decreasing corrosion resistance as illustrated in the Nyquist plot which shows that the

Fe-0 and Fe-0.25 that only contain the BCC phase have the highest impedance than other materials. Fig. 2.17 presents the XRD patterns of the HEAs with different Fe content to show the changes in phase structure.

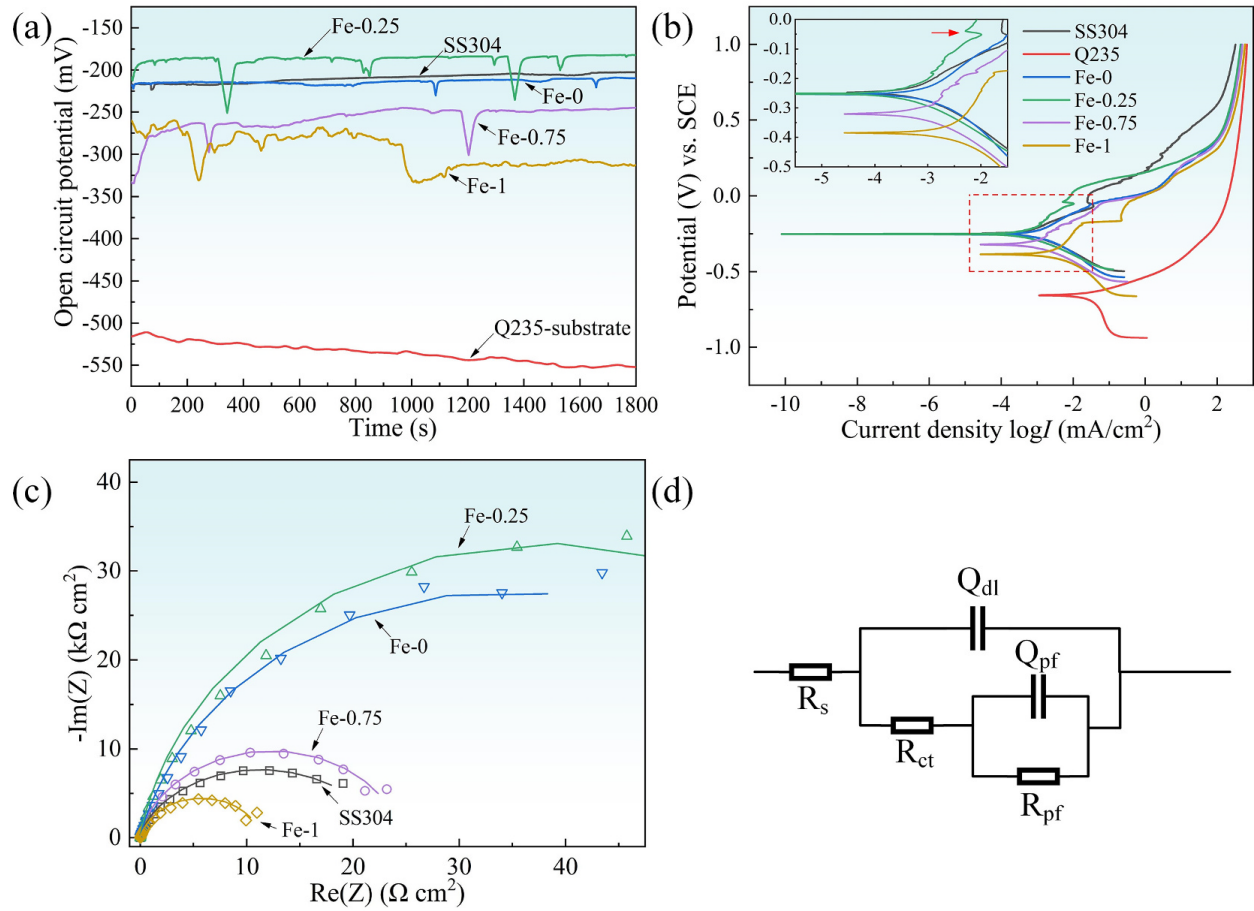


**Fig. 2.16.** Corrosion performance of GTA cladded AlCoCrFeNi HEA coatings. (a) Open circuit potential; (b) Potentiodynamic polarization; (c) Nyquist plot; (d) Equivalent circuit [38]

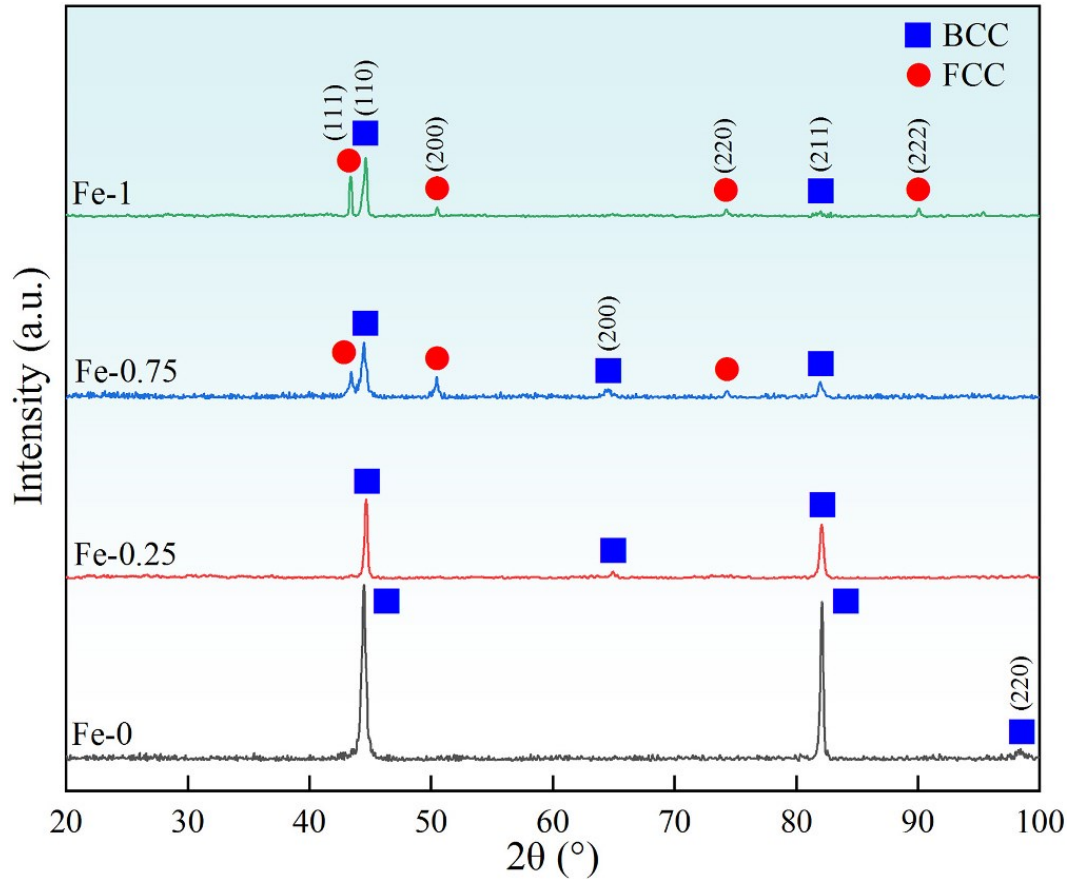


*Fig. 2.17. XRD result of each of different Fe content AlCoCrFeNi. [38]*

## 2.2.2 The resistance of high-entropy alloys to corrosive wear

In many industrial processes, wear and corrosion occur simultaneously. In this case, the tribological behavior and anti-corrosion ability of materials cannot be separated when dealing with the degradation of the materials, since the wear and corrosion can assist each other, leading to more damage to the target material. Studies on corrosive wear of high-entropy alloys can be found in the literature [55-68]. For instance, Wu et al. [69] investigated the effect of Ti on corrosive wear of AlCoCrFeNi HEA in NaCl and HCl solutions, respectively, and showed that

AlCoCrFeNiTi<sub>0.5</sub> exhibited higher hardness contributed by solid-solution hardening and precipitation-hardening as shown in in Table 2.2. The high-entropy alloy also exhibited higher corrosion resistance, compared to the commercial 316SS. The corrosion current of the AlCoCrFeNiTi<sub>0.5</sub> is smaller than that of 316SS, determined from potentiodynamic polarization tests depicted in Fig. 2.18. In the corrosion wear test, the addition of Ti enhances the resistance of the alloy to corrosion wear due to the effects of Ti on increased hardness and improved corrosion resistance, which effectively suppressed corrosive wear. Fig. 2.19 presents SEM images of HEAs and 316SS after corrosion wear tests in NaCl solution and HCl solution, respectively. Table 2.3 shows the wear rate of HEAs and 316SS in both corrosive solutions, indicating the benefits of the addition of Ti to the AlCoCrFeNi alloy.

**Table 2.2.** Mechanical properties of the materials measured with nano-indentation under the maximum load of 100 mN. [69]

Alloys		Hardness HIT (GPa)	Elastic Modulus EIT (GPa)	Creep CIT (%)
AlCoCrFeNi		6.35 ± 0.11	206.9 ± 9.4	2.01 ± 0.09
AlCoCrFeNiTi <sub>0.5</sub>	Dendrite	8.39 ± 0.07	203.5 ± 8.1	1.69 ± 0.08
	Interdendrite	9.52 ± 0.25	201.4 ± 6.9	1.49 ± 0.05
316SS		2.74 ± 0.06	101.6 ± 5.6	2.93 ± 0.14

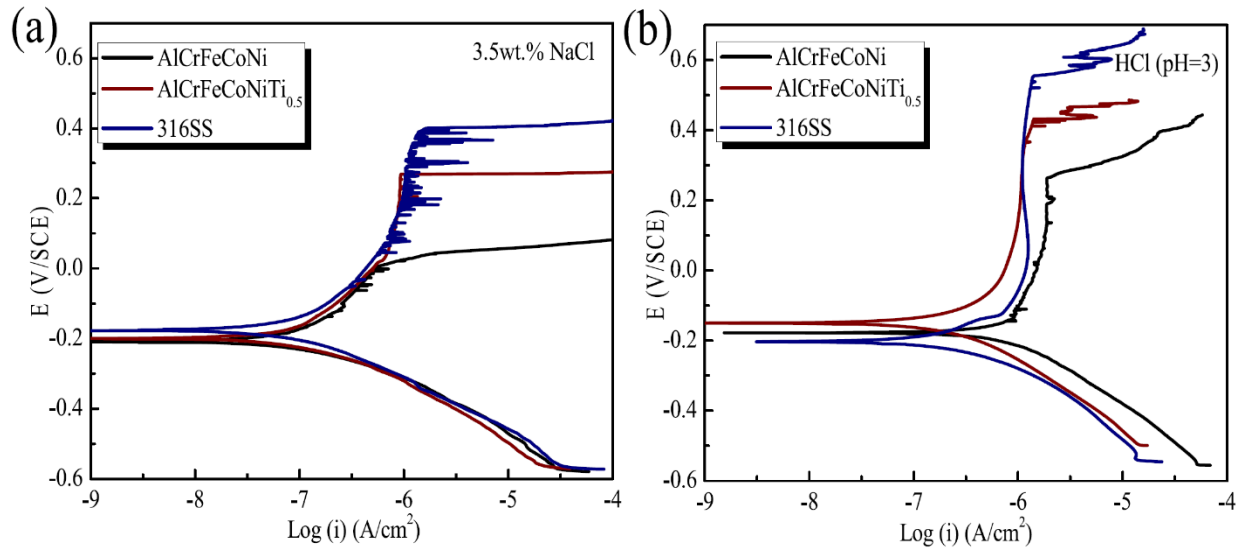


**Fig. 2.18.** Potentiodynamic polarization curves of AlCoCrFeNi, AlCrFeCoNiTi<sub>0.5</sub> and 316SS in (a) 3.5 wt.% NaCl and (b) HCl (pH = 3) solutions. [69]

**Table 2.3.** Specific wear rates of AlCoCrFeNi, AlCrFeCoNiTi<sub>0.5</sub> and 316SS alloys in 3.5 wt. % NaCl and HCl (pH = 3) solutions. Counterpart: 6 mm diameter Si<sub>3</sub>N<sub>4</sub> ball. [69]

Alloys	Specific wear rate (mm <sup>3</sup> /Nm)	
	3.5 wt % NaCl	HCl (pH = 3)
AlCoCrFeNi	$5.21 \times 10^{-5}$	$6.77 \times 10^{-5}$
AlCoCrFeNiTi <sub>0.5</sub>	$2.19 \times 10^{-5}$	$2.29 \times 10^{-5}$
316SS	$1.63 \times 10^{-4}$	$2.04 \times 10^{-4}$

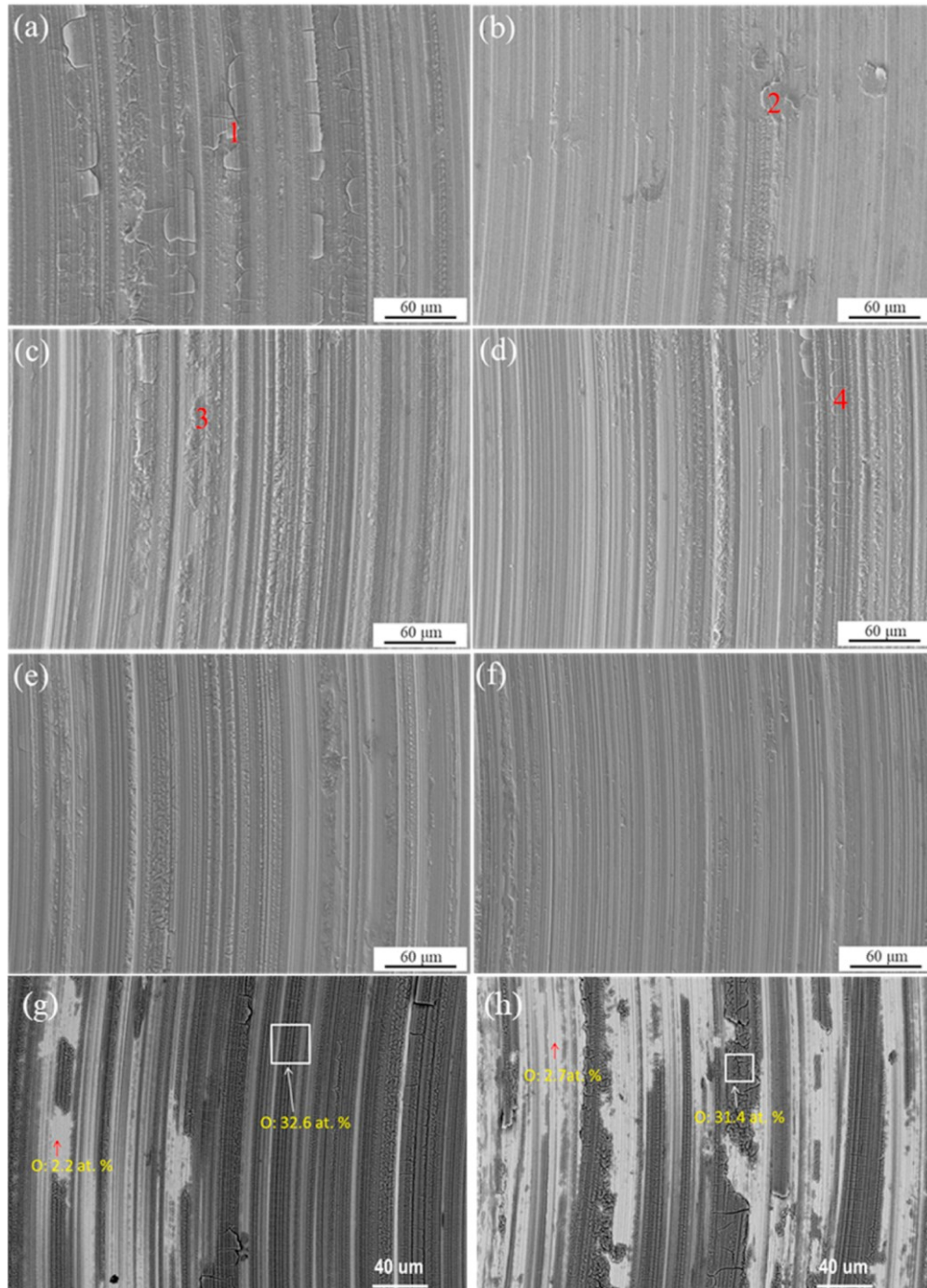
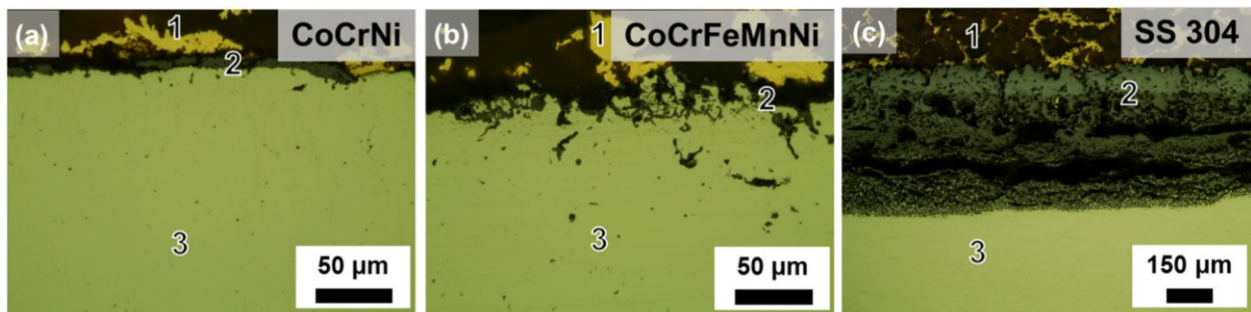


**Fig. 2.19.** SEM images of worn surface at the sliding distance of 36 m in (left) 3.5 wt.% NaCl solution and (right) HCl (pH = 3) solution: (a) and (b) AlCoCrFeNi; (c) and (d) AlCrFeCoNiTi0.5; (e) and (f) 316SS; BSD images of worn surfaces of (g) AlCoCrFeNi and (h) AlCrFeCoNiTi0.5 worn in 3.5 wt.% NaCl solution. [69]

### 2.2.3 The resistance of medium-entropy alloys to corrosive wear

Although high-entropy alloys have drawn much more attention than medium-entropy alloys with superior properties, the medium-entropy alloys have proven their value by researchers [71-78]. Agustianingrum et al. [70] studied the corrosion behavior of CoCrNi medium-entropy alloys in comparison with CoCrFeMnNi HEA and 304SS, showing that the former exhibits better performances in resisting oxidation with lesser oxidation, depicted in Fig. 2.20. In Zhu et al. research [71], potentiodynamic polarization curves and the corrosion rates of CoCrNi and 316 L SS are shown in Fig. 2.21 and Fig. 2.22, respectively. Their study showed that CoCrNi MEA exhibits higher corrosion resistance due to its dense and more protective passive film.



1: Copper mounting 2: Oxide layer 3: Base metal

*Fig. 2.20 OM images of (a) CoCrNi, (b) CoCrFeMnNi, and (c) SS 304 from cross-sectional areas after oxidation at 1100 °C for 24 h. [70]*

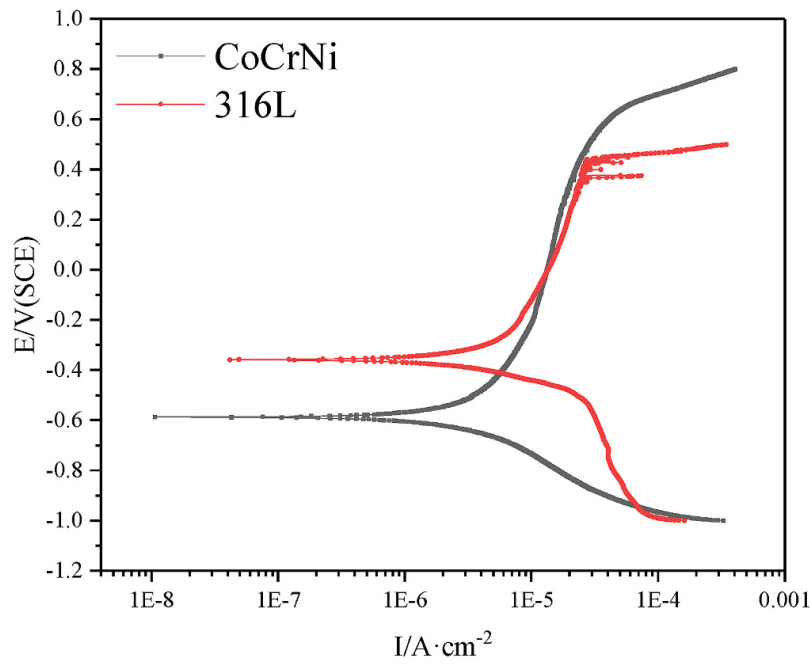


**Fig. 2.21** Potentiodynamic polarization curves of CoCrNi MEA and 316 L SS. [71]

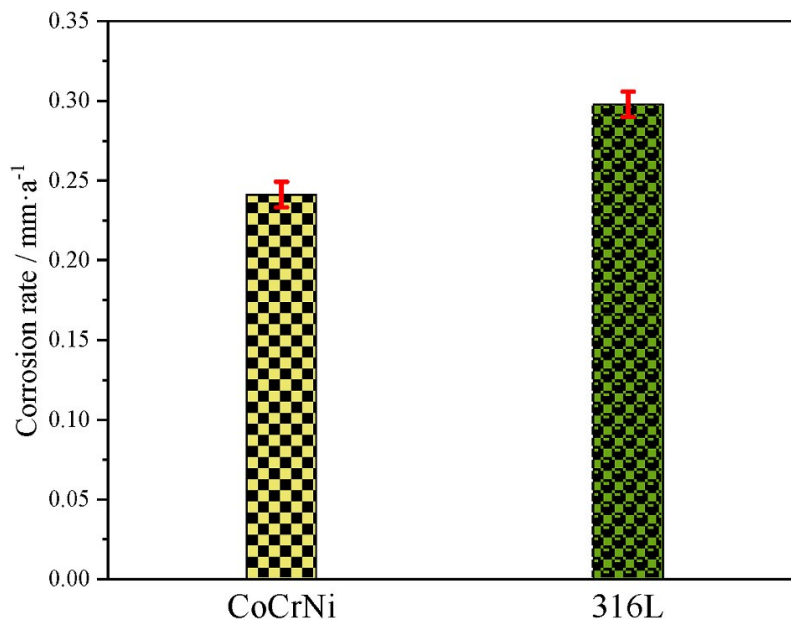


**Fig. 2.22** Corrosion rates of CoCrNi MEA and 316 L after immersion test in 3.5 wt% NaCl solution. [71]

Hu et al. [79] investigated TiZrNb MEA with different concentrations of elements (TiZrNb, Ti40Zr40Nb20, Ti45Zr35Nb20, Ti45Zr45Nb10, and Ti50Zr40Nb10) and compared them with well-known biomaterials Ti4Al4V. The TiZrNb MEAs showed better strength, e.g., the elastic modulus of TiZrNb range of 52 GPa ~ 73 GPa, which is close to that of the human bone and their corrosion resistance is similar to that of Ti6Al4V. The TiZrNb also showed higher yield strength than Ti4Al4V. Fig. 2.23 and 2.24 illustrate the tensile strength and potentiodynamic curves of the alloys.

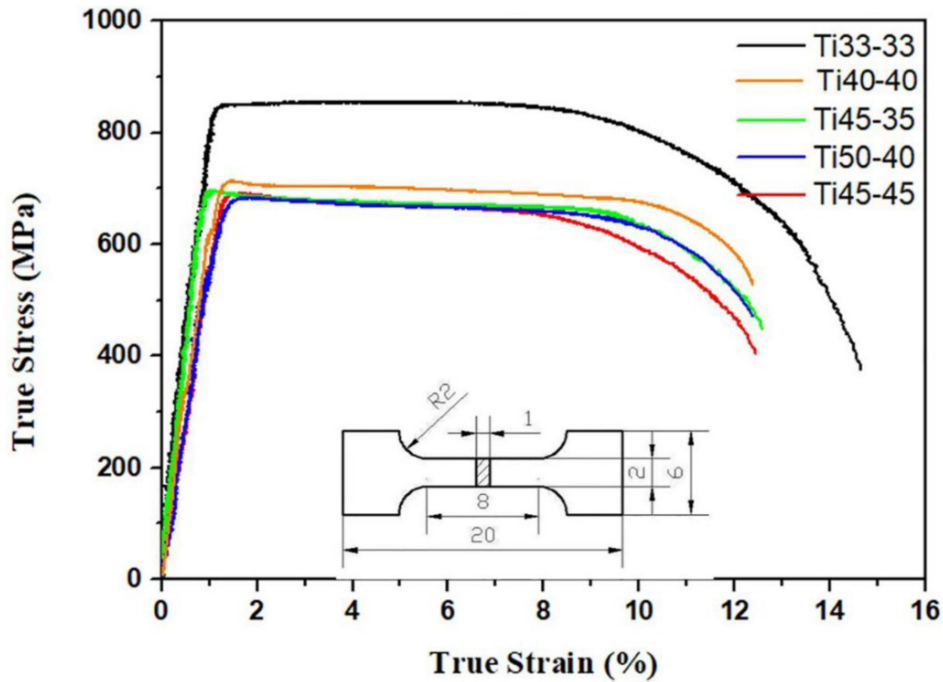


**Fig. 2.23** True tensile stress-strain of Ti–Zr–Nb MEAs at room temperature, and the inset at bottom left is the schematic diagram and size of the tensile specimen, the inset at bottom right is the EBSD of Ti33-33 near the fracture [80].

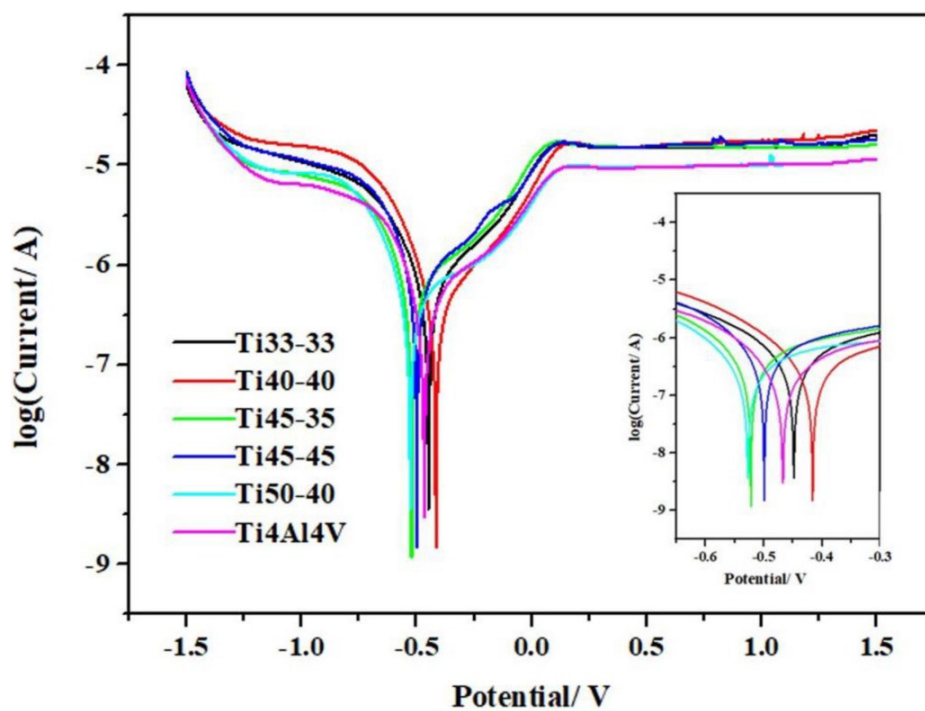


**Fig. 2.24** Potentiodynamic curves of Ti–Zr–Nb MEAs and Ti6Al4V alloy in the PBS solution at  $37 \pm 0.5$  °C. The inset is the enlarged part of the curves from -0.65 V to -0.3 V [80].

## **Chapter 3: Effect of Ni in Mechanical Properties and Microstructure of medium-entropy alloys AlCoCrFe and high-entropy alloys AlCoCrFeNi<sub>x</sub> (x > 0)**

As mentioned at the beginning of the thesis, AlCoCrFeNi has drawn considerable attention due to its attractive mechanical properties. This alloy has often been used as a base alloy for developing new HEAs by alloying with additional elements or modifying the ratio of its element concentrations for improved properties. On the other hand, medium-entropy alloys with fewer elements can also have superior performance with less complication. In this study, we investigated the microstructures and properties of as-cast AlCoCrFeNi<sub>x</sub> alloys (x = 0 - 2), focusing on effects of Ni content on microstructure and the corresponding mechanical properties and resistance to wear, corrosion, and corrosive wear. In particular, the Ni-free four-element medium-entropy alloy, AlCoCrFe, was also examined and compared with its five-element high-entropy companion.

Ni is an element with a high electron work function, which helps strengthen metallic bonds [11-13]. The beneficial effect of Ni on the mechanical strength of alloys, e.g., Cu alloys and low carbon steel, has been well demonstrated [12, 13]. In general, Ni is an effective element to select for the solid-solution hardening. It also helps increase the anti-corrosion ability of iron-nickel alloys [14] due to the fact that it increases the atomic bonding energy and thus the bond's stability. However, if Ni reacts with some elements to form intermetallic phases or weaker phases, the influence of Ni on the strength of alloys could become negative [13, 81]. Therefore, the role that Ni plays in affecting mechanical and wear properties of AlCoCrFeNi is worth being studied further in order to effectively tailor HEAs, not only AlCoCrFeNi but also other HEAs.

In addition to Ni, effects of other elements additions like Si, TiC, Ti and Co have also been studied [82-85], showing positive influences on physical properties of AlCoCrFeNi-based alloys. Pi *et al.* [86] observed that by increasing the nickel content in AlCoCrFeNi<sub>x</sub> from x = 0.6 to 1.4, the hardness decreased. Voiculescu *et al.* [87] also observed a decrease in the hardness of AlCoCrFeNi<sub>x</sub> as the nickel content increased from x=1 to 2. Tian *et al.* [81] investigated the effects of Ni content on the phase formation, tensile properties, and deformation of Ni-rich AlCoCrFeNi<sub>x</sub> (x = 2, 3, 4) and noticed that increasing Ni content facilitated the formation of FCC/L12 phases and also caused the microstructure evolved from near-eutectic structure to the divorced eutectic structure, leading to excellent plasticity with a moderate strength. The compressive yield strength of the AlCoCrFeNi<sub>x</sub> (1.0 ≤ x ≤ 3.0) high-entropy alloys was investigated by Cao *et al.* [88] who showed an overall decreasing trend, dropping from 1360 MPa (x = 1.5) to 450 MPa (x = 3.0). Alloys with a high Ni content (x ≥ 2.4 at.%) had a higher plastic strain (> 40%) than those of Ni-1.0 and Ni-1.5 alloys (<25%). Although some interesting aspects of AlCoCrFeNi<sub>x</sub> were studied, it is unclear if the performance of this high-entropy alloy is superior or comparable to its medium-entropy companion, AlCoCrFe. More detailed characterization of microstructures and microstructural evolution in the alloy with respect to the Ni addition would help use the material effectively.

As mentioned earlier, the medium-entropy alloy with fewer elements may also possess attractive properties and their microstructures could be relatively easier to control. The difference in properties between some medium-entropy alloys and high-entropy alloys, e.g., medium-entropy ferrous alloys and CoCrFeMnNi alloys, has been studied [42, 44]. Since the existence of second phases is common for high-entropy alloys [94-96] their properties become less easy for prediction, which certainly depend on their microstructure features. In this chapter, we will

investigate the microstructure, mechanical properties, and wear resistance of the MEA AlCoCrFe and HEA AlCoCrFeNi<sub>x</sub> ( $x > 0$ ). Results of the study are reported in this chapter.

## **3.1 Experiment procedure**

### **3.1.1 Samples preparation**

Samples of AlCoCrFeNi<sub>x</sub> ( $x = 0, 0.5, 1.0, 1.5$  and  $2.0$ ) were prepared using a vacuum arc furnace by melting mixtures of element powders. Each of the mixtures was pelleted into a cylinder using a presser to make a cylindrical sample weighted 10g, which was then placed in the arc furnace and melted three times in a high purity argon gas atmosphere that was used to protect the sample from oxidation. The obtained samples were cut into small pieces with dimensions of  $1 \times 1 \times 0.5$  cm by a wire electrical discharge machine (WEDM or Wire EDM). After cutting, the samples were polished with sandpaper from grit 80, 180, 400, 800, to 1200. The samples were finally polished with  $1 \mu\text{m}$  alumina powder and washed in an ultrasound cleaning machine with water to remove powder residue on the surface, followed by drying using a pressed airflow. The prepared samples were used for microstructure characterization and property evaluation.

### **3.1.2 Microstructure characterization**

A scanning electron microscope (SEM, Zeiss EVO M10, and Zeiss Sigma FESEM) with energy dispersive X-ray analysis (EDX) was used to observe the surface morphology and

analyze the composition of each sample. A transmission electron microscope, JEOL JEM-ARM 200CF S/TEM with EDX detector operated at 200 kV, was used to determine the crystal structure and chemical compositions of phases in the alloys. The general morphology of the phases was observed and high-resolution atomic images of the phases were obtained in the TEM mode, while the chemical compositions of the phases were analyzed in the scanning transmission microscope (STEM) mode. The TEM samples were prepared by slicing the cast materials, then grinding both sides of each sample to a thickness of 100  $\mu\text{m}$  or less, followed by electro-polishing. It should be pointed out that, since the medium-entropy AlCoCrFe alloy was less tough, a dedicated procedure was developed before the sample was ground and electro-polished. Unlike cutting a large piece of sheet, the cylindrical sample with a diameter of 3 mm was cut from a large sample, it was then sliced into circular pieces with a thickness of about 400-500  $\mu\text{m}$ . Both sides of the circular pieces were ground, followed by electro-polishing.

### **3.1.3 Evaluation of physical properties**

Macro-hardness of the alloys was tested by Rockwell's scale HRA under a load of 60 kgf, and the micro-hardness of the alloys was measured under loads of 80 mN and 300mN, respectively, using a NHT<sup>3</sup> nanoindentation tester (Anton Paar, Canada). At least three indentation tests were performed for each sample and each type of domains in order to obtain an average value. The reason the hardness of each sample was tested separately on a macro and a micro scale is that second phases occurred in AlCoCrFeNi<sub>1.5</sub> and AlCoCrFeNi<sub>2.0</sub>.

Compression tests were performed for the alloys under study. Compressive stress-strain curves of AlCoCrFeNi<sub>x</sub> alloys with different Ni contents were obtained at a strain rate of 0.3

mm/min using a 313 Electromechanical Universal Test Machine (TESTRESOURCES, USA). The alloy samples for the compression tests had a rectangular cross-section of 4 by 4 mm<sup>2</sup> and 7 mm in height. The compressive force was applied along the longitudinal axle of the sample.

Wear performances of the AlCoCrFeNi<sub>x</sub> alloys in dry wear condition were evaluated using a pin-on-disc tribometer (CSEM Instruments). The counterpart for the wear test was a silicon nitride (Si<sub>3</sub>N<sub>4</sub>) ball with a diameter of 4mm. Each wear test was performed under an applied load of 5N at a sliding speed of 200 rpm (equal to 2.1 cm/s) for 30 minutes. The dry wear tests were performed under two conditions: one was performed in the ambient condition and the other was performed with an airflow to cool the sample surface in order to minimize oxidation caused by frictional heat. After the wear test, the wear track was analyzed using a Zygo, 3D optical profilometer to measure the volume loss.

## **3.2 Result and discussion**

### **3.2.1 Microstructure of AlCoCrFeNi<sub>x</sub> (x = 0 and x > 0) by SEM and TEM**

Microstructures of the medium-entropy alloy, AlCoCrFe, and high-entropy alloy AlCoCrFeNi<sub>x</sub> (x = 0.5, 1.0, 1.5 and 2.0), were analyzed using scanning electron microscope. SEM images of the samples are presented in Fig. 3.1. Corresponding average compositions and those of individual phases or domains determined with EDX are given in Table 3.1. As shown, the Ni-free medium-entropy alloy, AlCoCrFe, appears to be homogeneous, while two phases or domains (dark and light) show up and become more distinctive with increasing the Ni content. A

similar two-phase heterogeneous microstructure was shown in early studies, such as a study by Joseph et al. [30] on  $Al_xCoCrFeNi$  with different Al contents. The bright domain is Fe-Cr-rich while the dark domain is Ni-Al-rich, and their compositions change with the nominal composition.

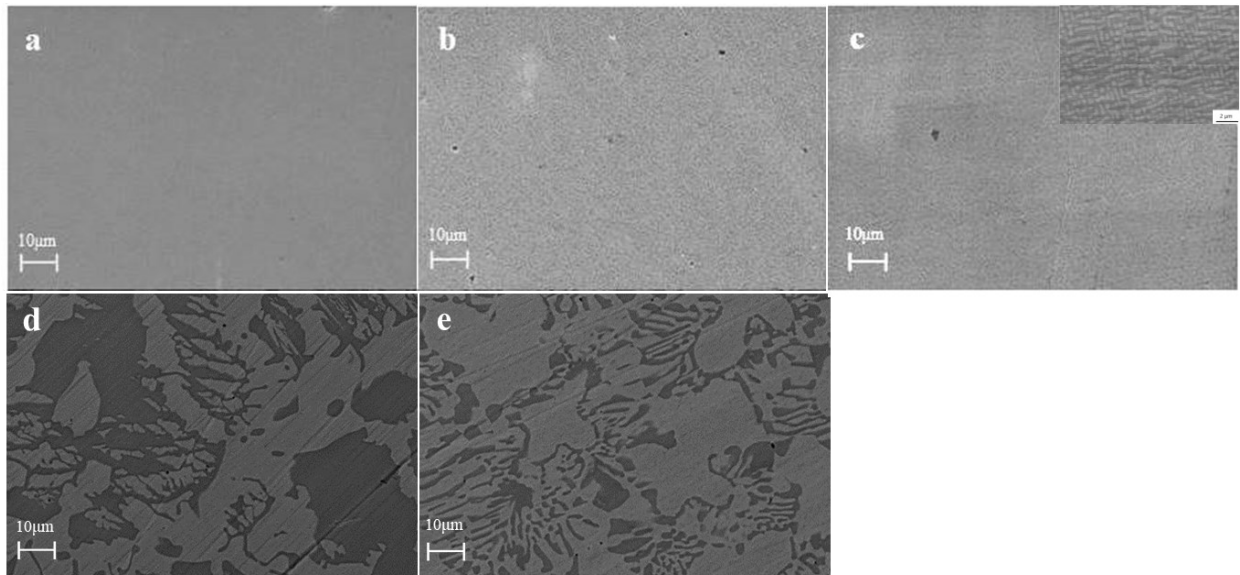


**Fig. 3.1.** SEM images of (a)  $AlCoCrFe$ , (b)  $AlCoCrFeNi_{0.5}$ , (c)  $AlCoCrFeNi_{1.0}$ , (d)  $AlCoCrFeNi_{1.5}$ , (e)  $AlCoCrFeNi_{2.0}$ . A closer image of  $AlCoCrFeNi_{1.0}$  with larger magnification is inserted in (c).

**Table 3.1.** – Overall and local chemical compositions (at%) of AlCoCrFeNi<sub>1.5</sub> and AlCoCrFeNi<sub>2.0</sub> determined by EDX.

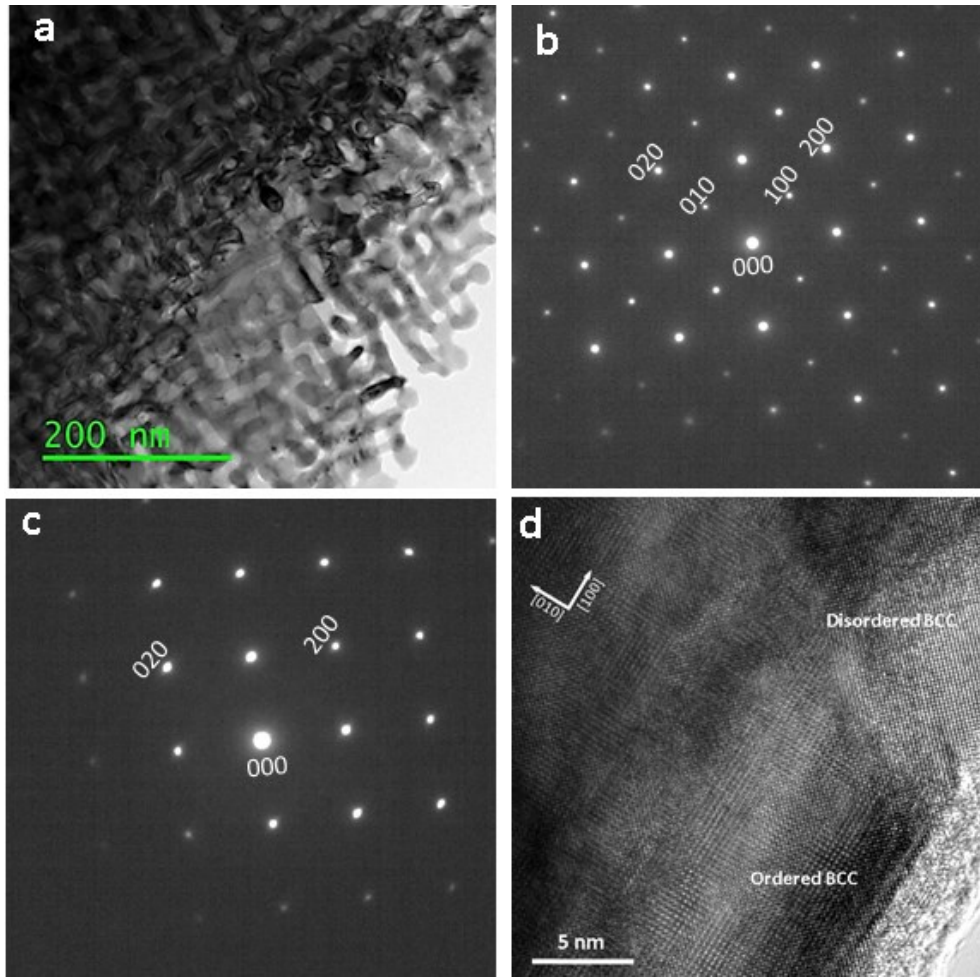
Samples	Atomic percentage (%)				
	Al	Co	Cr	Fe	Ni
AlCoCrFe	25	24.5	25.7	24.8	0
AlCoCrFeNi <sub>0.5</sub>	21.8	21.8	22.7	22.5	11.2
AlCoCrFeNi <sub>1.0</sub>	20.2	19.5	21	19.9	19.4
AlCoCrFeNi <sub>1.5</sub>	16.7	19.1	16.5	18.0	29.7
AlCoCrFeNi <sub>2.0</sub>	16.1	16.5	16.8	16.8	33.8
AlCoCrFeNi <sub>1.5</sub> (bright phase)	12.7	19.2	22.1	20.8	25.2
AlCoCrFeNi <sub>1.5</sub> (dark phase)	21.6	17.2	17.6	17.4	26.2
AlCoCrFeNi <sub>2.0</sub> (bright phase)	14.3	18.2	17.9	18.9	30.7
AlCoCrFeNi <sub>2.0</sub> (dark phase)	31.3	12.1	9.4	10.5	36.7

For more detailed information on the domains and their evolution, transmission electron microscopy (TEM), scanning transmission electron microscopy (STEM), and EDX mapping were employed for further analysis. Fig. 3.2 illustrates a TEM image of AlCoCrFe medium-entropy alloy, corresponding electron diffraction patterns, and a high-resolution atomic image. Fig. 3.3 illustrates EDX elemental maps showing distributions of Al, Cr, Fe, and Co. As one may see, this alloy shows a spinodal-decomposed nanostructure consisting of two domains, which are Cr-Fe-rich (bright domain) and Al-Co-rich (dark domain), respectively. By viewing the domains using diffraction spots from the diffraction patterns, it is confirmed that the Al-Co-rich domain is an ordered BCC phase and the Cr-Fe-rich one is a disordered BCC phase. The ordered and disordered BCC structures are determined by the structure factor, expressed as [102]

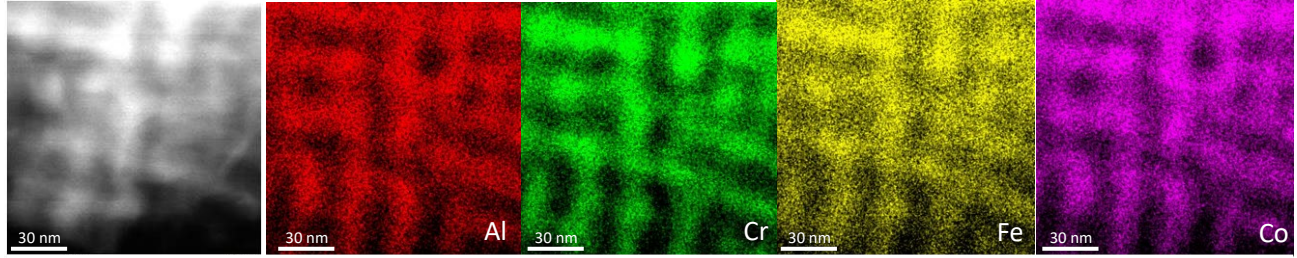
$$F_{hkl} = \sum_i f_i e^{2\pi i(hx_i + ky_i + lz_i)}$$

This factor gives the information about the atomic arrangement. For a disordered binary BCC structure, reflections are present (i.e.,  $F=f_a + f_b$ ) when  $h+k+l$  is even or absent ( $F=f_a - f_b$ ) when  $h+k+l$  is odd (forbidden reflections). However, for an ordered binary BCC, the intensities of forbidden reflections are non-zero and still show up, since  $f_a$  is not equal to  $f_b$ . This helps distinguish the ordered and disordered BCC phases in our high-entropy alloys.

When Ni was added to the AlCoCrFe, the spinodal decomposition was enhanced and the two phases became coarser, e.g., see the SEM image inserted in Fig. 3.1 (c). Fig. 3.4A shows a TEM image of AlCoCrFeNi<sub>1.0</sub>, and Fig. 3.4B is a STEM dark-filed image. From the images, one may see the two type domains larger than those in AlCoCrFe (Fig. 3.2a). Most of the domains are a few hundred nanometers in size and some domains show their size in the range of micron. Unlike the AlCoCrFe shown in Fig. 3.2 and Fig. 3.3, the domain boundaries in AlCoCrFeNi<sub>1.0</sub> can be clearly seen. One of the two type domains is the ordered BCC phase, and the other is the disordered BCC phase. The EDX elemental maps indicate that the bright phase (disordered BCC) in the STEM dark-filed image is Cr-Fe-rich and the dark one (ordered BCC, known as B2) is Al-Ni-rich. In this five-element high-entropy alloy, Ni seems to have a higher affinity for Al, leading to the formation of Al-Ni-rich domain or phase while pushing Co into the Cr-Fe-rich domain.

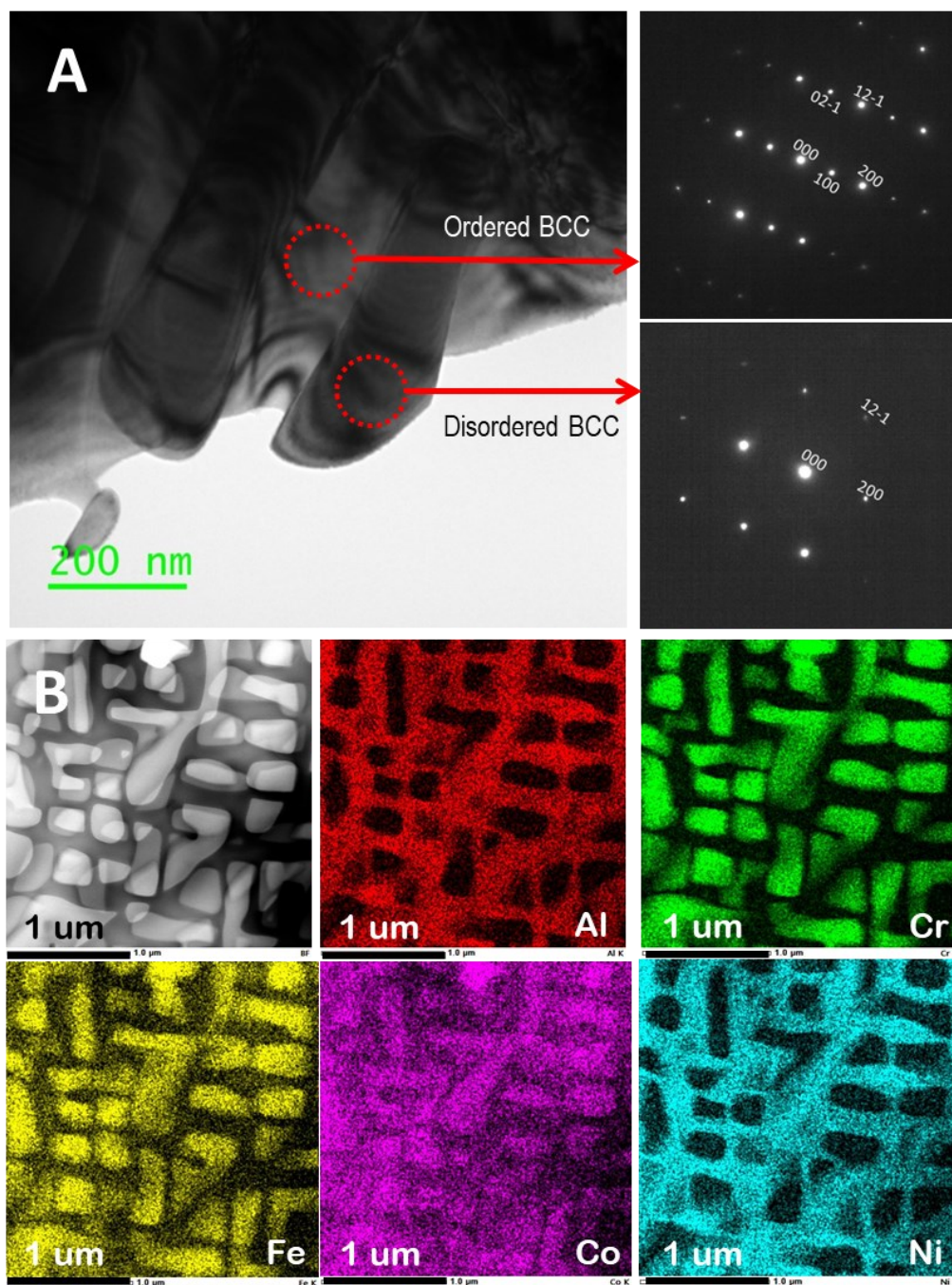


**Fig. 3.2** (a) TEM bright field images showing morphologies of AlCoCrFe sample; electron diffraction patterns of (b) an ordered BCC phase and (c) a disordered BCC phase; (d) a high-resolution atomic image showing the two phases.



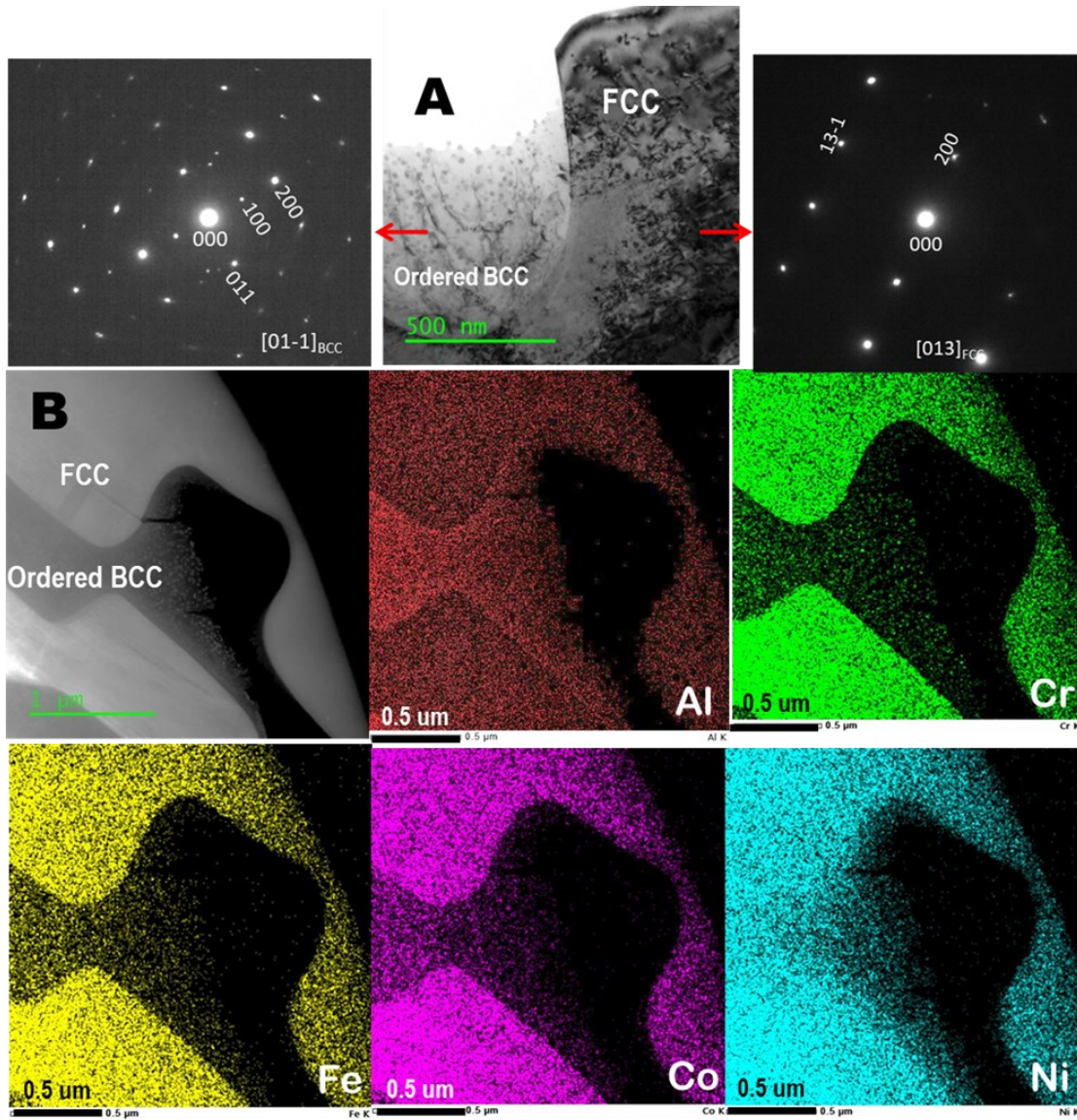
**Fig. 3.3** EDX elemental maps showing the distribution of Al, Cr, Fe, and Co in AlCoCrFe medium-entropy alloy. As shown, there are two domains, one is Cr-Fe-rich (bright domain) and the other is Al-Co-rich (dark domain)

As the Ni content was continuously increased, it was observed that the disordered BCC phase transformed to a FCC phase. Fig. 3.5A shows a TEM image with high magnification. There are two distinctive domains, one of which is the ordered BCC phase, and the other is a FCC phase, confirmed by corresponding electron diffraction patterns. Compared with the phase scale in AlCoCrFe and AlCoCrFeNi<sub>1.0</sub>, one may see that the phases in AlCoCrFeNi<sub>2.0</sub> are in micrometer or micron. Further analysis with STEM and EDX mapping shows that the ordered BCC is Al-Ni-rich while the FCC is Cr-Fe-Co-rich but still contains a fair amount of Ni, as the EDX maps of element distributions indicate in Fig. 3.5B.



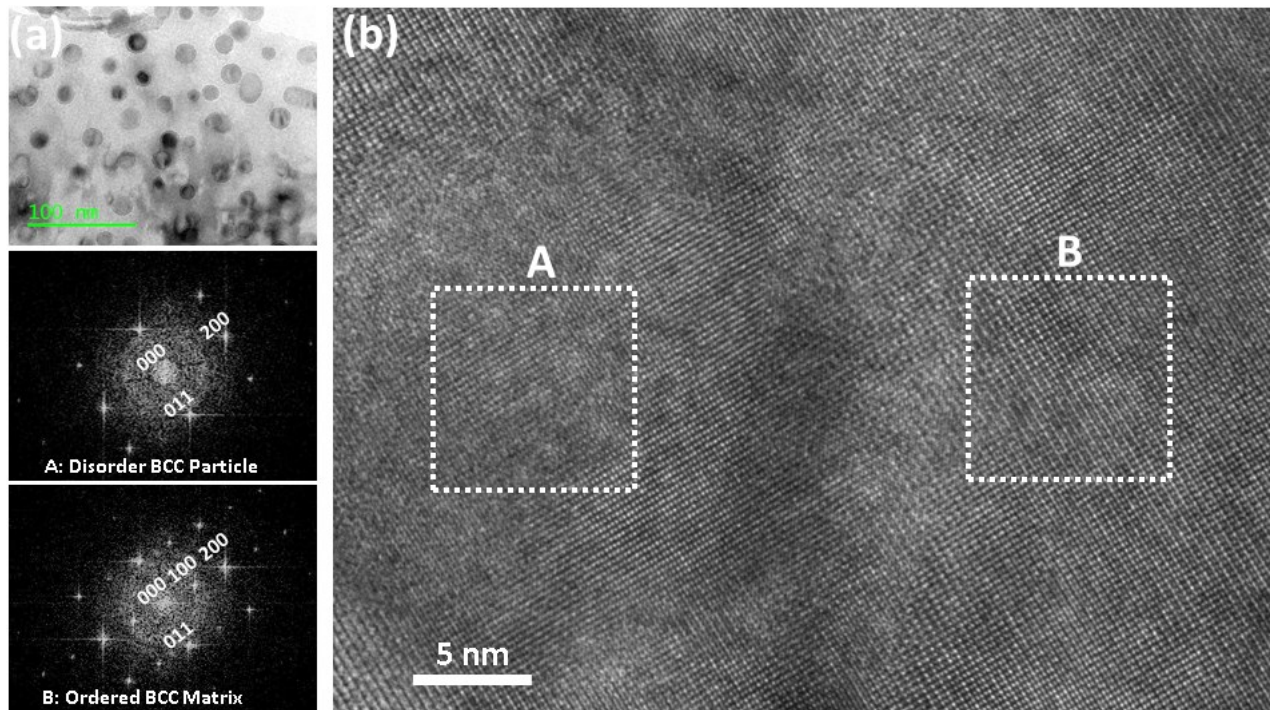
**Fig. 3.4 A** - a TEM image of  $\text{AlCoCrFeNi}_{1.0}$ , and diffraction patterns of two phases in the alloy.

**B** -EDX elemental maps showing the distribution of Al, Cr, Fe, Co, and Ni.



**Fig. 3.5 A** - a TEM image of  $\text{AlCoCrFeNi}_{2.0}$ , which contains two distinctive type domains, one of which is an ordered BCC phase and the other is a FCC phase; inside the ordered BCC phase, there are nanoparticles; **B** – EDX maps of element distributions in the ordered BCC and FCC phases.

It is of interest to observe that inside the ordered BCC phase, there are nanoparticles as illustrated in Fig. 3.5A. The size of the particles is in the range of 10 ~ 20 nm. Fig. 3.6 presents TEM and high-resolution transmission electron microscopy (HRTEM) images, which show the nanoparticles inside the ordered BCC matrix. Local EDX analysis shows that the nanoparticle is Cr-rich. Table 3.2. summarizes the local EDX analysis and provides average compositions of different phases in AlCoCrFe, AlCoCrFeNi<sub>1.0</sub>, and AlCoCrFeNi<sub>2.0</sub>.



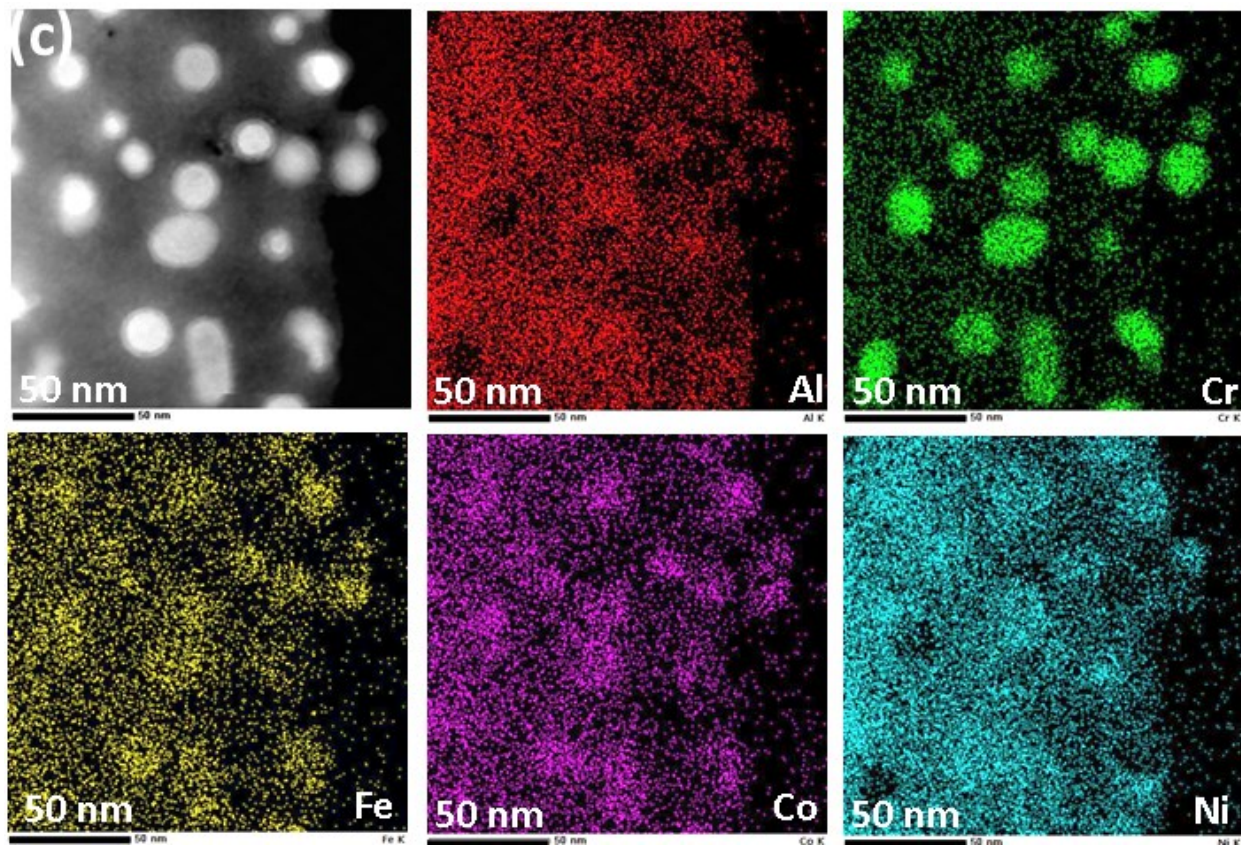


**Fig. 3.6** (a) a TEM image of the ordered BCC phase (B2) in  $AlCoCrFeNi_{2.0}$ , within which nanoparticles are present; (b) a HRTEM image showing nanoparticles and the B2 matrix: the dashed squares A and B were used for fast Fourier transform (FFT) processing. The corresponding diffractograms, displayed just below image (a), indicate that the nanoparticle has a disorder BCC structure while the matrix is B2. (c) a STEM dark-filed image and EDX maps of element distributions in the nanoparticles and the ordered BCC matrix.

**Table 3.2** Local EDX analysis (with TEM) for different phases in AlCoCrFe, AlCoCrFeNi<sub>1.0</sub>, and AlCoCrFeNi<sub>2.0</sub>.

Phases		Concentration (at%)				
		Al	Co	Fe	Cr	Ni
AlCoCrFe	Ordered BCC (B2)	27.66±5.11	34.97±4.48	19.77±3.89	17.60±4.76	
	Disordered BCC	15.56±3.30	17.13±5.04	30.50±3.81	36.81±4.83	
AlCoCrFeNi <sub>1.0</sub>	Ordered BCC (B2)	26.91±4.19	20.89±0.55	16.05±1.08	6.25±1.13	29.89±5.65
	Disordered BCC	1.10±0.64	19.23±2.10	30.42±1.61	44.17±2.06	5.07±0.81
AlCoCrFeNi <sub>2.0</sub>	Ordered BCC (B2)	25.83±5.91	18.62±5.23	10.74±10.09	7.61±6.67	37.20±26.82
	FCC	7.52±0.50	18.59±0.14	19.76±0.57	21.67±0.47	32.39±0.57
Nanoparticle	Disordered BCC	7.66±5.76	14.02±1.21	10.48±4.80	50.06±9.85	17.61±9.16

### 3.2.2 Mechanical properties of AlCoCrFeNi<sub>x</sub> (x = 0 and x > 0)

The macro-hardness of the alloys was measured. Fig. 3.7 illustrates the hardness of the as-cast alloy samples, with Rockwell's scale HRA tested under a load of 60 kgf. As shown, the medium-entropy alloy, AlCoCrFe, is harder than Ni-added AlCoCrFeNi<sub>x</sub>. Ni is an element having a high electron work function, which usually increases the metallic bond strength and thus strengthens materials [12-14]. The decrease in hardness caused by Ni should be attributed to the variations in microstructure and the formed phases as listed in Tables 3.1. and 3.2. The commercial stainless steel was added to compare with the alloys to show the advantages of as-cast alloys which hardness is increased.

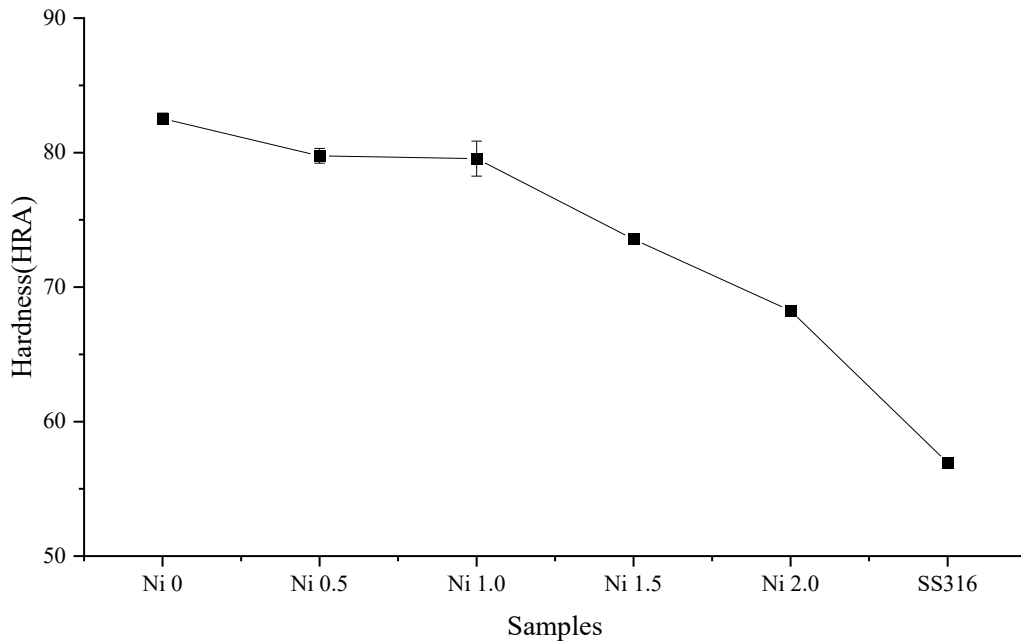


**Fig. 3.7** Vickers hardness test of AlCoCrFeNi<sub>x</sub> (x= 0, 0.5, 1.0, 1.5, 2.0) compared with commercial stainless steel 316 in HRA (load is 60 kgf).

To understand the variations in hardness, micro-indentation tests were performed for the alloys, respectively. Fig. 3.8 illustrates a few images of representative micro-indentation tests on AlCoCrFe, AlCoCrFeNi<sub>1.0</sub>, AlCoCrFeNi<sub>1.5</sub> and AlCoCrFeNi<sub>2.0</sub>, respectively. Values of micro-hardness measured respectively under loads of 80 mN and 300 mN, respectively, are given in Table 3.3. As shown in Fig. 3.8(a) and (b) as well as Figs. 3.1(a) and (c), AlCoCrFe and AlCoCrFeNi<sub>1.0</sub> do not show distinguishable phases under the optical microscope of the micro-indenter. Thus, each of these two samples only has one hardness value under a fixed indentation load as given in Table 3.3. It should be indicated that the micro-hardness value varies with the indentation load [31] but the micro-hardness of the alloys can be ranked when tested using the same indentation load. For AlCoCrFeNi<sub>1.5</sub> and AlCoCrFeNi<sub>2.0</sub>, two phases are distinguishable so that their hardness values were measured. As shown in Table 3.3 and Fig. 3.8, AlCoCrFe has the highest micro-hardness. The micro-hardness decreases with increasing the Ni content. AlCoCrFeNi<sub>2.0</sub> shows markedly lower micro-hardness, and its FCC has the lowest micro-hardness. It should be indicated that under the optical microscope attached to the micro-indenter, the dark domains (Al-Ni-rich) in AlCoCrFeNi<sub>2.0</sub> consist of B2 and FCC phases (Fig. 3.8(d)), which are harder than the FCC but not as hard as dark domains in AlCoCrFeNi<sub>1.5</sub>, which contain B2 phase only (Fig. 3.8(c)). The bright domains in AlCoCrFeNi<sub>1.5</sub> are harder than those in AlCoCrFeNi<sub>2.0</sub> since they could be in the stage of transition from disordered BCC to FCC.

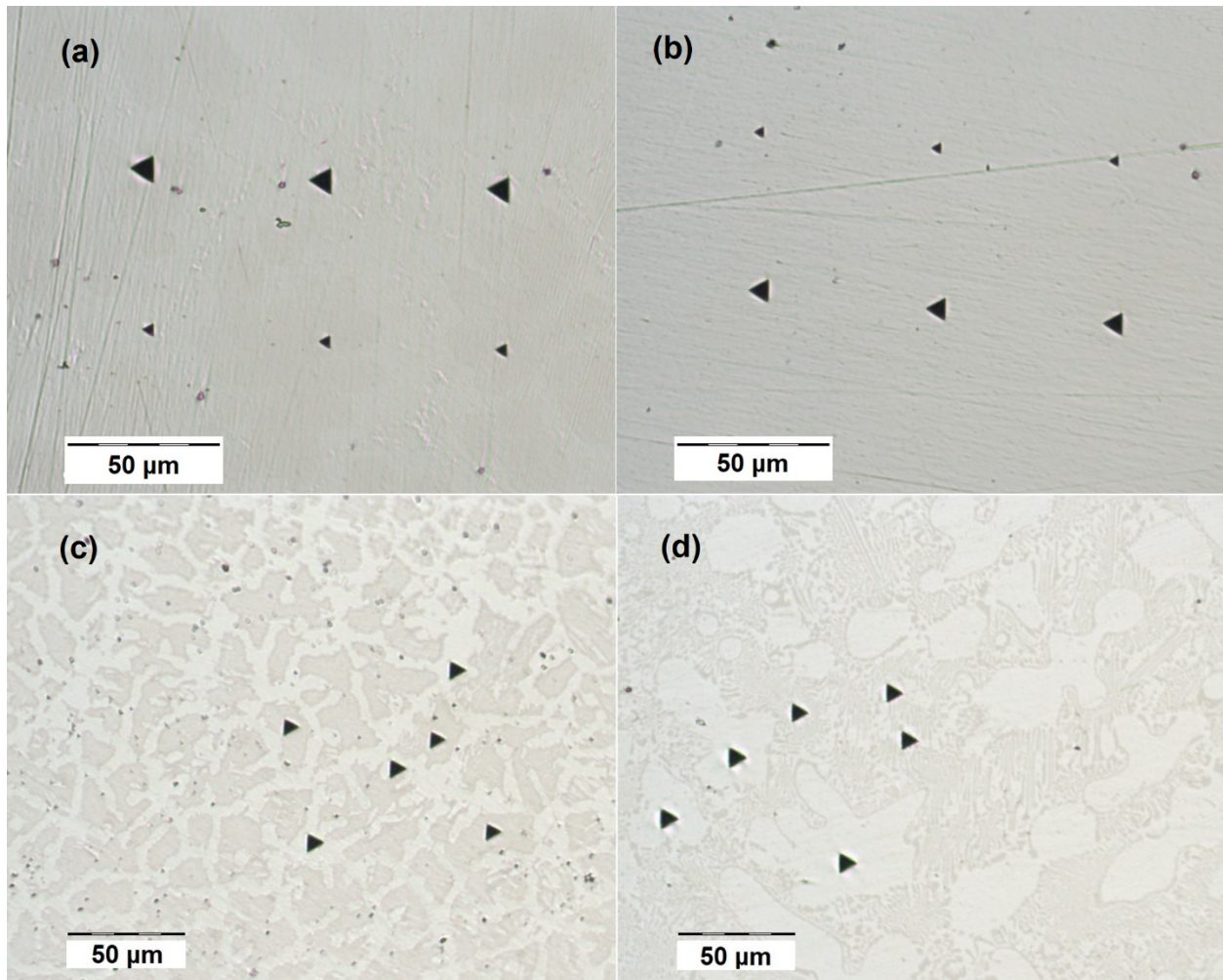


**Fig. 3.8** Nano/micro-indentation tests on (a)  $\text{AlCoCrFe}$ , (b)  $\text{AlCoCrFeNi}_{1.0}$ , (c)  $\text{AlCoCrFeNi}_{1.5}$ , and (d)  $\text{AlCoCrFeNi}_{2.0}$ .

**Table 3.3.** Micro-hardness values of  $\text{AlCoCrFe}$ ,  $\text{AlCoCrFeNi}_{1.0}$ ,  $\text{AlCoCrFeNi}_{1.5}$ , and  $\text{AlCoCrFeNi}_{2.0}$ ; indentation loads: 80 mN and 300 mN.

\* Under the optical microscope, the dark domains in  $\text{AlCoCrFeNi}_{2.0}$  consist of B2 and FCC.

Alloys	HV (80mN)	HV (300mN)
$\text{AlCoCrFe}$	837.23	577.26

AlCoCrFeNi <sub>1.0</sub>		634.77	498.45
AlCoCrFeNi <sub>1.5</sub>	Al-Ni rich dark area: B2	615.23	396.03
	Fe-Cr rich bright area: FCC/Disordered BCC	391.71	332.05
AlCoCrFeNi <sub>2.0</sub>	Al-Ni rich dark area*: B2+FCC	397.28	328.12
	Fe-Cr rich bright area: FCC	341.07	270.98

Based on the microstructure observations and hardness testing, the medium-entropy alloy, AlCoCrFe, is the hardest, which should be ascribed to its nanostructure consisting of an ordered BCC phase (B2) and a disordered BCC phase resulting from spinodal-decomposition, as shown in Fig. 2. The high-entropy alloy, AlCoCrFeNi<sub>2.0</sub>, has the lowest hardness because of its soft FCC phase and coarse microstructure (see Figs. 1, 5, and 8). AlCoCrFeNi<sub>1.0</sub> has its hardness between those of AlCoCrFe and AlCoCrFeNi<sub>2.0</sub>. AlCoCrFeNi<sub>1.0</sub> has ordered BCC (B2) and disordered BCC phases (see Fig. 4), which are much coarser than those in AlCoCrFe (see Figs. 2 and 3), corresponding to lowered hardness. Besides, as the Ni content increases, the disordered BCC transformed to a softer FCC. The disordered BCC appears to be a precursor of the FCC phase and may thus be softened as Ni content increases until it changes to the softer FCC phase. This may be seen from the measured micro-hardness of AlCoCrFeNi<sub>1.5</sub>. It is of interest to see the disordered BCC nanoparticles embedded in the B2 matrix or B2 domains in AlCoCrFeNi<sub>2.0</sub>, which should influence the hardness of the B2 domains. Nevertheless, because of the softer FCC phase, the overall hardness of this alloy is low. It is unclear how the nanoparticles developed in the B2 matrix (see Fig. 6), and how much they influence the mechanical properties of the B2 phase since they are too small to be evaluated using the current micro-indenter. However, due to the lower hardness of the disordered BCC phase according to the hardness data given in Table 3.3., the disordered BCC nanoparticles embedded in the B2 matrix might lower the hardness of

the B2 domains. Further investigation is needed for precise information using other instruments such as atomic force microscope.

Compression tests were performed for further information on the mechanical behavior of the alloys. Fig. 9 illustrates compressive stress ~ strain curves of the alloys. As shown the medium-entropy alloy AlCoCrFe has the highest yield strength, corresponding to the highest hardness. However, this alloy has the lowest ductility and is relatively brittle, compared to others. Because of its nano-scaled two-phase domains from the spinodal- decomposition as shown in Fig. 2(a), this medium-entropy alloy has numerous barriers to dislocation movement, which should be responsible for its high hardness and low ductility. As Ni is added, the yield strength decreases with an increase in ductility. AlCoCrFeNi<sub>2.0</sub> is the most ductile with the lowest yield strength, ascribed to its soft FCC phase and coarse microstructure.

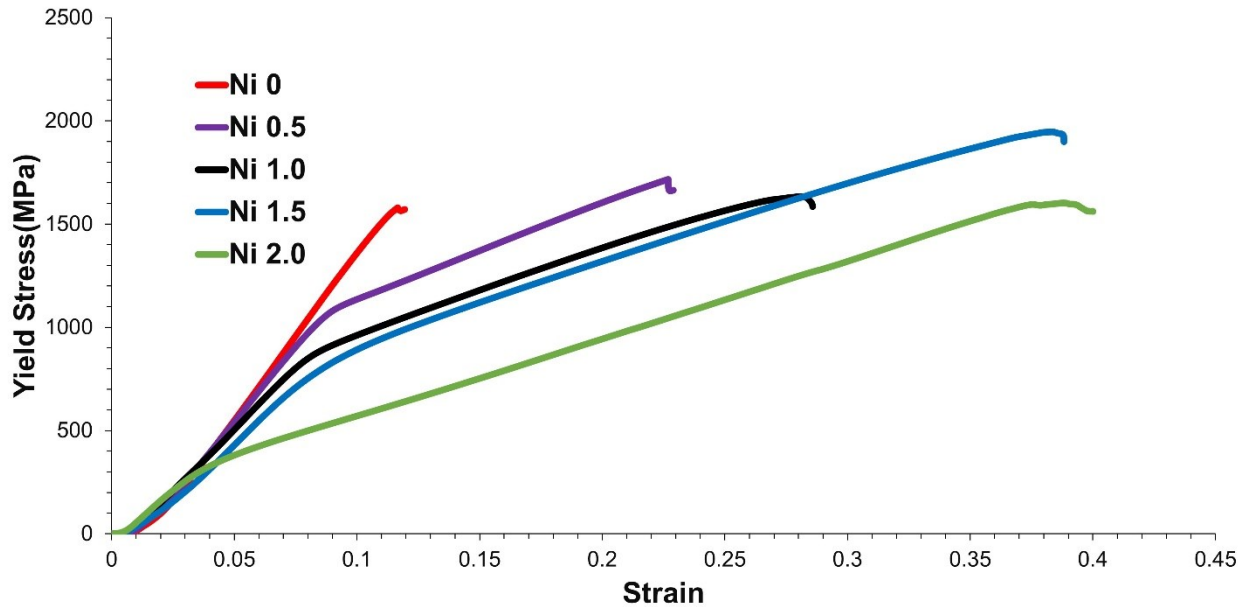


**Fig. 3.9** Compression stress ~ strain curves of AlCoCrFeNi<sub>x</sub> with  $x = 0, 0.5, 1.0, 1.5, 2.0$ .

### 3.2.3 The wear resistance of AlCoCrFeNi<sub>x</sub> (x = 0 and x > 0)

The resistance of the alloys to dry wear was evaluated under the condition described in **Chapter 3.1 Experimental Procedure**. The wear resistance of materials is largely dependent on their hardness. Fig. 3.10 (a) shows volume losses of AlCoCrFeNi<sub>x</sub> (x= 0, 0.5, 1.0, 1.5, 2.0) caused by dry wear tests. As expected, the hardest Ni-free alloy shows the lowest volume loss, and the volume loss increases with increasing the Ni content. The wear tests were performed under two conditions: one was performed in the ambient environment, and the other was performed with an air flow directed to the contact area between the sample and the counterpart (Si<sub>3</sub>N<sub>4</sub> pin), which was used to minimize the surface temperature rise by removing frictional heat. During the dry wear test, the frictional heat more or less increased the temperature of the contact area, thus softening the sample surface and consequently lowering its resistance to wear. As shown in Fig. 3.10(b), with the air flow to remove the frictional heat, volume losses of the samples decreased, compared to those without the air flow, except for the case of AlCoCrFeNi<sub>2.0</sub>. As shown, the softest AlCoCrFeNi<sub>2.0</sub> showed a particularly large increase in the volume loss in contrast with other samples. However, without the air flow, the increase in the volume of AlCoCrFeNi<sub>2.0</sub> was less profound, and the increase in volume loss with increasing the Ni content is approximately in a linear manner. This could be ascribed to the formation of oxide scale or patches that may help withstand the wearing force and reduce the direct damage to the metal surface. With the air flow cooling, the oxidation was more or less reduced, thus minimizing the possible benefit of oxidation on the medium- and high- entropy alloys to their wear resistance. To confirm if this hypothesis is true, wear tracks of samples and local compositions were examined with SEM and EDX.

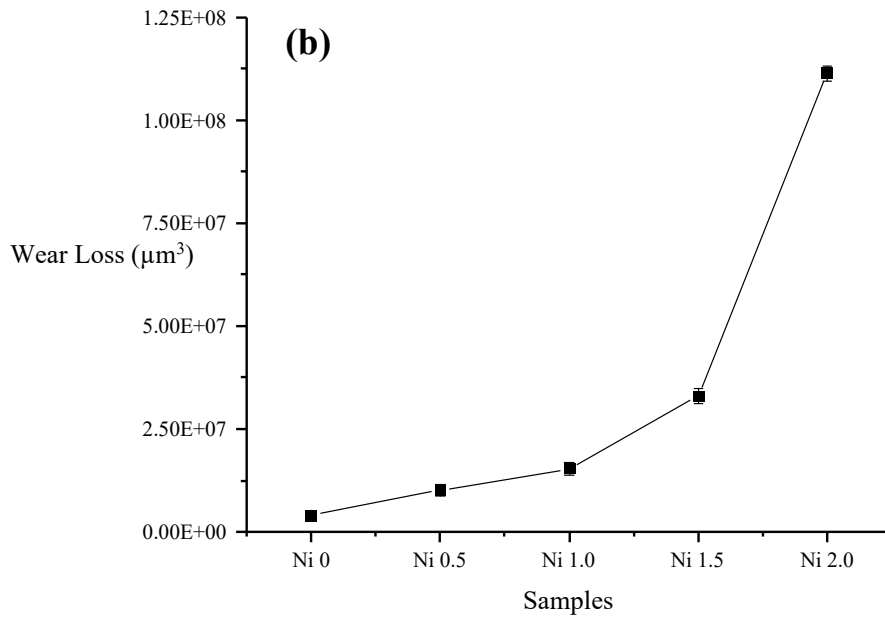
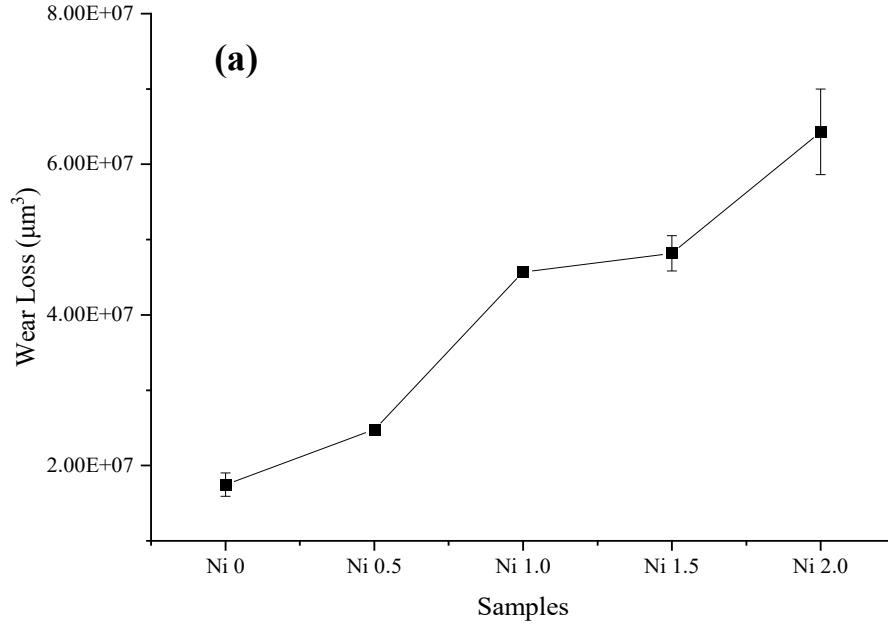


**Fig. 3.10** Wear loss of the alloys caused by (a) dry wear test without airflow and (b) dry wear test with airflow. The airflow was used to minimize the effect of frictional heat on wear.

Figs. 3.11 (a) – (c) illustrate wear tracks on AlCoCrFe, AlCoCrFeNi<sub>1.0</sub> and AlCoCrFeNi<sub>2.0</sub> tested without the airflow. Figs. 3.11 (d) – (f) illustrate the situation with the airflow involved. As illustrated, discontinuous oxide scales or patches are present on the wear tracks. Table 3.4 gives compositions of selected spots on the wear tracks. Based on the worn surface observations and EDX composition analysis, with the airflow cooling, oxidation was minimized, along with the decrease in surface softening by the frictional heat. Although the oxide scale could help withstand the wearing force, the surface softening by frictional heating appears to have a larger influence on the wear resistance, evidenced by the lowered volume loss when tested with the airflow than that without the airflow.

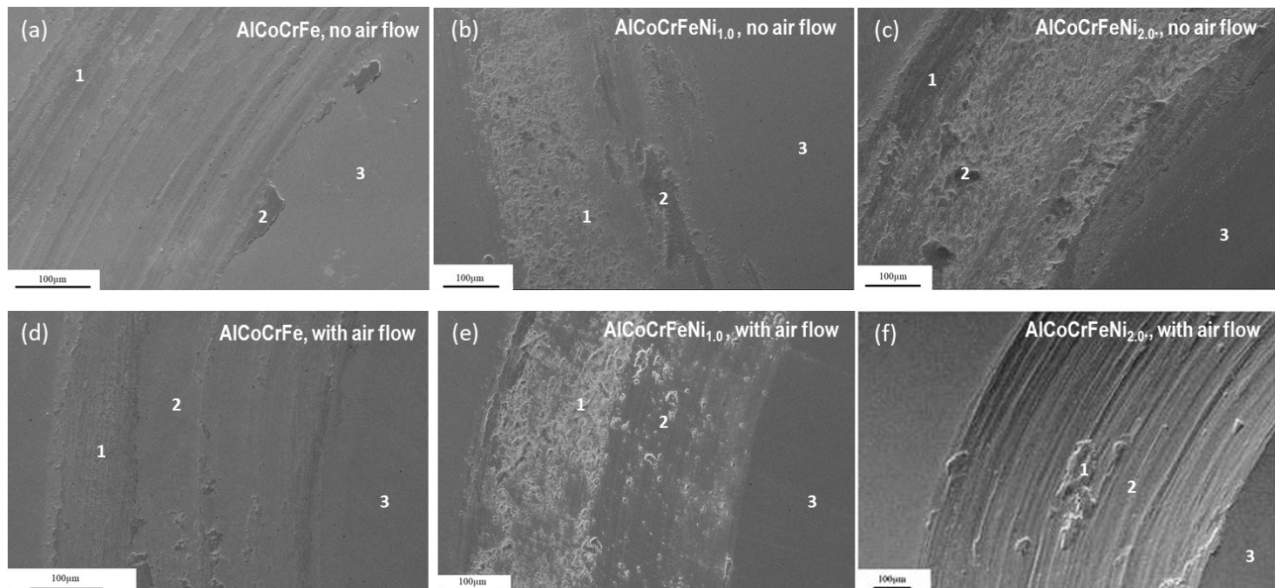


**Fig. 3.11.** The SEM images of wear tracks on (a) AlCoCrFe, (b) AlCoCrFeNi<sub>1.0</sub> and (c) AlCoCrFeNi<sub>2.0</sub>, caused by wear tests with and without the airflow cooling.

**Table 3.4.** – EDX analysis of the local composition of worn surfaces shown in Fig. 3.11

Material	Spot	Al	Co	Cr	Fe	Ni	O
AlCoCrFe, no air flow	1	10.7	12.5	12.7	12.5	--	51.7
	2	7.3	6.9	7.8	7.4	--	70.5
	3	23.7	25.0	26.3	25.0	--	0
AlCoCrFe, with air flow	1	12.5	13.6	14.5	13.7	--	45.7
	2	23.5	23.9	27.0	25.6	--	0
	3	26.1	24.4	25.1	24.3	--	0
AlCoCrFeNi <sub>1.0</sub> , no air flow	1	10.3	11.9	11.6	11.3	10.3	44.8
	2	9.5	9.1	8.8	9.1	9.5	53.9
	3	19.5	19.1	22.6	20.4	18.4	0
AlCoCrFeNi <sub>1.0</sub> , with air flow	1	6.3	9.9	10.1	9.5	9.5	54.7
	2	16.9	20.1	22.0	22.0	19.0	0
	3	20.4	19.3	20.2	20.0	20.1	0
AlCoCrFeNi <sub>2.0</sub> , no air flow	1	4.7	4.4	5.0	4.6	9.0	72.4
	2	4.7	4.7	5.4	4.8	9.5	70.9
	3	15.0	17.5	17.4	15.6	34.5	0
AlCoCrFeNi <sub>2.0</sub> , with air flow	1	12.2	15.3	14.0	14.3	29.0	15.2
	2	28.2	17.2	13.9	16.6	34.3	0
	3	17.7	16.9	14.2	17.8	33.3	0

### 3.3 Conclusions

The microstructure and mechanical properties including hardness, tensile strength and tribological performances of AlCoCrFe MEA and AlCoCrFeNi<sub>x</sub> (x = 0.5 - 2.0) are investigated in this chapter. In conclusion, AlCoCrFe MEA showing a spinodal-decomposed nanostructure with Cr-Fe rich disordered BCC phases and Al-Ni rich ordered BCC (B2) phase presented in TEM results. The increasing contents of Ni transform the disordered BCC phase to a softer FCC phase, and in the AlCoCrFeNi<sub>2.0</sub> 10 ~ 20 nm nanoparticles which have higher Cr content than the surrounding B2 matrix. The reason of the AlCoCrFe MEA is harder than the five-element HEA

is because of the nano-scaled disordered BCC phase and ordered BCC (B2) phase generate a myriad of interfacial barriers to dislocations movement and when the Ni is added, the BCC is transformed to FCC which is decreasing the hardness of the alloys. The result of hardness is directly affecting the result of dry wear test and the AlCoCrFe MEA is showing the highest resistance to wear among these materials.

## **Chapter 4: Corrosion behavior of AlCoCrFeNi<sub>x</sub> (x = 0 and x > 0) with different Ni contents**

There is a lack of understanding the anti-corrosion and wear properties of this high-entropy alloy with respect to the Ni content and its medium-entropy companion for comparison purposes. Although limited studies are found in the literature [89-93], they are more focused on AlCoCrFeNi alloys with specific compositions and their performance under specific processing conditions. In addition, the reported observations and conclusions are not always consistent. Rios *et al.* studied the effect of Ni on the corrosion behavior of AlCoCrFeNi<sub>x</sub> (x=1, 1.4, 1.8) in simulated biological environment, and reported that with increasing Ni content the corrosion rate varied but did not show a consistent trend [89]. In particular, for wear in different modes especially when corrosion and wear are simultaneously involved, how the high-entropy and medium-entropy alloys respond to the wear-corrosion synergy are much less known which we already discussed about the result of dry wear test in the last chapter. For the AlCoCrFeNi based HEA alloys system, numerous studies [97-100] have been conducted in 3.5 w.t.% of NaCl solution but lack a systematic analysis of the corrosion and tribo-corrosion behaviour in the acidic solution for the AlCoCrFeNi based HEA alloys. In this chapter, we will investigate as-cast high-entropy AlCoCrFeNi<sub>x</sub> alloys with x ranging in-between 0 and 2, including corrosion and corrosive wear in acidic solution and result of this study will show in this chapter.

## 4.1 Experiment Procedure

### 4.1.1 Sample preparation

Samples of  $\text{AlCoCrFeNi}_x$  ( $x = 0, 0.5, 1.0, 1.5$  and  $2.0$ ) were prepared using a vacuum arc furnace by melting mixtures of element powders. Each of the mixtures was pelleted into a cylinder using a presser to make a cylindrical sample weighted 10g, which was then placed in the arc furnace and melted three times in a high purity argon gas atmosphere that was used to protect the sample from oxidation. The obtained samples were cut into small pieces with dimensions of  $1 \times 1 \times 0.5$  cm. The samples were polished with sandpaper from grit 80, 180, 400, 800, to 1200. The samples were finally polished with  $1 \mu\text{m}$  alumina powder and washed in an ultrasound cleaning machine with water to remove powder residue on the surface, followed by drying using a pressed air flow. One side of the cut samples was connected to a wire by conductive tape and encapsulated with resin in a silicon mould, once hardened the other side of the samples will again be polished by sandpaper from grit 80 to 1200. The resin encapsulated samples were used to do the polarization test in case to measure the corrosion current and the open-circuit voltage of the samples in diluted  $\text{H}_2\text{SO}_4$  solution ( $\text{pH} = 3$ ). For the corrosion wear, the cut samples were again encapsulated with resin but no wire was attached.

### 4.1.2 Experimental details

Resistances of the AlCoCrFeNi<sub>x</sub> samples with different Ni contents to corrosion in an acidic H<sub>2</sub>SO<sub>4</sub> solution with a pH value equal to 3 were evaluated. Potentiodynamic polarization curves of AlCoCrFeNi<sub>x</sub> alloys in acidic H<sub>2</sub>SO<sub>4</sub> (pH = 3) solution was obtained using a Gamry electrochemical system (Gamry PC4/750). The specimens were mounted in the epoxy resin, with a surface area of 1 cm<sup>2</sup> exposed to the solution. The specimens acted as the working electrode. A Pt plate was used as the counter electrode, and a saturated calomel electrode (SCE) was used as the reference electrode. Prior to the polarization tests, the open circuit potential (OCP) was monitored for 60 minutes to ensure the system reached a relatively stable state. Electrochemical impedance spectroscopy (EIS) measurements were carried out by perturbing the equilibrium at OCP using  $\Delta E = 10$  mV sine wave signals (peak to zero) in a frequency range from 10<sup>5</sup> Hz to 10<sup>-2</sup> Hz. Each test was repeated at least three times to ensure repeatability.

The performance of the AlCoCrFeNi<sub>x</sub> alloys during corrosive wear in the acidic H<sub>2</sub>SO<sub>4</sub> (pH = 3) solution was evaluated using a pin-on-disc tribometer (CSEM Instruments). Before the wear test starts, the encapsulated sample was put into a steel container attached to the spin disk of the tribo-meter which was filled with the diluted H<sub>2</sub>SO<sub>4</sub>. The counterpart for the wear test was a silicon nitride (Si<sub>3</sub>N<sub>4</sub>) ball with a diameter of 4mm. Each wear test was performed under an applied load of 5N at a sliding speed of 200 rpm (equal to 2.1 cm/s) for 30 minutes. After the wear test, the wear track was analyzed using a Zygo, 3D optical profilometer for measuring the volume loss and SEM with EDS (Energy Dispersive Spectroscopy) module was used to analyze the fraction of oxygen content of the wear track.

## 4.2 Result and Discussion

### 4.2.1 Electrochemical properties and corrosion behavior of AlCoCrFeNi<sub>x</sub> (x = 0 and x > 0) with different Ni contents

Corrosion behaviors of the alloys were investigated. Since the alloys contain passive elements of Cr and Al with high concentrations, they are resistant to corrosion in wet and mildly corrosive environments. Thus, this study is more focused on the resistance of the alloys to more aggressive corrosion in an acidic solution, diluted H<sub>2</sub>SO<sub>4</sub> solution (pH=3). Fig. 4.1(a) illustrates corrosion currents of AlCoCrFeNi<sub>x</sub> alloys obtained from potentiodynamic polarization tests. As shown, the corrosion current ( $i_{\text{corr}}$ ) increases with increasing the Ni content, indicating that the added Ni negatively affects the corrosion resistance of the alloy. Since the concentrations of passive elements, Cr and Al, are sufficiently high in all the alloys, Ni may not significantly influence the formation of the passive film and its coverage. This can be seen from the polarization curves of the alloys as illustrated in Fig. 4.1(b). As illustrated, all the alloys display typical active-passive behavior and show slight differences in the passive current density ( $i_p$ ), the width of the passive region ( $\eta_p$ ), and pitting potential ( $E_p$ ). Thus, the decrease in corrosion resistance with increasing the Ni content could be largely attributed to the increase in microstructural heterogeneity as Fig. 3.1 illustrates, which may enhance the galvanic corrosion.

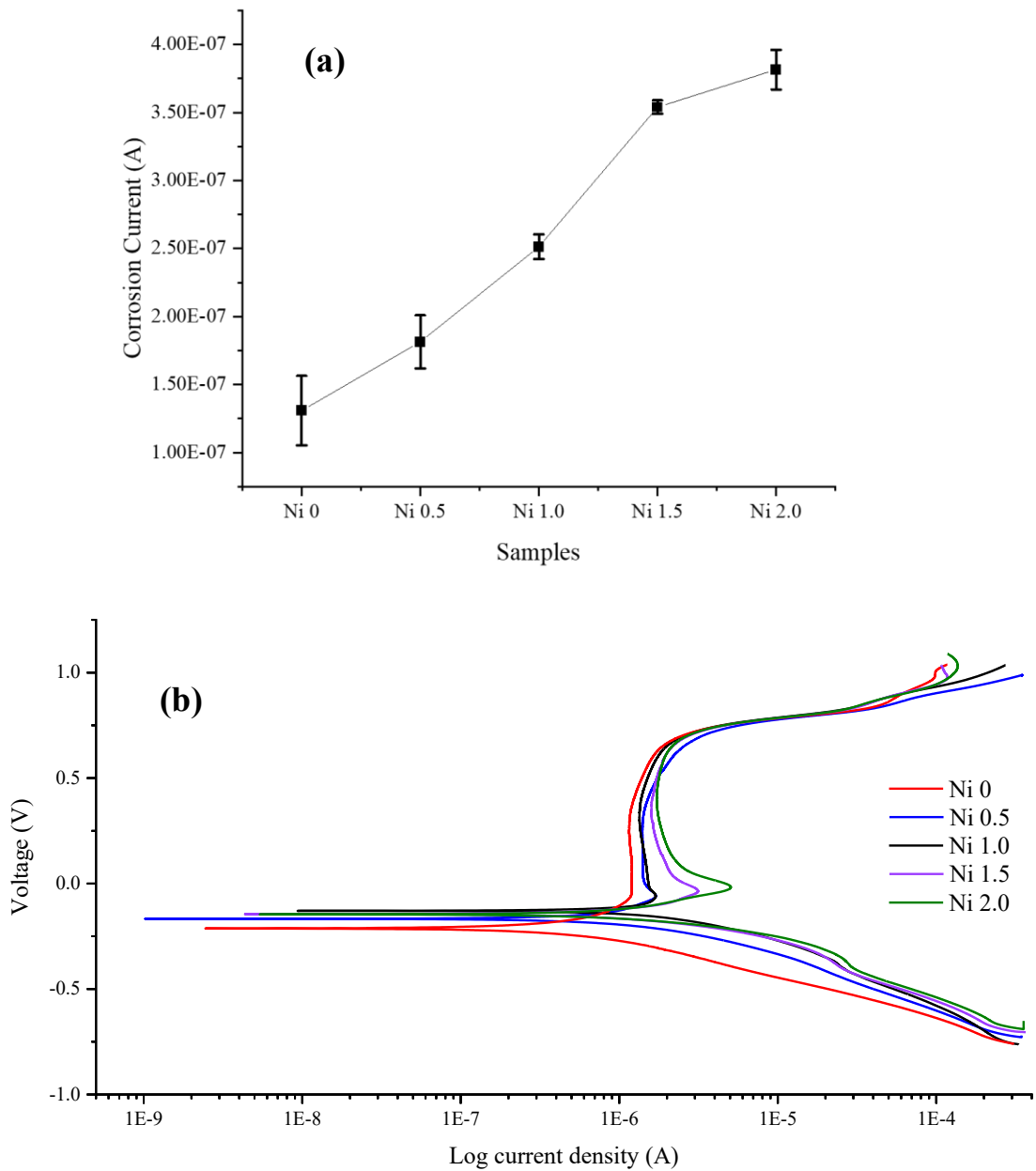
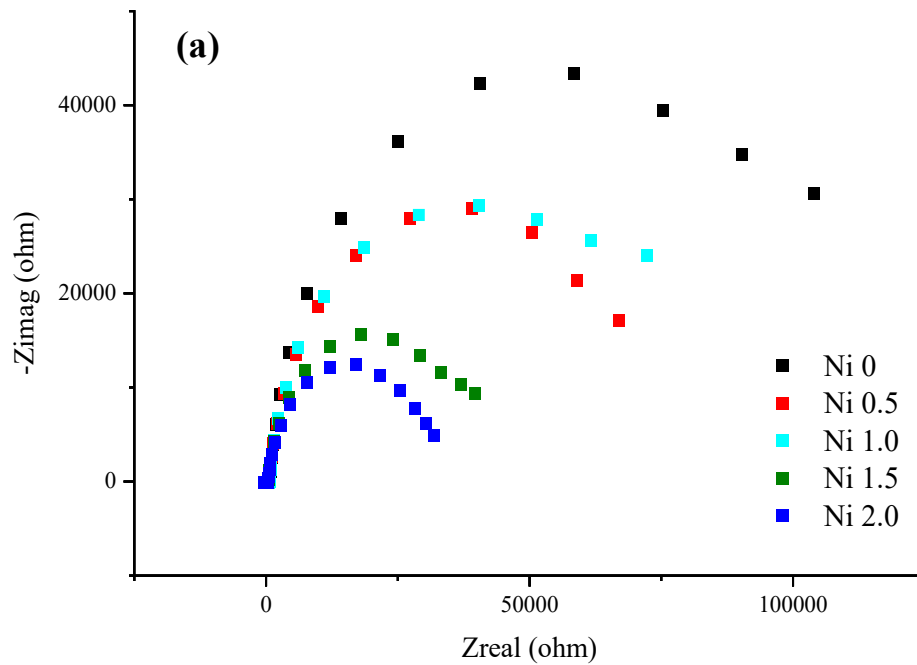


**Fig. 4.1.** (a) Corrosion currents of  $AlCoCrFeNi_x$  in acidic solution of  $pH=3$  ( $x = 0, 0.5, 1.0, 1.5, 2.0$ ); (b) Polarization curves of the alloys in the acidic solution.

In order to further confirm the drawn conclusion, the impedance of the alloys was measured, which is correlated with the corrosion resistance of the alloys and passive film [32]. Fig. 4.2(a) presents Nyquist plots of AlCoCrFeNi<sub>x</sub> alloys in the H<sub>2</sub>SO<sub>4</sub> solution (pH=3). The charge-transfer process should be the primary electrochemical mechanism due to the semicircular shapes of the obtained curves. AlCoCrFe has the largest diameter of its capacitive loop among all the alloys, implying that this Ni-free alloy has higher corrosion resistance than the Ni-containing alloys.



(b)

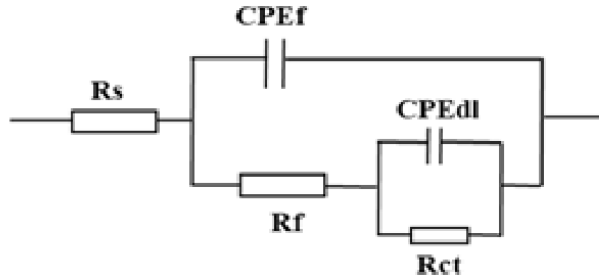


**Fig. 4.2.** (a) Results of impedance measurements for  $\text{AlCoCrFeNi}_x$  ( $x = 0, 0.5, 1.0, 1.5, 2.0$ ) in the acidic solution; (b) Equivalent circuits used to model the impedance data.

Based on the passivation behavior of  $\text{AlCoCrFeNi}_x$  and the contribution of the double electric layer, an equivalent circuit with corrosion-related components is established to fit the experimental data as illustrated in Fig. 4.2(b). In the circuit,  $R_s$  represents the resistance of the solution,  $R_f$  and  $C_f$  represent the resistance and capacitance of the corrosion product film formed on the surface, respectively.  $R_{ct}$  represents the resistance to charge transfer across the interface between the sample and the solution, and  $C_{dl}$  is the capacitance of the double layer. Values of these parameters, determined from fitting results of the impedance measurements, are given in Table 4.1. In the table,  $Y_0$  represents the admittance magnitude of CPE [33], known as a component of an equivalent electrical circuit that models the behavior of a double layer, which is regarded as an imperfect capacitor.  $n$  is the dispersion coefficient with its value in the range of 0

to 1; CPE becomes a capacitor when  $n$  is equal to 1 [34]. With increasing the Ni content in the alloy,  $R_{ct}$  decreases from  $119.6 \text{ k}\Omega \cdot \text{cm}^{-2}$  to  $21.95 \text{ k}\Omega \cdot \text{cm}^{-2}$ , implying that greater Ni contents decrease the corrosion resistance by reducing the surface impedance. Moreover, the difference in  $R_f$  value among all the alloys is modest, which is in good agreement with the passivation behavior of  $\text{AlCoCrFeNi}_x$  shown by the polarization curves. These results indicate that the rates of electrochemical reaction at the corrosion product film/solution interface or dissolution rate of the film on the  $\text{AlCoCrFeNi}_x$  are close. It is worth mentioning that the values of  $R_f$  and  $C_f$  are relatively small, compared with those of  $R_{ct}$  and  $C_{dl}$ , suggesting that the corrosion process of the  $\text{AlCoCrFeNi}_x$  alloy is mainly controlled by a charge transfer process. [35-37]

**Table 4.1.** The fitting results of the impedance measurements.

Samples	CPEdl				CPEf				
	$R_{ct}^a$ ( $k\Omega.cm^2$ )	$Y_0$ ( $\mu\Omega^{-1}.cm^{-2}$ )	n	$C_{dl}$ ( $\mu F.cm^{-2}$ )	$R_f^b$ ( $k\Omega.cm^2$ )	$Y_0$ ( $\mu\Omega^{-1}.cm^{-2}$ )	n	$C_f$ ( $\mu F.cm^{-2}$ )	$R_s^c$ ( $k\Omega.cm^2$ )
AlCoCrFe	119.6	24.9	0.9373	26.72	0.2569	3.944	0.5860	0.03024	0.2910
AlCoCrFeNi <sub>0.5</sub>	110.3	46.1	0.9070	54.49	0.2640	0.07643	0.9062	0.02496	0.0413
AlCoCrFeNi <sub>1</sub>	94.09	40.3	0.9046	46.33	0.2344	0.06564	1.0000	0.06564	0.1353
AlCoCrFeNi <sub>1.5</sub>	41.26	46.2	0.8736	50.77	0.2081	0.06105	0.9018	0.01788	0.1785
AlCoCrFeNi <sub>2</sub>	21.95	44.5	0.8769	44.35	0.3139	0.03763	1.0000	0.03763	0.1411

As mentioned earlier, the decrease in the corrosion resistance of the alloy with increasing the Ni content could be mainly influenced by the microstructure coarsening as shown in Fig. 3.1, which promotes galvanic corrosion. Although AlCoCrFe shows a spinodal-decomposed nanostructure, its microstructural heterogeneity is much smaller than the Ni-containing alloys. Another possible minor factor is the decrease in the atomic percentage of the passive elements, Cr and Al when Ni is added. The four-element AlCoCrFe contains 25 at% Cr and 25 at% Al, while the concentrations of these two passive elements in, e.g., AlCoCrFeNi<sub>2.0</sub>, decrease to 16~17 at%. The decrease in the concentration of the passive elements, though does not influence much the polarization behavior as shown in Fig. 4.1(b), might have some influence on their role in protecting the alloy from corrosion.

For more information, we measured electron work functions of three typical alloys, AlCoCrFeNi<sub>x</sub> ( $x = 0, 1.0, 2.0$ ), using a scanning Kelvin probe. Before the measurement, the surface of the samples was polished using sandpapers from grit 80, 180, 400, 800, to 1200, and then using 1 $\mu$ m alumina paste to smoothen the sample surface and remove the surface film and adsorbed layer. The polished samples were washed with water in an ultrasound cleaning machine to remove powder residue on the surface. The polishing treatment would minimize the influence of surface oxide film and adsorbed layer on the work function measurement, making the measured work function more intrinsic. AlCoCrFe, AlCoCrFeNi<sub>1.0</sub>, and AlCoCrFeNi<sub>2.0</sub> have their work function equal to 4.77 eV, 4.71 eV and 4.64 eV, respectively. The electron work function is the minimum energy required to move electrons at the Fermi level from inside a metal to its surface [12-14], which is a measure of the electrochemical stability and corrosion behavior of metal [13, 38]. The work function measurement indicates that the barrier to electron escape from the alloy AlCoCrFeNi<sub>x</sub> decreases as the Ni was added, and AlCoCrFeNi<sub>2.0</sub> shows

the lowest work function. The variations in work function with Ni content are consistent with the results of corrosion current and impedance measurements shown in Fig. 4.1 and Table 4.1.

#### **4.2.2 Effect of Ni content on corrosive wear of AlCoCrFeNi<sub>x</sub>**

When wear occurred in a corrosive environment, the synergy between wear and corrosion generally increases the damage to the target material. Wear removes the protective layer such as passive film, introduces plastic deformation and defects, making the material more prone to electrochemical attacks. On the other hand, corrosion may increase the surface roughness, or turn the material to a porous weak oxide scale, thus accelerating the wear damage. However, if the oxide is strong and adherent to the substrate, it may benefit the wear resistance. In order to investigate how the AlCoCrFe medium-entropy alloy performs during corrosive wear and how the Ni content influences the performance of high-entropy alloy AlCoCrFeNi<sub>x</sub> under the same corrosive wear condition, corrosive wear tests were performed for all the alloys in the dilute acidic solution (pH = 3). Fig. 4.3(a) illustrates volume losses of AlCoCrFeNi<sub>x</sub> versus the Ni content. Different from their performances during the dry wear tests, AlCoCrFe showed the lowest resistance to corrosive wear, while Ni-containing alloys performed better. Such a trend is unexpected since the Ni-free alloy is the hardest with the highest corrosion resistance among all the alloys under study as demonstrated earlier.

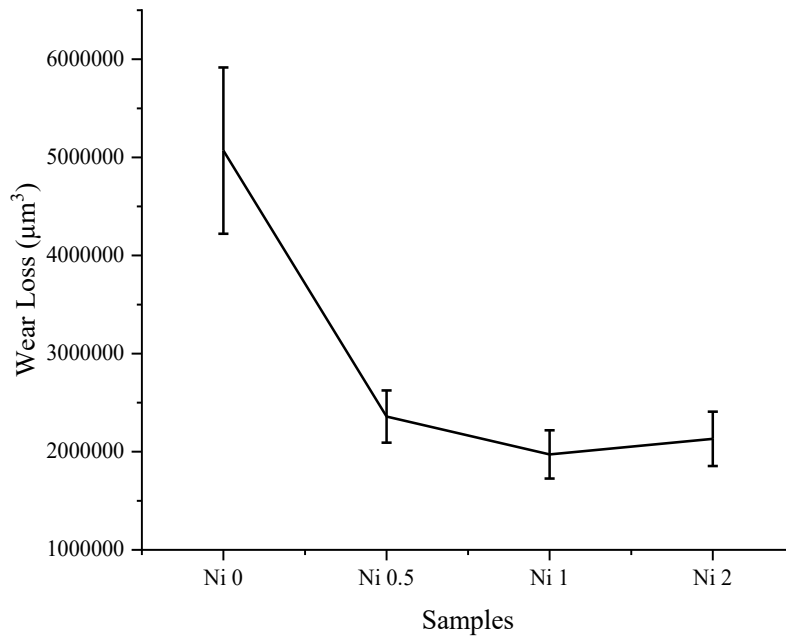


**Fig. 4.3** Volume losses of  $AlCoCrFeNi_x$  ( $x = 0, 0.5, 1.0, 1.5, 2.0$ ) caused by wear under a load of  $5N$  in acidic solution of  $pH = 3$ .

A possible reason for the lower resistance of  $AlCoCrFe$  to corrosive wear, compared to the Ni-containing alloys, could be ascribed to corrosion-enhanced local cracking in this less tough alloy. As demonstrated by the compression tests, the hardest  $AlCoCrFe$  is relatively brittle, compared to the Ni-containing alloys. With increasing the Ni content, the ductility of  $AlCoCrFeNi_x$  increased. During the dry wear test, the frictional heat more or less softened the alloys and minimized the negative influence of the brittleness on the wear resistance and hardness of the alloys that dominated their wear resistance. However, in the acidic solution, the temperature is kept at room temperature, and the corrosive solution may promote local cracking

through the stress-corrosion mechanism [39, 40]. As a result, the ranking of the corrosive wear resistance could be reversed.

In order to check if the above mechanism is possible, the worn surface of AlCoCrFe was examined and compared to those of AlCoCrFeNi<sub>0.5</sub> and AlCoCrFeNi<sub>1.0</sub>. Fig. 4.4 illustrates the wear tracks of the three alloys worn in the acidic solution. As shown in Fig. 4.4(a), cracks and pits are visible on the worn surface of AlCoCrFe. In the corrosive solution, the pits and cracks are blunted. Fig. 4.4(b) illustrates a cross-sectional profile, which shows the depth of two relatively large pits. Fewer smaller cracks and pits are also present on the worn surface of AlCoCrFeNi<sub>0.5</sub>. However, no cracks and pits were observed on AlCoCrFeNi<sub>1.0</sub>. As shown in Fig. 4.3, volume losses of AlCoCrFeNi<sub>x</sub> with x= 0.5, 1.0 and 2.0 are close. Because of the passivation of the alloys in the acidic solution as shown in Fig. 4.1(b), the oxide scales on the alloys could also play a role in resisting corrosive wear. The darker areas are oxide, evidenced by EDX analysis (see Table 4.2). More oxide patches are present on the worn surface of AlCoCrFeNi<sub>1.0</sub> as shown in Fig. 4.4 (d), which should, along with increased ductility, compensate for the decrease in hardness, thus more or less benefiting the resistance of the alloy to corrosive wear.

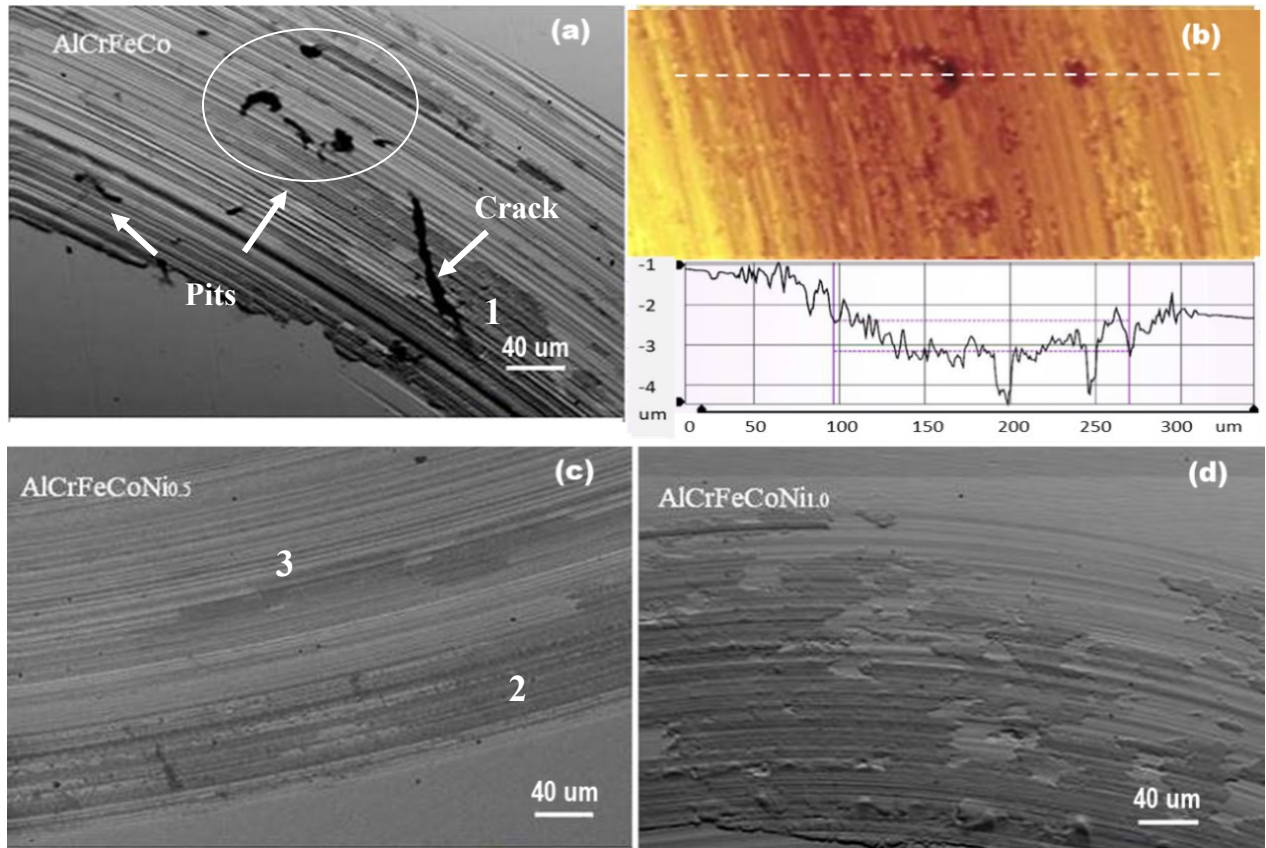


**Fig. 4.4.** Wear tracks of (a)  $AlCoCrFe$ , (c)  $AlCoCrFeNi_{0.5}$ , (d)  $AlCoCrFeNi_{1.0}$ ; Cracks and pits are visible on the worn surface of  $AlCoCrFe$ . (b) a cross-sectional profile of wear track on  $AlCoCrFe$ , which shows the depth of two relatively large pits.

**Table 4.2.** EDX compositional analysis for selected spots.

Sample	Spot	Al%	Co%	Cr%	Fe%	Ni%	O%
$AlCoCrFe$	1	29.8	9.2	10.9	9.6	0	40.4
$AlCoCrFeNi_{0.5}$	2	16.1	14.0	15.6	14.7	7.0	36.4
$AlCoCrFeNi_{0.5}$	3	22.5	21.8	23.0	29.1	10.8	0

## 4.3 Conclusions

Based on the collected information on AlCoCrFeNi<sub>x</sub> (x = 0 – 2.0) alloys, comparison between MEA and HEAs was made in terms of their corrosion resistance and corrosive wear resistance. As shown, with the Ni addition, disordered BCC phase in AlCoCrFe MEA was changed to a FCC phase. This FCC phase along with an ordered BCC phase appears promote galvanic corrosion, leading to a decrease in corrosion resistance with increasing the Ni content. The fractions of passive elements, Cr and Al in the alloys, were lowered when the fifth element, Ni, was added. The decreases in concentrations of Cr and Al may have negative influence on the passivation capability of the alloy and the protectiveness of its passive film. Besides, although the AlCoCrFe MEA is hard and resistance to corrosion, it showed a lower resistance to corrosive wear due to possible lowered resistance to mechanical-electrochemical induced cracking, evidenced by observed micro-cracks and pits on its worn surface. In other words, AlCoCrFe is hard but lack of toughness could be responsible for its lower resistance to the stress-corrosion cracking compared to the Ni-containing alloys with higher ductility. A hard and less tough material is more prone to surface irregularities, such as pits, caused by corrosion and the resultant stress concentrations facilitate cracking and wear.

# Chapter 5: General conclusions and future work

## 5.1 General conclusions

High-entropy alloys have attracted considerable interest and have been extensively studied. However, it is often observed that the medium-entropy alloys may have possess comparable or better properties with less microstructural complications. In this research microstructure, mechanical properties, corrosion and wear behavior of high-entropy alloy  $\text{AlCoCrFeNi}_x$  ( $x > 0$ ) and medium-entropy alloy ( $x = 0$ ) were investigated and compared. It is shown that the Ni content strongly affects properties of the  $\text{AlCoCrFeNi}_x$  alloy. Efforts were also made to clarify underlying mechanisms. General conclusions are listed below:

- a. The medium-entropy alloy,  $\text{AlCoCrFe}$ , shows a spinodal-decomposed nanostructure consists of Cr-Fe-rich disordered BCC phase and an Al-Ni-rich ordered BCC phase (B2). The added Ni made the phases grown from a fine scale to a coarser scale, and continuous increase in the Ni content resulted in a phase transformation from the disordered BCC phase to a FCC phase. Some nanoparticles around 10-20 nm with high Cr content showed up in the B2 phase in  $\text{AlCoCrFeNi}_{2.0}$ .
- b. The medium-entropy alloy  $\text{AlCoCrFe}$  is harder than the five-element high-entropy alloys, which is benefited by its spinodal-decomposed nano-scaled mixture of ordered BCC and disordered BCC phases, which provided many barriers to dislocation movement. The added Ni making coarsened the microstructure and the induced formed FCC phase is softer, reducing the overall hardness and makes the alloy ductile than the medium-entropy alloy.

- c. The resistance of the medium-entropy alloy to wear and corrosion is higher than that of high-entropy alloy due to its nanostructure, which is hard with minimal galvanic effect. Increasing the Ni content softens the alloy and promotes galvanic corrosion due to the microstructure coarsening and disordered BCC – FCC transformation. The lowered fraction of the passive elements, Al and Cr, due to the increased Ni content in the high-entropy alloy could also influence the passivation capability and protectiveness of the formed passive film.
- d. The medium-entropy alloy has a higher wear resistance than the high-entropy alloys. However, the situation is reverse when the alloys were worn in an acidic corrosive environment, although the former has higher hardness and corrosion resistance. Micro-cracks and pits were visible on the medium-entropy alloy, suggesting that this hard but less toughness alloy is prone to stress-corrosion cracking, compared to the Ni-containing high-entropy alloy with higher ductility.

## 5.2 Future studies

The medium-entropy alloy has a nanoscale two-phase structure consisting of a disordered BCC phase and an ordered BCC phase, resulting from a spinodal decomposition. The two phases have coincident interfaces. It has been observed that special defect network formed at the interfaces when deformed at higher strain rates, leading to increased ductility. It is unclear how such interfaces influence the deformation behavior and properties, which is an interesting phenomenon worth being further investigated. The medium-entropy alloy under study is harder and more resistant to wear and corrosion than its high-entropy companion with Ni addition.

However, the medium-entropy alloy shows lower resistance to corrosive wear, compared to the high-entropy ones. Stress-corrosion cracking could be responsible for its inferior performance during corrosive wear which worth being further studied, in order to improve the medium-entropy alloy for widened range applications.

## References

- [1] Yeh JW, Chen SK, Lin SJ, Gan JY, Chin TS, Shun TT, Tsau CH, Chang SY. Nanostructured high-entropy alloys with multiple principal elements: novel alloy design concepts and outcomes. *Adv Eng Mater.* **6** (2004) 299–303.
- [2] Yeh JW. Recent progress in high-entropy alloys. *Ann Chim-Sci Mat.* **31** (2006) 633–648.
- [3] D. B. Miracle, J. D. Miller, O. N. Senkov, C. Woodward, M. D. Uchic, and J. Tiley. Exploration and Development of High Entropy Alloys for Structural Applications, *Entropy* **16** (2014) 494-525.
- [4] F.Y. Tian, L. K. Varga, N.X. Chen, J. Shen, L. Vitos, Empirical design of single-phase high-entropy alloys with high hardness, *Intermetallics* **58** (2015) 1-6.
- [5] M.H. Tsai, J.W. Yeh, High-Entropy Alloys: A Critical Review, *Mater. Res. Lett.* **2(3)** (2014) 107-123.
- [6] J.M. Zhu, H.M. Fu, H.F. Zhang, A.M. Wang, H. Li, Z.Q. Hu, Microstructures and compressive properties of multicomponent AlCoCrFeNiMo<sub>x</sub> alloy, *Materials Science and Engineering A* **527** (2010) 6975–6979s.
- [7] C.B. Nascimento, U. Donatus, C.T. Ríos, R.A. Antunes, Electronic properties of the passive films formed on CoCrFeNi and CoCrFeNiAl high entropy alloys in sodium chloride solution, *Journal of Materials Research and Technology* **9(6)** (2020) 13879-13892.

- [8] W.R. Zhang, P. K. Liaw and Y. Zhang, Science and technology in high-entropy alloys, *Science China Materials* **61** (2018) 2-22.
- [9] P.F. Wu, K.F. Gan, D.S. Yan, Z.H. Fu, Z.M. Li, A non-equiatomic FeNiCoCr high-entropy alloy with excellent anti-corrosion performance and strength-ductility synergy, *Corrosion Science* **183** (2021) 109341.
- [10] S.J. Zheng, Z.B. Cai, J.B. Pu, C. Zeng, S.Y. Chen, R. Chen, L.P. Wang, A feasible method for the fabrication of VAlTiCrSi amorphous high entropy alloy film with outstanding anti-corrosion property, *Applied Surface Science* **483** (2019) 870-874.
- [11] H. Lu, L. Li, X.C. Huang, and D.Y. Li, An electron work function-based mechanism for solid solution hardening, *JALCOM* **737** (2018) 323-329.
- [12] X.C.Huang, H. Lu, and D.Y. Li, Understanding the corrosion behavior of isomorphous Cu–Ni alloy from its electron work function, *Materials Chemistry and Physics* **173** (2016) 238-245.
- [13] H. Lu, Z.R. Liu, X.G. Yan, D.Y. Li, Leo Parent, Harry Tian, Electron work function – a promising guiding parameter for material design, *Scientific Reports* **6** (2016) 24366.
- [14] N. Alharthi, E.S. M. Sherif, H. S. Abdo, and S. Z. E.Abedin. Effect of Nickel Content on the Corrosion Resistance of Iron-Nickel Alloys in Concentrated Hydrochloric Acid Pickling Solutions, Hindawi, *Advances in Materials Science and Engineering* (2017) Article ID 1893672, 8 pages.

- [15] Y.Y. Liu, Z. Chen, J.C. Shi, Z.Y. Wang, J.Y. Zhang, The effect of Al content on microstructures and comprehensive properties in  $\text{Al}_x\text{CoCrCuFeNi}$  high entropy alloys, *Vacuum* **161** (2019) 143-149.
- [16] C.C. Tung, J.W. Yeh, T.T. Shun, S.K. Chen, Y.S. Huang, H.C. Chen, On the elemental effect of  $\text{AlCoCrCuFeNi}$  high-entropy alloy system, *Materials Letters* **61(1)** (2007) 1-5.
- [17] Z.W. Wang, M. Wu, Z.H. Cai, S. Chen, I. Baker, Effect of Ti content on the microstructure and mechanical behavior of  $(\text{Fe}_{36}\text{Ni}_{18}\text{Mn}_{33}\text{Al}_{13})_{100-x}\text{Ti}_x$  high entropy alloys, *Intermetallics* **75** (2016) 79-87.
- [18] X.W. Qiu, C.G. Liu, Microstructure and properties of  $\text{Al}_2\text{CrFeCoCuTiNi}_x$  high-entropy alloys prepared by laser cladding, *Journal of Alloys and Compounds* **553** (2013) 216-220.
- [19] H. Qiu, H.G. Zhu, J.F. Zhang, Z.H. Xie, Effect of Fe content upon the microstructures and mechanical properties of  $\text{Fe}_x\text{CoNiCu}$  high entropy alloys, *Materials Science and Engineering: A* **769** (2020) 138514.
- [20] W.H. Liu, J.Y. He, H.L. Huang, H. Wang, Z.P. Lu, C.T. Liu, Effects of Nb additions on the microstructure and mechanical property of  $\text{CoCrFeNi}$  high-entropy alloys, *Intermetallics* **60** (2015) 1-8.
- [21] C. Li, J.C. Li, M. Zhao, Q. Jiang, Effect of alloying elements on microstructure and properties of multiprincipal elements high-entropy alloys, *Journal of Alloys and Compounds* **475(1-2)** (2009) 752-757.

- [22] H. F. Sun, C. M. Wang, X. Zhang, R. Z. Li & L. Y. Ruan, Study of the microstructure and performance of high-entropy alloys  $\text{Al}_x\text{FeCuCoNiCrTi}$ , *Materials Research Innovations* **19:sup8**, (2015) S8-89-S8-93.
- [23] Y.Q. Zhao, H.Z. Cui, M.L. Wang, Y. Zhao, X. Zhang, C.M. Wang, The microstructures and properties changes induced by Al:Co ratios of the  $\text{AlXCrCo}_2\text{-XFeNi}$  high entropy alloys, *Materials Science and Engineering: A* **733** (2018) 153-163.
- [24] Q.C. Fan, B.S. Li, Y. Zhang, Influence of Al and Cu elements on the microstructure and properties of  $(\text{FeCrNiCo})\text{Al}_x\text{Cu}_y$  high-entropy alloys, *Journal of Alloys and Compounds* **614** (2014) 203-210.
- [25] C.Y. Hsu, W.R. Wang, W.Y. Tang, S.K. Chen, J.W. Yeh, Microstructure and Mechanical Properties of New  $\text{AlCo}_x\text{CrFeMo}_0.5\text{Ni}$  High-Entropy Alloys, *Advanced Engineering Materials* **12(1-2)** 44-49.
- [26] C.C. Juan, C.Y. Hsu, C.W. Tsai, W.R. Wang, T.S. Sheu, J.W. Yeh, S.K. Chen, On microstructure and mechanical performance of  $\text{AlCoCrFeMo}_0.5\text{Ni}_x$  high-entropy alloys, *Intermetallics* **32** (2013) 401-407.
- [27] Chen, MR., Lin, SJ., Yeh, JW., et al. Effect of vanadium addition on the microstructure, hardness, and wear resistance of  $\text{Al}_{0.5}\text{CoCrCuFeNi}$  high-entropy alloy. *Metal Mater Trans A* **37** (2006) 1363–1369 .
- [28] J. Joseph, N. Haghdadi, K. Shamlaye, P. Hodgson, M. Barnett, D. Fabijanic, The sliding wear behaviour of  $\text{CoCrFeMnNi}$  and  $\text{Al}_x\text{CoCrFeNi}$  high entropy alloys at elevated temperatures, *Wear* **428–429** (2019) 32-44.

- [29] Z. Xu, D.Y. Li, D.L. Chen, Effect of Ti on the wear behavior of AlCoCrFeNi high-entropy alloy during unidirectional and bi-directional sliding wear processes, *Wear* **476** (2021) 203650.
- [30] Myslyvchenko OM, Krapivka MO, Tereshchenko OS, Filep MI. Influence of Chromium on the Phase Composition and Specific Features of Hardening of the MnFeCoNiCu High-Entropy Alloy. *Materials Science* **56(3)** (2020) 375-380.
- [31] Li B-Y, Peng K, Hu A-P, Zhou L-P, Zhu J-J, Li D-Y. Structure and properties of FeCoNiCrCu<sub>0.5</sub>Al<sub>x</sub> high-entropy alloy. *Transactions of Nonferrous Metals Society of China (English Edition)*. **23(3)**:735-741.
- [32] Ma Y, Jiang B, Li C, Wang Q, Dong C, Liaw PK, Xu F, Sun L. The BCC/B2 Morphologies in Al<sub>x</sub>NiCoFeCr High-Entropy Alloys. *Metals* **7(2)** (2017) 57.
- [33] W.R. Wang, W.L. Wang, S.C. Wang, Y.C. Tsai, C.H. Lai, J.W. Yeh, Effects of Al addition on the microstructure and mechanical property of Al<sub>x</sub>CoCrFeNi high-entropy alloys, *Intermetallics* **26** (2012) 44-51.
- [34] Hsu, CY., Juan, CC., Sheu, TS., et al. Effect of Aluminum Content on Microstructure and Mechanical Properties of Al<sub>x</sub>CoCrFeMo<sub>0.5</sub>Ni High-Entropy Alloys. *JOM* **65** (2013) 1840–1847.
- [35] J.M. Wu, S.J. Lin, J.W. Yeh, S.K. Chen, Y.S. Huang, H.C. Chen, Adhesive wear behavior of Al<sub>x</sub>CoCrCuFeNi high-entropy alloys as a function of aluminum content, *Wear* **261** (2006) 513-519.

- [36] Y. Dong, Y.P. Lu, J.R. Kong, J.J. Zhang, T.L. Li, Microstructure and mechanical properties of multi-component AlCrFeNiMox high-entropy alloys, *Journal of Alloys and Compounds* **573** (2013) 96-101.
- [37] X.W. Qiu, M.J. Wu, C.G. Liu, Y.P. Zhang, C.X. Huang, Corrosion performance of Al<sub>2</sub>CrFeCoxCuNiTi high-entropy alloy coatings in acid liquids, *Journal of Alloys and Compounds* **708** (2017) 353-357.
- [38] Q.K. Fan, C. Chen, C.L. Fan, Z. Liu, X.Y. Cai, S.B. Lin, C.L. Yang, Effect of high Fe content on the microstructure, mechanical and corrosion properties of AlCoCrFeNi high-entropy alloy coatings prepared by gas tungsten arc cladding, *Surface and Coatings Technology* **418** (2021) 127242.
- [39] Nagase T, Mizuuchi K, Nakano T. Solidification Microstructures of the Ingots Obtained by Arc Melting and Cold Crucible Levitation Melting in TiNbTaZr Medium-Entropy Alloy and TiNbTaZrX (X = V, Mo, W) High-Entropy Alloys. *Entropy* **21(5)** (2019) 483.
- [40] T. Nagase, M. Todai, P. Wang, S.H. Sun, T. Nakano, Design and development of (Ti, Zr, Hf)-Al-based medium entropy alloys and high entropy alloys, *Materials Chemistry and Physics* **276** (2022) 125409.
- [41] E.W. Huang, D.J. Yu, J.W. Yeh, C. Lee, K. An, S.Y. Tu, A study of lattice elasticity from low entropy metals to medium and high entropy alloys, *Scripta Materialia* **101** (2015) 32-35.
- [42] G. Bracq, M. Laurent-Brocq, C. Varvenne, L. Perrière, W.A. Curtin, J.-M. Joubert, I. Guillot, Combining experiments and modeling to explore the solid solution strengthening of high and medium entropy alloys, *Acta Materialia* **177** (2019) 266-279.

- [43] Y.S. Lee, R. J. Cava, Superconductivity in high and medium entropy alloys based on MoReRu, *Physica C: Superconductivity and its Applications* **566** (2019) 1353520.
- [44] J.W. Bae, H.S. Kim, Towards ferrous medium-entropy alloys with low-cost and high-performance, *Scripta Materialia* **186** (2020) 169-173.
- [45] A. Gali, E.P. George, Tensile properties of high- and medium-entropy alloys, *Intermetallics* **39** (2013) 74-78.
- [46] G. Laplanche, A. Kostka, C. Reinhart, J. Hunfeld, G. Eggeler, E.P. George, Reasons for the superior mechanical properties of medium-entropy CrCoNi compared to high-entropy CrMnFeCoNi, *Acta Materialia* **128** (2017) 292-303.
- [47] R.B. Chang, W. Fang, J.H. Yan, H.Y. Yu, X. Bai, J. Li, S.Y. Wang, S.J. Zheng, F.X. Yin, Microstructure and mechanical properties of CoCrNi-Mo medium entropy alloys: Experiments and first-principle calculations, *Journal of Materials Science & Technology* **62** (2021) 25-33.
- [48] Tang Z, Huang L, He W, Liaw PK. Alloying and Processing Effects on the Aqueous Corrosion Behavior of High-Entropy Alloys. *Entropy* **16(2)** (2014) 895-911.
- [49] Y. Zhao, M.L. Wang, H.Z. Cui, Y.Q. Zhao, X.J. Song, Y. Zeng, X.H. Gao, F. Lu, C.M. Wang, Q. Song, Effects of Ti-to-Al ratios on the phases, microstructures, mechanical properties, and corrosion resistance of Al<sub>2-x</sub>CoCrFeNiTi<sub>x</sub> high-entropy alloys, *Journal of Alloys and Compounds* **805** (2019) 585-596.

- [50] Y.Z. Shi, B. Yang, X. Xie, J. Brechtel, K. A. Dahmen, P. K. Liaw, Corrosion of Al<sub>x</sub>CoCrFeNi high-entropy alloys: Al-content and potential scan-rate dependent pitting behavior, *Corrosion Science* **119** (2017) 33-45.
- [51] Y.F. Kao, T.D. Lee, S.K. Chen, Y.S. Chang, Electrochemical passive properties of Al<sub>x</sub>CoCrFeNi (x=0, 0.25, 0.50, 1.00) alloys in sulfuric acids, *Corrosion Science* **52** (2010) 1026-1034.
- [52] C.C. Yen, H.N. Lu, M.H. Tsai, B.W. Wu, Y.C. Lo, C.C. Wang, S.Y. Chang, S.K. Yen, Corrosion mechanism of annealed equiatomic AlCoCrFeNi tri-phase high-entropy alloy in 0.5 M H<sub>2</sub>SO<sub>4</sub> aerated aqueous solution, *Corrosion Science* **157** (2019) 462-471.
- [53] A. Parakh, M. Vaidya, N. Kumar, R. Chetty, B.S. Murty, Effect of crystal structure and grain size on corrosion properties of AlCoCrFeNi high entropy alloy, *Journal of Alloys and Compounds* **863** (2021) 158056.
- [54] X.W. Qiu, Y.P. Zhang, L. He, C.G. Liu, Microstructure and corrosion resistance of AlCrFeCuCo high entropy alloy, *Journal of Alloys and Compounds* **549** (2013) 195-199.
- [55] Y. Qiu, S. Thomas, D. Fabijanic, A.J. Barlow, H.L. Fraser, N. Birbilis, Microstructural evolution, electrochemical and corrosion properties of Al<sub>x</sub>CoCrFeNiTi<sub>y</sub> high entropy alloys, *Materials & Design* **170** (2019) 107698.
- [56] H.T. Duan, Y. Wu, M. Hua, C.Q. Yuan, D. Wang, J.S. Tu, H.C. Kou, J. Li, Tribological properties of AlCoCrFeNiCu high-entropy alloy in hydrogen peroxide solution and in oil lubricant, *Wear* **297** (2013) 1045-1051.

- [57] H. Liang, J.W. Miao, B.Y. Gao, D.W. Deng, T.M. Wang, Y.P. Lu, Z.Q. Cao, H. Jiang, T.J. Li, H.J. Kang, Microstructure and tribological properties of AlCrFe<sub>2</sub>Ni<sub>2</sub>W<sub>0.2</sub>Mo<sub>0.75</sub> high-entropy alloy coating prepared by laser cladding in seawater, NaCl solution, and deionized water, *Surface and Coatings Technology* **400** (2020) 126214.
- [58] Q.F. Zeng, Y.T. Xu, A comparative study on the tribocorrosion behaviors of AlFeCrNiMo high entropy alloy coatings and 304 stainless steel, *Materials Today Communications* **24** (2020) 101261.
- [59] S.Y. Chen, Z.B. Cai, Z.X. Lu, J.B. Pu, R. Chen, S.J. Zheng, C.L. Mao, S.J. Chen, Tribocorrosion behavior of VAlTiCrCu high-entropy alloy film, *Materials Characterization* **157** (2019) 109887.
- [60] Y. Yu, J. Wang, J. Yang, Z.H. Qiao, H.T. Duan, J.S. Li, J. Li, W.M. Liu, Corrosive and tribological behaviors of AlCoCrFeNi-M high entropy alloys under 90 wt. % H<sub>2</sub>O<sub>2</sub> solution, *Tribology International* **131** (2019) 24-32.
- [61] H. Liang, D.X. Qiao, J.W. Miao, Z.Q. Cao, H. Jiang, T.M. Wang, Anomalous microstructure and tribological evaluation of AlCrFeNiW<sub>0.2</sub>Ti<sub>0.5</sub> high-entropy alloy coating manufactured by laser cladding in seawater, *Journal of Materials Science & Technology* **85** (2021) 224-234.
- [62] Sharma, A.K., Perumal, G., Arora, H.S. and Grewal, H.S., Slurry Erosion–Corrosion Resistance of MoNbTaTiZr High Entropy Alloy. *Journal of Bio-and Tribo-Corrosion* **7(3)** (2021) 1-10.

- [63] Muangtong, P.; Namus, R.M.; Goodall, R. Improved Tribocorrosion Resistance by Addition of Sn to CrFeCoNi High Entropy Alloy. *Metals* **11** (2021) 13.
- [64] C.X. Zhang, X.L. Lu, H.B. Zhou, Y.F. Wang, X.D. Sui, Z.Q. Shi, J.Y. Hao, Construction of a compact nanocrystal structure for (CrNbTiAlV)<sub>Nx</sub> high-entropy nitride films to improve the tribo-corrosion performance, *Surface and Coatings Technology* **429** (2022) 127921.
- [65] R.B. Nair, Karthikeyan Selvam, H.S. Arora, Sundeep Mukherjee, H. Singh, H.S. Grewal, Slurry erosion behavior of high entropy alloys, *Wear* **386–387** (2017) 230-238.
- [66] Shittu J., Sadeghilaridjani M., Pole M. et al. Tribo-corrosion response of additively manufactured high-entropy alloy. *npj Mater Degrad* **5**, 31 (2021).
- [67] Z.X. Lu, Y.L. Mao, S.M. Ren, J.M. Pu, Z.Y. Fu, X. Fan, S.Q. Gao, J. Fan, A novel design of VAlTiCrCu/WC alternate multilayer structure to enhance the mechanical and tribo-corrosion properties of the high-entropy alloy coating, *Materials Characterization* **176** (2021) 111115.
- [68] Z.B. Cai, Z. Wang, W.J. Yang, P. Zhang, Y. Lu, J.B. Pu, Microstructure and corrosion behavior of AlCrTiV-X (X = Cu, Mo, CuMo) high-entropy alloy films in 3.5 wt.% NaCl solution, *Surfaces and Interfaces* **27** (2021) 101558.
- [69] M.Y. Wu, R. C. Setiawan, D.Y. Li, Benefits of passive element Ti to the resistance of AlCrFeCoNi high-entropy alloy to corrosion and corrosive wear, *Wear* **492–493** (2022) 204231.
- [70] M. P. Agustianingrum, U.H. Lee, N.K. Park, High-temperature oxidation behaviour of CoCrNi medium-entropy alloy, *Corrosion Science* **173** (2020) 108755.

- [71] M. Zhu, F. He, Y.F. Yuan, S.Y. Guo, G.Y. Wei, A comparative study on the corrosion behavior of CoCrNi medium-entropy alloy and 316L stainless steel in simulated marine environment, *Intermetallics* **139** (2021) 107370.
- [72] Luo, H., Sohn, S.S., Lu, W. et al. A strong and ductile medium-entropy alloy resists hydrogen embrittlement and corrosion. *Nat Commun* **11**, 3081 (2020).
- [73] W. Kai, Z.Y. Jiang, G.T. Chen, I.H. Lee, H.J. Lin, H.H. Hsieh, W.T. Lin, J.J. Kai, High-temperature air-oxidation of NiCoCrAlx medium-entropy alloys, *Corrosion Science* **192** (2021) 109858.
- [74] H. Feng, H.B. Li, X.L. Wu, Z.H. Jiang, S. Zhao, T. Zhang, D. Xu, S.C. Zhang, H.C. Zhu, B.B. Zhang, M.X. Yang, Effect of nitrogen on corrosion behaviour of a novel high nitrogen medium-entropy alloy CrCoNiN manufactured by pressurized metallurgy, *Journal of Materials Science & Technology* **34** (2018) 1781-1790.
- [75] Z.Y. Zhou, B. Liu, W.M. Guo, A. Fu, H. Duan, W.H. Li, Corrosion behavior and mechanism of FeCrNi medium entropy alloy prepared by powder metallurgy, *Journal of Alloys and Compounds* **867** (2021) 159094.
- [76] K. Feng, Y. Zhang, Z.G. Li, C.W. Yao, L. Yao, C.Y. Fan, Corrosion properties of laser clad CrCoNi medium entropy alloy coating, *Surface and Coatings Technology* **397** (2020) 126004.
- [77] F. Weng, Y.X. Chew, W.K. Ong, Y.J. Man, S. Sui, C.L. Tan, F.L. Ng, M.H. Goh, G.J. Bi, Enhanced corrosion resistance of laser aided additive manufactured CoCrNi medium entropy alloys with oxide inclusion, *Corrosion Science* **195** (2022) 109965.

- [78] J. Huang, P.L. Wang, K.F. Du, H.Y. Yin, D.H. Wang, Electrochemical Preparation of Fe<sub>0.5</sub>CoNiCuSn<sub>x</sub> Medium Entropy Alloys and Their Corrosion Properties, *Journal of The Electrochemical Society* **168** (2021) 121503.
- [79] S. Hu, T.J. Li, Z.Q. Su, D.X. Liu, Research on suitable strength, elastic modulus and abrasion resistance of Ti–Zr–Nb medium entropy alloys (MEAs) for implant adaptation, *Intermetallics* **140** (2022) 107401.
- [80] C. R. LaRosa, M. Shih, C. Varvenne, M. Ghazisaeidi, Solid solution strengthening theories of high-entropy alloys, *Materials Characterization* **151** (2019) 310-317.
- [81] QW Tian, GJ Zhang, KX Yin, WL Cheng, YN Wang, JC Huang, Effect of Ni content on the phase formation, tensile properties and deformation mechanisms of the Ni-rich AlCoCrFeNi<sub>x</sub> (x = 2, 3, 4) high entropy alloys. *Materials Characterization* **176** (2021) 111148.
- [82] MY Wu, K. Chen, Z. Xu, DY Li, Effect of Ti addition on the sliding wear behavior of AlCrFeCoNi high-entropy alloy, *Wear* **462–463** (2020) 203493.
- [83] MJ Kang, KR Lim, JW Won, YS Na, Effect of Co content on the mechanical properties of A2 and B2 phases in AlCo<sub>x</sub>CrFeNi high-entropy alloys, *Journal of Alloys and Compounds* **769** (2018) 808-812.
- [84] H. Liu, J. Liu, PJ Chen, HF Yang, Microstructure and high temperature wear behaviour of in-situ TiC reinforced AlCoCrFeNi-based high-entropy alloy composite coatings fabricated by laser cladding, *Optics & Laser Technology* **118** (2019) 140-150.

- [85] H. Liu, SF Sun, T. Zhang, GZ. Zhang, HF Yang, JB Hao, Effect of Si addition on microstructure and wear behavior of AlCoCrFeNi high-entropy alloy coatings prepared by laser cladding, *Surface and Coatings Technology* **405** (2021) 126522.
- [86] JH Pi, Y. Pan, H. Zhang, L Zhang, Microstructure and properties of AlCrFeCuNi<sub>x</sub> ( $0.6 \leq x \leq 1.4$ ) high-entropy alloys. *Materials Science and Engineering A* **534** (2012) 228-233.
- [87] Voiculescu I, Geantă V, Ștefănoiu R, Patroi D, Influence of the Chemical Composition on the Microstructure and Microhardness of AlCrFeCoNi High Entropy Alloy. *Revista de Chimie-Bucharest-Original Edition* **12** (2013) 64.
- [88] LG Cao, XH Wang, YM Wang, LL Zhang, Y. Yang, FB Liu, Y. Cui, Microstructural evolution, phase formation and mechanical properties of multi-component AlCoCrFeNi<sub>x</sub> alloys. *Applied Physics A* **125** (2019) 1-11.
- [89] Ríos ML, Perdomo PPS, Voiculescu I, Effects of nickel content on the microstructure, microhardness and corrosion behavior of high-entropy AlCoCrFeNi<sub>x</sub> alloys. *Sci Rep* **10** (2020) 21119.
- [90] YK Mu, LB Zhang, L. Xu, Prashanth K, NZ Zhang, XD Ma, YF Jia, YL Xu, YD Jia, G. Wang, Frictional Wear and Corrosion Behavior of AlCoCrFeNi High-Entropy Alloy Coatings Synthesized by Atmospheric Plasma Spraying. *Entropy* **22** (2020) 740.
- [91] Yamanaka K, Shiratori H, Mori M, Corrosion mechanism of an equimolar AlCoCrFeNi high-entropy alloy additively manufactured by electron beam melting. *npj Mater Degrad* **4** (2020) 24.

- [92] Lobel M, Lindner T, Mehner T, Rymer L-M, Bjorklund S, Joshi S, Lampke T, Microstructure and Corrosion Properties of AlCrFeCoNi High-Entropy Alloy Coatings Prepared by HVOF and HVOF. *J Therm Spray Tech* **31** (2021) 247–255.
- [93] QH Li, TM Yue, ZN Guo, X. Lin, Microstructure and Corrosion Properties of AlCoCrFeNi High Entropy Alloy Coatings Deposited on AISI 1045 Steel by the Electrospark Process. *Metallurgical and Materials Transactions A* **44** (2013) 1767–1778.
- [94] Z. Li, Pradeep K, Y. Deng, Metastable high-entropy dual-phase alloys overcome the strength–ductility trade-off. *Nature* **534** (2016) 227–230.
- [95] T. Xiong, SJ Zheng, JY Pang, XL Ma, High-strength and high-ductility AlCoCrFeNi<sub>2.1</sub> eutectic high-entropy alloy achieved via precipitation strengthening in a heterogeneous structure. *Scripta Materialia* **186** (2020) 336-340.
- [96] Koppoju S, Konduri SP, Chalavadi P, Effect of Ni on Microstructure and Mechanical Properties of CrMnFeCoNi High Entropy Alloy. *Trans Indian Inst Met* **73** (2020) 853–862.
- [97] R. Wang, K. Zhang, C. Davies, X.H. Wu, Evolution of microstructure, mechanical and corrosion properties of AlCoCrFeNi high-entropy alloy prepared by direct laser fabrication, *Journal of Alloys and Compounds*, Volume **694** (2017) 971-981.
- [98] D.M. Kemény, N.M. Pálfi, É. Fazakas, Examination of microstructure and corrosion properties of novel AlCoCrFeNi multicomponent alloy, *Materials Today: Proceedings*, Volume **45(5)** (2021) 4250-4253.

[99] W. Zheng, Y.P. Wu, S. Hong, J.B. Cheng, L. Qiao, J. Cheng, S.S. Zhu, Electrochemical properties and cavitation erosion behaviors of HVOF sprayed (AlCoCrFeNi)<sub>1-X</sub>(WC-10Co)<sub>X</sub> composite coatings in NaCl medium, *Ceramics International*, Volume **47(20)** (2021) 29410-29422.

[100] Yamanaka, K., Shiratori, H., Mori, M. et al. Corrosion mechanism of an equimolar AlCoCrFeNi high-entropy alloy additively manufactured by electron beam melting. *npj Mater Degrad* **4** (2020) 24.

[101] D. A. Porter, K. E. Easterling, M. Y. Sherif, *Phase transformation in metals and alloys* third edition, 2009.

[102] D.B. Williams and C. B. Carter, *Transmission Electron Microscopy*, 2nd edition, Springer 2009.